Kinetics of Iron Oxide Nanoparticle Nucleation, Growth, and Assembly

Ryan Dean Hufschmid

A dissertation

submitted in partial fulfillment of the

requirements for the degree of

Doctor of Philosophy

University of Washington

2019

Reading Committee:

Kannan M. Krishnan, Chair

Lucien N. Brush

Marjorie A. Olmstead

Program Authorized to Offer Degree:

Materials Science & Engineering

University of Washington

Abstract

Kinetics of Iron Oxide Nanoparticle Nucleation, Growth, and Assembly

Ryan Dean Hufschmid

Chair of the Supervisory Committee:
Professor Kannan M. Krishnan
Materials Science & Engineering

Iron oxides are ubiquitous in nature and serve as a platform for a variety of engineered applications, including biomedical imaging and therapeutic procedures. Interactions between minerals, organic molecules, and ions in aqueous environments are fundamental for both engineered nanoparticles that interface with complex biological media, and for naturally occurring particles in delicate environmental systems. To directly observe and quantify dynamic phase changes of iron oxide nanoparticles in solution I use *in situ* Transmission Electron Microscopy (TEM). To systematically study colloidal stability at the nanoscale we alter surface chemistry by with organic molecules and solution chemistry with the electron beam.

TEM is a powerful materials characterization tool capable of imaging, diffraction, and spectroscopy with atomic resolution. Recent advances in *in situ* TEM techniques and instrumentation enable direct nanoscale imaging and spectroscopy in relevant environments. Specialized holders encapsulate liquid samples, allowing direct observation of dynamic aqueous phenomena under controlled electron dose conditions. Imaging can be complemented by other

characterizations available in the TEM including electron energy loss spectroscopy (EELS) and diffraction for structural and chemical characterization. By observing nanoparticles *in situ*, nucleation, growth, and dissolution kinetics are quantified in real-time to improve our understanding of natural systems and optimize nanoparticle synthesis.

TABLE OF CONTENTS

LIST OF FIGURES

LIST OF TABLES

ACKNOWLEDGEMENTS

Thank you to the many friends, colleagues, and mentors, without whom this work would not have been possible. In particular, I am indepted to my advisor Professor Kannan Krishnan for inviting me to join his group and making so many connections for me along the way. Thank you for your patience and exhortation throughout this endeavor. Thank you to my committee: Prof. Marjorie Olmstead, Prof. Lucien Brush, and Prof. Justin Kollman for your thoughtful and honest feedback. I am grateful for my colleagues in the Krishnan Research Group at UW, whom I have learned so much from and with, especially Dr* Eric Teeman, Dr. Hamed Arami, Dr. R. Matthew Ferguson, Dr. Amit Khandhar, Dr. Youfeng Hou, and Dr* Carolyn Shasha.

Thank you, Professor Nigel Browning, for hosting me at PNNL and serving as a second mentor to me. Without your support, vision, and teaching, this work would not have been possible. I was fortunate to work with many world-class scientists during my time at the lab including Dr. B. Layla Mehdi, Dr. Christina Newcomb, Dr. Jim De Yoreo, Dr. Jay Grate, and Dr. Nik Qafoku.

Thanks to many fellow microscopists for helping me train and/or learning alongside me: Dr. Matthew Olszta, Dr. Libor Kovarik, Dr. Hao Yang, Dr. Lucas Parent, Dr. Patricia Abellan, Dr. Trevor Moser, J. Paige Byers, and Dr. Eric Jensen; you were all so generous with your time and knowledge.

And thanks to my collaborators far and wide, including Omid Sadeghi and Prof. May Nyman at OSU, and Dr. Joachim Landers, Soma Salamon, and Prof. Heiko Wende at the University of Duisburg-Essen.

Erin, my love, for crossing the t's and dotting the i's in every color of the rainbow on these drafts, building our Seattle community, and holding my hand through these challenging and exciting years. Thank You.

DEDICATION

I dedicate this thesis to my family, whom I have relied upon for love, support, meals, and encouragement through all the experiments and miles traveled. Mom and Dad, thank you for always believing I could do this work and for celebrating each step of the process.

Chapter 1. INTRODUCTION

1.1 Iron Oxide Nanoparticles in Natural and Engineered Systems

Iron oxides are of natural scientific and technological interest. Iron, element number 26, is the heaviest element produced by fusion in stars; as such it is abundant throughout the universe and terrestrially. Iron is readily oxidized, forming a variety of iron oxide and hydroxide minerals. These minerals are primary constituents in many natural systems where iron is an important component of many geological and biological materials. Iron oxidation is central to biology—the iron-based protein hemoglobin in blood serves as the oxygen transporter in most animals. Due to its occurrence and role in biology, iron is well-tolerated by the human body and easily metabolized. As such, it is an attractive platform for a variety of biomedical applications. Importantly, iron is a transition metal with partially filled d-orbitals, producing an atomic magnetic moment. In some crystal structures this produces technologically important magnetic phenomena. For example, magnetite (Fe_3O_4) exhibits ferrimagnetism, and at small (< 28 nm) sizes: superparamagnetism.

Superparamagnetic iron oxide nanoparticles (SPIONs) have desirable magnetic properties, general biocompatibility, and are abundant in nature, making them attractive for a variety of biomedical applications. [1] Many engineered applications of nanoparticles require uniform properties which in turn depend on uniform particles. A distribution of particles is monodisperse if the particles have uniform characteristics. This typically refers to the size and size distribution, but crystalline phase and chemistry must all be characterized for particles to show predictable properties. To quantify dispersity, we define a distribution as monodisperse if the standard deviation of the size is less than 5%. For a 10 nm nanoparticle a difference of 5% is on the order of a single unit cell. Because properties are dependent on, for example, particle size, size

distribution, morphology, crystallinity, and immediate environment, [2] it is important to understand how synthetic conditions affect the growth and nucleation of nanoparticles.

1.2 IRON OXIDE PHASES

There are four phases of iron oxide that are stable or metastable at room temperature. These are wüstite (Fe(II)O), magnetite ($Fe(II)Fe_2(III)O_4$), maghemite (γ-$Fe_2(III)O_3$), and hematite (α-$Fe_2(III)O_3$). [3] These phases vary in structure and properties. When synthesizing iron oxides for a given application, it is necessary to have control over which phase is being produced. It is also important to be able to determine which phases are present.

Table 1.1 summarizes the four relevant iron oxide phases as well as some of their properties.

Table 1.1. Summary of stable and metastable iron oxide phases.

Phase	**Chemical Formula**	**Structure (space group)**	**Lattice Parameter**	**Magnetism**
Wüstite	Fe(II)O	'NaCl' (Fm3m)	4.332 Å	Antiferromagnetic*
Magnetite	$Fe(II)Fe_2(III)O_4$	Inverse-spinel (Fd3m)	8.397 Å	Ferrimagnetic
Maghemite	γ-$Fe_2(III)O_3$	Inverse-spinel ($P2_13$)	8.33 Å	Ferrimagnetic
Hematite	α-$Fe_2(III)O_3$	'Corundum' ($R\bar{3}c$)	a = 5.038 Å c = 13.772 Å	Canted antiferromagnetic

*The Néel temperature of wüstite is 198K, so it is effectively paramagnetic at room temperature.

Wüstite (FeO) is a cubic crystal with the same structure as NaCl. It consists of a close-packed, face-centered cubic (FCC), lattice of oxygen atoms interlaced with a lattice of iron atoms. Both magnetite and maghemite have the inverse-spinel structure: also a cubic crystal with an FCC oxygen lattice, with iron occupying some of the tetrahedral and octahedral sites between neighboring oxygens. Models of these structures are shown in Figure 1.1.

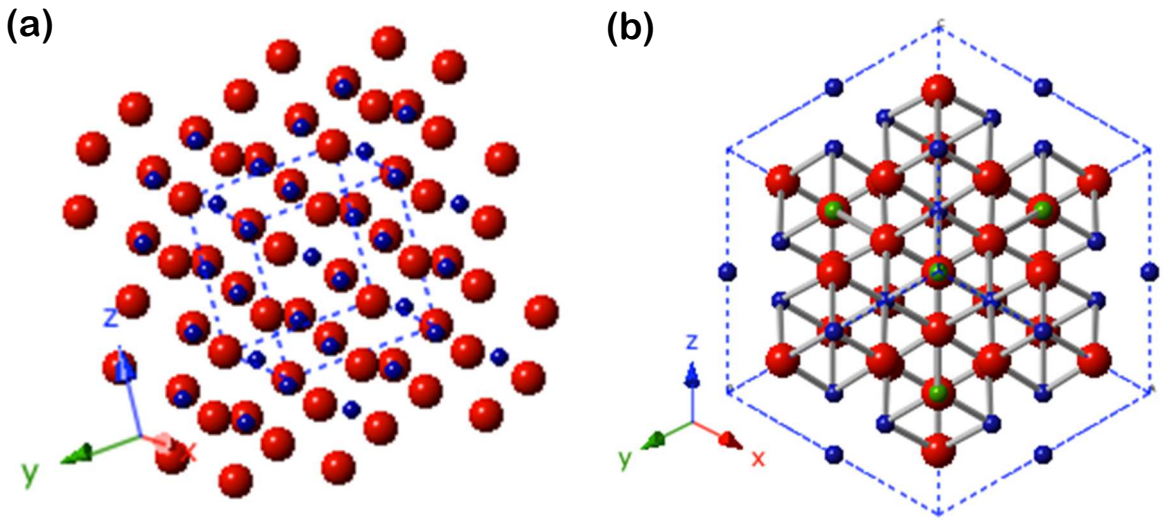

Figure 1.1. Crystal structures of wüstite **(a)** and magnetite **(b)**, with oxygen in red, octahedral iron in blue, and tetrahedral iron in green.

Some iron oxide phases exhibit technologically important magnetic phenomena. Iron is a transition metal with a partially filled d-orbital, giving it an atomic magnetic moment, as depicted in Figure 1.2. In a solid, adjacent atomic moments sum together to give the net magnetic moment. For FeO, adjacent moments are antiferromagnetically coupled and oppose each other. Due to its crystalline symmetry, each moment is paired resulting in no net moment. However, inverse-spinel phases exhibit ferrimagnetism; they have a specific asymmetry of structure and magnetite is mixed valence, containing both Fe^{2+} and Fe^{3+}, so that some paired atomic moments are not equal in magnitude, leaving a net moment.

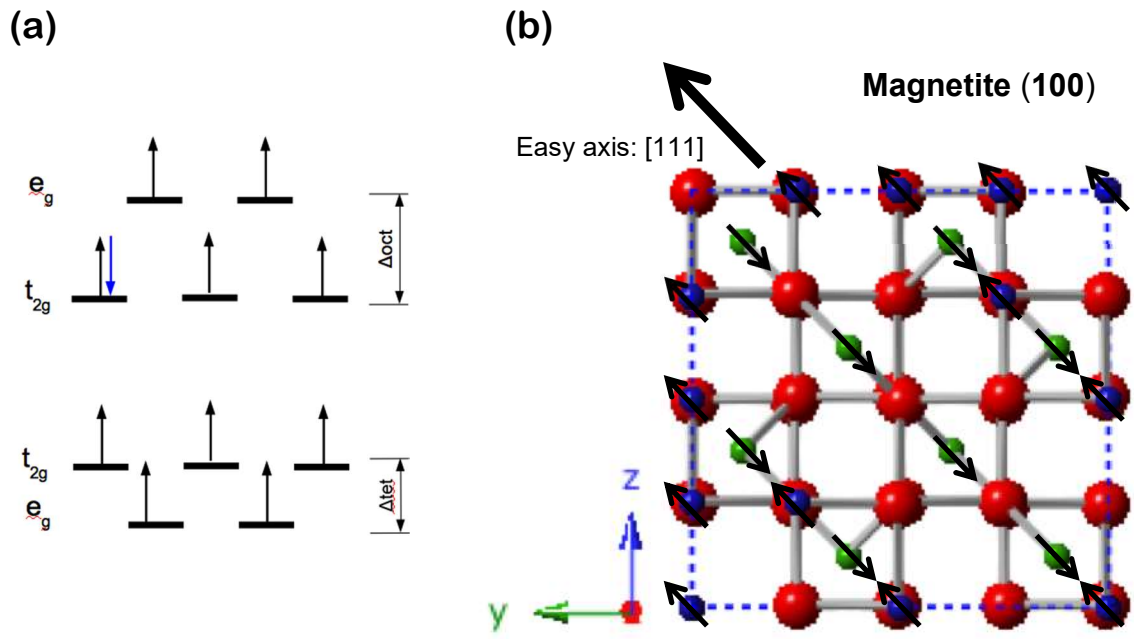

Figure 1.2. The partially filled d-orbital causes iron and other transmission metals to have an atomic magnetic moment **(a)**. In certain crystal structures, such as inverse-spinel magnetite, atomic moments are not balanced, which gives rise to net magnetic moment **(b)**.

In a bulk solid, magnetic materials will form magnetic domains with their own magnetic moments that will arrange to form closed loops to minimize free energy, in the absence of an applied field. Below a certain size a ferro-(or ferri-) magnetic crystal will have a single magnetic domain, called the single domain limit.

An external magnetic field can exert a torque on a magnetic moment. If the field is sufficiently strong it can change the orientation of a magnetic domain. The field required to reverse depends on the domains volume, V, as well as certain physical properties such as the domain's geometry and material properties, encapsulated by its anisotropy, K. K is generally a constant for a given material (iron oxide) and shape (sphere) but we can see that as size (V) decreases, so does the energy to reverse magnetization. If made small enough, thermal energy may be sufficient to

spontaneously reverse magnetization. That is: $k_BT > KV$. We call this behavior superparamagnetism, and the size of this transition the superparamagnetic limit. Of course, other ferromagnetic materials (i.e. cobalt and nickel) will exhibit superparamagnetism, but they do not confer the other benefits of iron oxide, namely that they are toxic. Superparamagnetic nanoparticles have several important technological applications, for example they are the basis for Magnetic Particle Imaging (MPI). [4] In an alternating magnetic field, superparamagnetic articles will show a specific reversal behavior, while nonmagnetic material will not show a significant response. In this way a distribution of magnetic particles can be imaged. The signal produced by the reversal is therefore positive contrast. This has been proposed as novel biomedical imaging modality, and vascular imaging is the primary application.

Although all four iron oxide phases are stable at ambient conditions, over time the lower oxidation state phases tend to oxidize when exposed to heat and sufficient oxygen. [5], [6] Materials progressively transform from wüstite, to magnetite, to maghemite, to hematite. This must be accounted for when performing any experimental technique involving irradiation, or when samples are stored. Transformation may also be exploited if a higher oxidation state phase is desired.

Various characterization methods may determine phase based on their structural and chemical properties. Diffraction experiments are sensitive to structure. However, magnetite and maghemite have nearly identical crystal structures, and the lattice spacing difference is only about 1%, typically within experimental uncertainty. Spectroscopies can characterize chemical composition. In some cases, materials can be characterized according to magnetic properties. These characterization techniques will be discussed in Chapter 2.

Figure 1.3 shows the equilibrium phase diagram for the iron-oxygen system as a function of temperature. This diagram shows the most stable phases for various temperature ranges and oxygen contents.

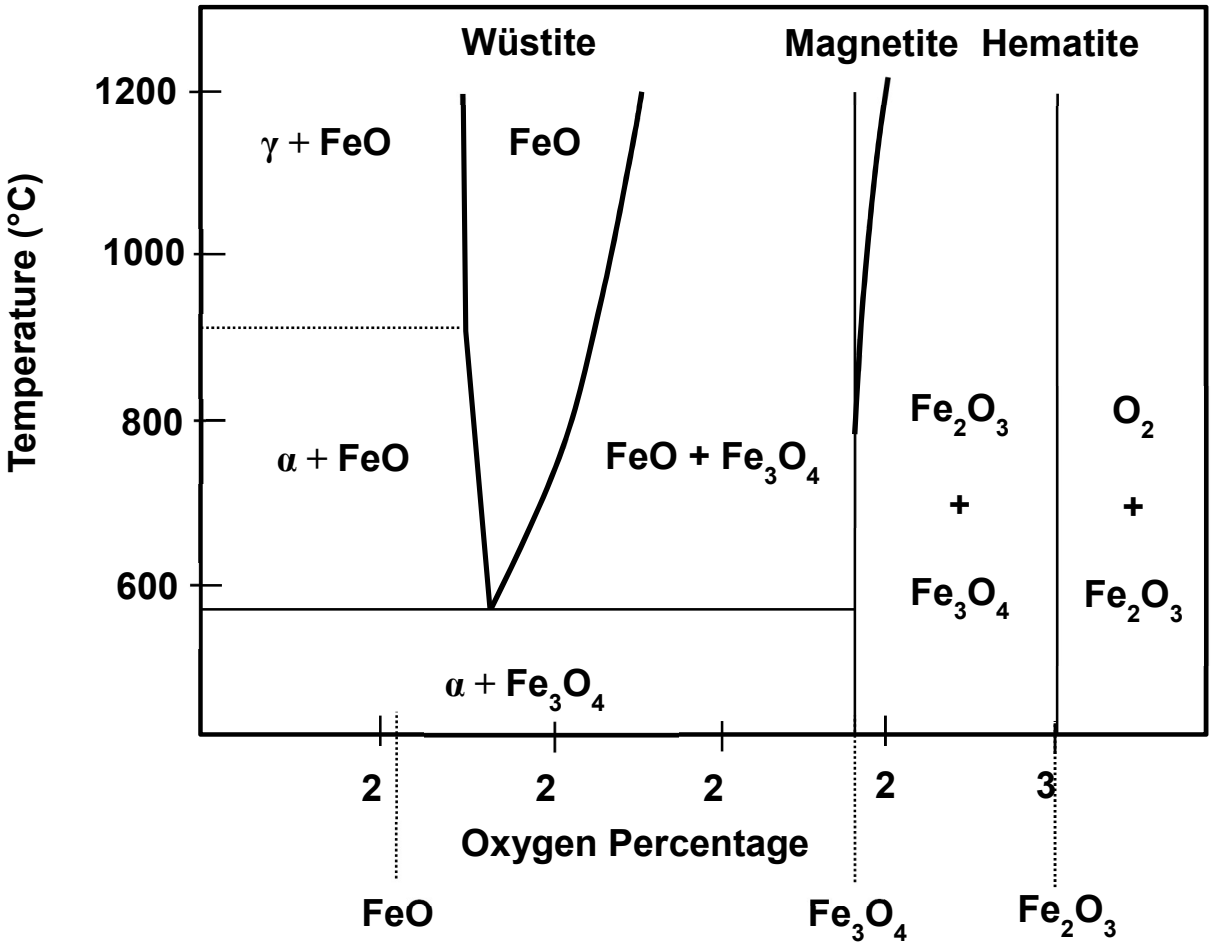

Figure 1.3. Equilibrium phase diagram for the iron-oxygen system.

Phase diagrams are useful for determining expected phases for a given temperature, processing history, and composition. However, this represents a system at equilibrium and will have limited applicability to metastable structures formed under kinetically controlled conditions, such as many of the nanoparticles studied in this work. Maghemite, essentially Fe^{3+}-rich magnetite, is notably absent from the equilibrium diagram, and wüstite, which is not stable at room

temperature, does indeed appear in some of our nanoparticles; although the equilibrium phase diagram does predict the lowest energy phase, it cannot predict the variety of non-equilibrium reactions and structures. Nonetheless, this is a useful reference for predicting phase based on composition and temperature.

Another type of phase diagram shows equilibrium phases as a function of electrochemical potential and pH. Sometimes called a Pourbaix diagram for the scientist who first constructed it, [7] it is used to predict equilibrium compositions in solution. A Pourbaix diagram for the iron-oxygen-hydrogen system in water is shown in Figure 1.4. One feature of this diagram is the presence of hydrated iron oxide phases, which are prevalent in aqueous systems. Also predicted is the formation of Fe^{2+} at acidic pH, which we will observe *in situ* in Section 5.4.

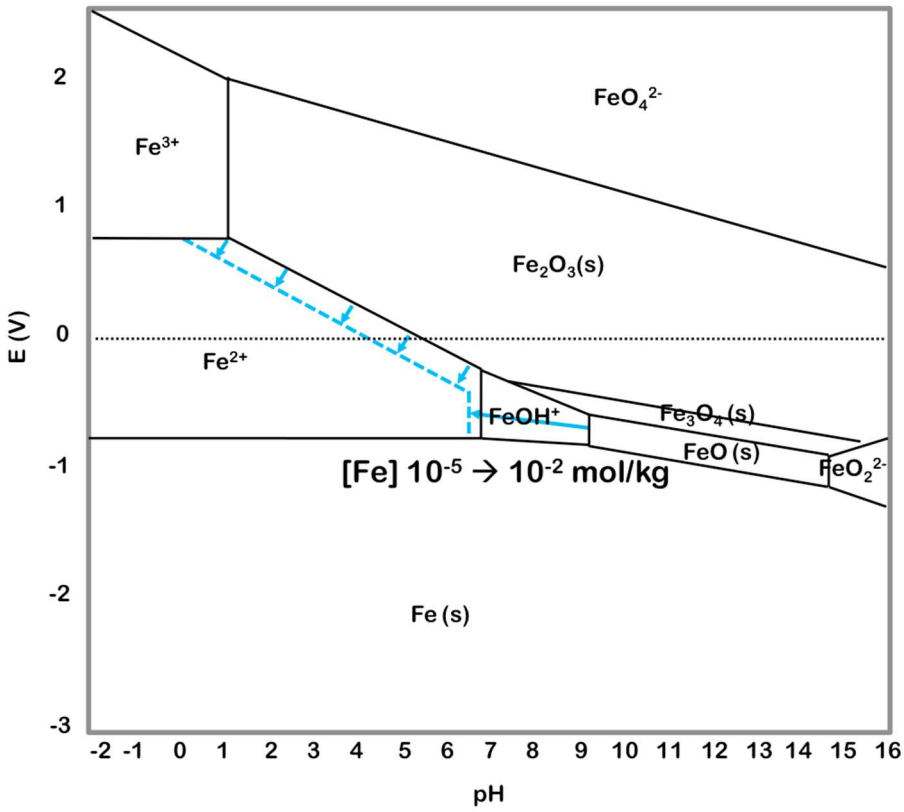

Figure 1.4. Potential vs. pH phase (Pourbaix) diagram for iron-oxygen-hydrogen system in water. The blue arrows denote the shift in stability of the solid region as iron concentration increases, promoting nucleation of iron oxide nanoparticles.

1.3 History of Nanoparticle Synthesis

Historically there have been several approaches to nanoparticle synthesis, with varying degrees of synthetic control. Scientific investigation of nanoscale gold colloids began with Faraday in the 1850s [8], but other medical, alchemical, and artistic applications for gold colloids can be traced back to antiquity, long before the field of nanotechnology was formally conceived. [9] The production of gold nanoparticles by aqueous reduction of gold chloride was described in 1951, [10] Following this synthetic template, a wide variety of metallic nanoparticles, for example Pt, [11] Co, [12] Bi, [13] Ni, [14] and Ru, [15] have been produced by aqueous reduction syntheses. Multi-component nanoparticles, such as oxides, can be synthesized by aqueous co-precipitation; [16], [17] however, organic phase syntheses generally provide the highest degree of synthetic control. [18]–[21]

Currently, the Krishnan Research Group at the University of Washington develops magnetic nanoparticles for biomedical applications, contributing significantly to fields of magnetic imaging and nanoparticle synthesis. [1], [22] Initial attempts to develop magnetic nanoparticle tracers began with cobalt. [12]. However, focus eventually shifted to iron oxide-based platforms due to advantages that have been previously discussed. Synthesis of iron oxide nanoparticles in the Krishnan group began with the work of Marcela Gonzales on magnetic fluid hyperthermia (MFH). [23]–[25] This was continued with R. Matthew Ferguson, who optimized SPIONs for Magnetic Particle Imaging (MPI) and developed much of the Magnetic Particle Spectrometry (MPS) hardware still in use in the group. [26]–[28] Amit Kandahar further developed the nanoparticle synthesis and aqueous phase transfer and optimized the nanoparticle coating for biomedical applications, [29], [30] and Hamed Arami further developed surface coatings and functionalization in addition to undertaking animal trials. [31]–[33] Current research in the

Krishnan Group focuses on deepening our understanding of SPION biodistribution and intracellular fate, [34], [35] as well as the physics of magnetic relaxation dynamics. [36]

This work aims to bring our understanding of the structure, chemistry, and properties of superparamagnetic iron oxide nanoparticles (SPIONs) up to date using state-of-the-art characterization techniques.[1] In Chapter 2 I begin with an overview of the experimental methods and techniques used to characterize iron oxide phases. Chapter 3 compares synthesis of iron oxide nanoparticles by various chemical routes. Following the synthesis, in Chapter 4 I investigate the nanoscale structure and chemistry of iron oxide nanoparticles in more detail. Finally, I use *in situ* electron microscopy to observe and quantify the nucleation, growth, and colloidal stability of iron oxide nanoparticles in Chapter 5.

[1] Portions of this work have been published in refereed journal articles and presented at professional conferences and are denoted with footnotes and in-text citations. [37]–[44]

Chapter 2. MATERIALS CHARACTERIZATION

2.1 COMPLEMENTARY CHARACTERIZATION TECHNIQUES

Uniquely determining iron oxide phase typically requires complementary phase characterization techniques. Due to similarity among the phases, structural characterization, i.e. diffraction, should be combined with chemical characterization, i.e. spectroscopy. To characterize a batch of nanoparticles in aggregate (approximately 1 mg or more), a combination of Raman spectroscopy and x-ray diffraction can be used. For nanoscale phase characterization, TEM enables sub-nanometer imaging, diffraction, and often spectroscopy (i.e. EELS) in a single instrument, so in this work TEM is the primary characterization instrument. It is still important to correlate experimental results with other approaches and across length scales.

The iron oxide phases differ both crystallographically and electronically based on the valence state of the iron. Magnetite and wüstite are crystallographically distinct and discernable using X-ray or electron diffraction. Because both magnetite and maghemite are inverse-spinels with similar lattice spacing, distinguishing between these two phases with diffraction is difficult for crystals smaller than approximately 20 nm, because the size-induced broadening of diffraction peaks istoo large to resolve the 0.8% difference in lattice parameter. To determine the phase of an iron oxide definitively, complimentary characterization techniques are typically necessary, for example by combining diffraction experiments (X-ray or electron) with Raman spectroscopy.

The most common methods for characterizing crystallography are diffraction experiments, X-ray or electron, and Raman spectroscopy. Raman is sensitive to vibrational modes of the crystal, while diffraction directly captures the reciprocal lattice. To characterize the electronic structure of an iron oxide, electron shell transition energies are measured. These excitations are typically driven

by high energy electrons, e.g. EELS. These experiments could just as easily be carried out optically with X-rays, as in X-ray Absorption Near Edge Spectroscopy (XANES).

When applied together, diffraction and Raman spectroscopy are used to determine the phase of any unknown iron oxide. These techniques typically require milligrams of sample. However, the materials here are nanoparticles, and eventually will be synthesized *in situ* in a TEM. It is beneficial to have techniques that can characterize small amounts of nanoparticles and can be performed inside of a microscope. I will discuss electron diffraction, and EELS because these will be useful in characterizing materials *in situ*.

2.1.1 *Raman Spectroscopy*

In Raman spectroscopy, a laser is incident on a sample. A photon is absorbed and interacts with Raman active modes within the lattice. Then, a second photon is emitted, shifted relative to the incident photon. This shift is dependent on the structure of the sample and the local bonding environment. The Raman spectra can be diagnostic of a material. All spectra were obtained using a 514 nm laser.

To establish reference spectra, Raman has been performed on commercially available powders of magnetite and hematite (Atlantic Equipment Engineers), nominally 1—5 μm in size. The diagnostic peak for magnetite is observed around 667 cm^{-1}, with smaller peaks at 330 cm^{-1} and 550 cm^{-1}. Hematite has four peaks between 200—400 cm^{-1}, a peak at 616 cm^{-1}, and a peak at 1322 cm^{-1}. These values are consistent with literature.[6], [45]

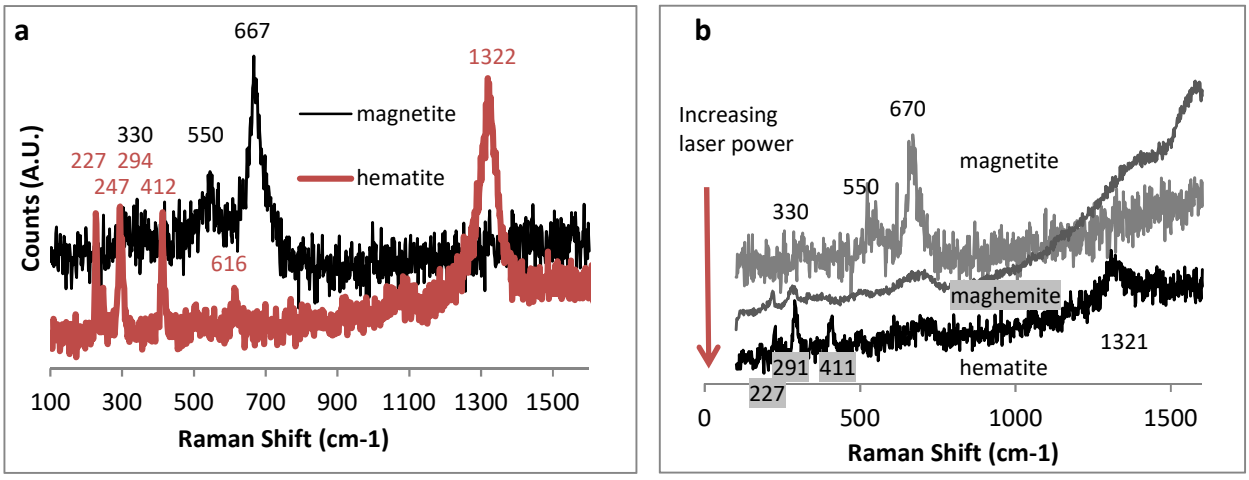

Figure 2.1. Raman spectra of iron oxide reference powders, **(a),** and Raman from magnetite iron oxide nanoparticles at various stages of laser induced oxidation, **(b)**.

Care must be taken not to oxidize samples when performing Raman on iron oxides. Wüstite readily oxidizes to magnetite, to maghemite, to hematite. Wüstite is virtually undetectable in Raman due to said rapid oxidation, and when characterizing magnetite or maghemite in air, laser power must be kept below around 1 mW.[5], [6] This sequential transformation is demonstrated in Figure 2.1 and shows the oxidation of nanoparticles from magnetite, to maghemite, and finally transformation to hematite. This also provides us with a diagnostic spectra for maghemite. Because it is also an inverse-spinel it shows the same vibrational modes as magnetite, however, due to the different electronic structure, the prevalence of various peaks is altered. The broadening of the ~670 cm^{-1} peak as well as the prevalence of the second harmonic around 1340 cm^{-1} are considered diagnostic of maghemite. [6] The low wavenumber peaks seen in the maghemite spectra are the first indication of the presence of hematite.

2.1.2 *Diffraction*

In diffraction experiments, an incident beam of electrons or photons is scattered by the lattice of the crystal. The intensity of the diffracted radiation depends on the angular relationship between the beam and the crystalline planes within the sample. The angles for constructive interference are given by Bragg's law: $2dsin\theta = n\lambda$. Where d is the planar spacing, θ is the angular relation between the beam and the plane, and λ is the wavelength of radiation. Electron diffraction is described in §2.2, and X-ray diffraction is applied in §3.6.

2.1.3 *Magnetometry*

Vibrating sample magnetometry (VSM) characterizes the particles magnetic behavior, and can be used to estimate their size. In VSM the sample is placed in a uniform magnetic field (H) while the sample is vibrated sinusoidally, perpendicular to the magnetic field throughout the entire measurement. The change in magnetic induction is measured on a pickup coil and the magnetization (M) of the sample is determined. Typically, a range of magnetic field values are cycled through to generate a magnetic susceptibility curve (M vs. H).

Magnetic characteristics were evaluated using a Vibrating Sample Magnetometer (VSM) (Lakeshore, Weterville, OH) and custom-built [27] Magnetic Particle Spectrometer (MPS). Differential susceptibility (dm/dH or $\chi_{diff}[H]$) was measured using the MPS, with a 18.6mTμ_0^{-1} sinusoidal excitation field at 25kHz. MPS plots were normalized to compare the full width at half maximum (FWHM), which is an indicator of the potential spatial resolution in MPI scanners, [27], [46] The median magnetic core size and distribution were determined from VSM magnetization curves using the Chantrell method. [47] The initial susceptibility (χ_i), coercivity (H_0), and saturation magnetization (M_s) of the nanoparticles were experimentally determined and fit to a

Langevin function, using 446 kA/m as bulk M_s for magnetite. [26] Magnetocrystalline and shape anisotropies are critical to SPION performance, in particular for MPI and MFH. [48]–[51] Anisotropy constants for our nanoparticles have previously been measured to be on the order of 3.5 ± 3.0 kJ/m^3 for 25 nm SPIONs, well below bulk values of approximately 11 kJ/m^3. [52], [53]

Where sizes are reported throughout this work, unless otherwise noted, they are median diameter as determined by this fitting procedure. Error bars represent first standard deviation of the log-normal size distribution. VSM size estimates, and volumetric measurement techniques are in general better statistical representations of a sample as they analyze millions of particles compared to TEM measurements that, at best, include thousands of particles. However, Chantrell fitting assumes a log-normal distribution, and that particles are superparamagnetic. If particles are ferro- or antiferromagnetic, or the size distribution is not log-normal, the results will be inaccurate. Thus, both TEM and VSM are complimentary techniques providing valuable information.

Both the particles' magnetic size, D, and their distribution, σ, can be calculated from their room temperature magnetization curves. This was derived by Roy Chantrell, [47] and sometimes referred to as Chantrell fitting.

$$D = \left[\frac{18\mathrm{kT}}{\pi I'_s}\sqrt{\frac{\chi_i}{3\epsilon I'_s}\frac{1}{H_0}}\right]^{1/3}$$

$$\sigma = 1/3\left[\ln\left(3\,\chi_i/\left(\epsilon I'_s\frac{1}{H_0}\right)\right)\right]^{1/2}$$

Where the susceptibility, χ_i, the saturation magnetization, $\varepsilon I'_s$, and the field at $I=0$, $1/H_0$, are all determined experimentally by VSM from the slope of the linear region, the saturation magnetization (M_S) and the y-intercept, respectively.

Figure 2.2 shows an example magnetization curve for superparamagnetic iron oxide nanoparticles, measured in chloroform. Note the superparamagnetic behavior, that is, no remnant magnetism. There is a small amount of open loop behavior, presumably due to particle interactions.

Addition of polymer stabilizers or aqueous phase transfer could reduce interparticle interactions and it is now standard practice to measure magnetic properties of SPIONs after they have been coated transferred to water. However, for smaller particles (< 25 nm), measurement in organic solvents if generally acceptable.

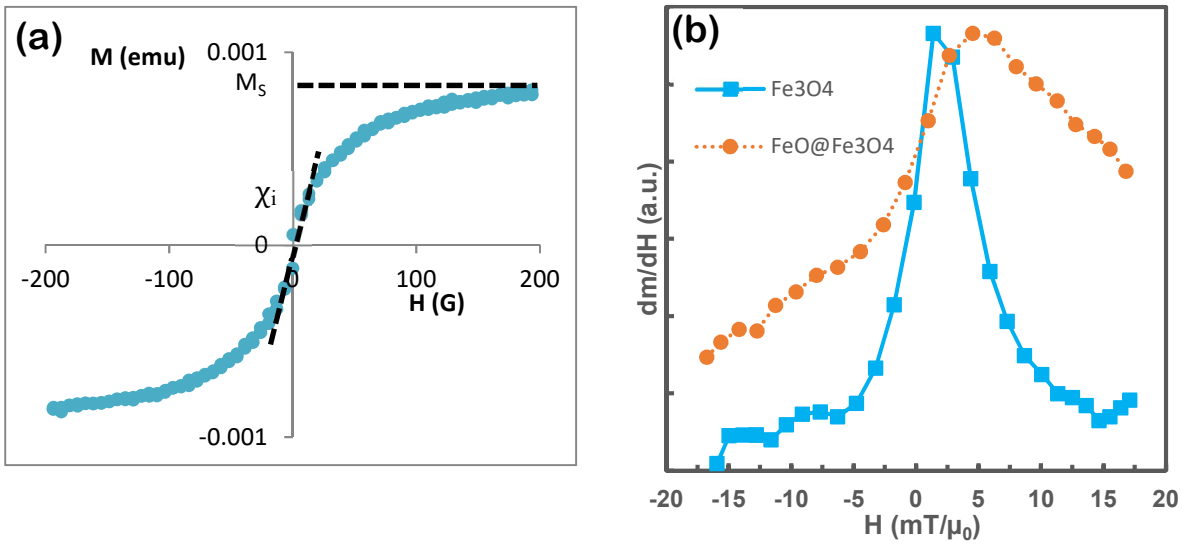

Figure 2.2. **(a)** Magnetization, *M* (*H*), for an ensemble of iron oxide nanoparticles. Characteristic superparamagnetic magnetization curve measured by VSM. These particles have a diameter of 22.01 nm, with a log-normal $\sigma = 0.21 \approx 4.7$ nm, inferred from Chantrell fitting. **(b)** Differential susceptibility (d*m*/d*H*) from iron oxide nanoparticles with comparable physical size ($D_M \sim 25$ nm from TEM) but differing iron oxide phase: pure magnetite (Fe_3O_4), mixed wüstite/magnetite ($FeO@Fe_3O_4$).

The magnetization is measured as a function of applied field using a Vibrating Sample Magnetometer (VSM). A superparamagnetic magnetization curve for iron oxide particles dispersed in chloroform is shown in Figure 2.2. The saturation magnetization, M_S, becomes smaller with increasing size and the susceptibility, χ_i, becomes larger with increasing particle size. By assuming a log-normal size distribution and approximating the superparamagnetic curve as a

Langevin function, the size distribution of superparamagnetic particles in solution can be related to these magnetic properties. [47]

The differential susceptibility, d*M*/d*H*, of two representative iron oxide nanoparticle samples is shown in Figure 2.2**b**. The differential susceptibility is measured using Magnetic Particle Spectroscopy (MPS)—essentially a zero-dimensional MPI scanner. MPS characterizes the response of the imaging system, including the nanoparticle tracers, to a point source, in this case a spatially localized but time-varying magnetic field. This is the point-spread function (PSF) and is predictive of MPI performance. [54] A narrow full-width-at-half-max of the d*M*/d*H* peak is an indicator of resolution in MPI. These plots are normalized, but MPS intensity can be indicative of brightness in MPI. The optimized magnetite sample has a much narrower and distinct peak than the magnetite-wüstite sample, characteristic of a significantly better MPI performance. This measurement was taken at room temperature, above the Néel temperature for wüstite, rendering this phase paramagnetic, which should not contribute to the d*M*/d*H* signal, and thus decreases the mixed phase sample's overall performance. See Chapter 4 for a detailed discussion of the structure of iron oxide nanoparticles.

2.2 Transmission Electron Microscopy

The obtainable resolution of any imaging technique is fundamentally limited by the wavelength of illumination, λ. This is generally defined by the Rayleigh criterion as the diffraction-limited resolution, where the minimum resolvable distance, d, is when the first diffraction minima for one point source overlaps with the maxima for another. Ernst Abbe first described the resolution limit for a light microscope in 1873 in this:

$$d = \frac{\lambda}{2 \sin \alpha}$$

Where α is the semi-angle separating the centers of the two point sources.

An optical microscope, with light on order of hundreds of nanometers cannot observe features below this length scale. When it comes to the study of materials and the relationship between structure and properties, many features of interest are on the atomic scale, ~0.1 nm. While optical microscopes are not capable of resolving features on this scale, electrons can have wavelengths much lower than this. The wave-like nature of electrons was first described by Louis de Broglie in his 1924 thesis.

$$\lambda_{de\ Brogl} = \frac{h}{mv}$$

Where h is Plank's constant, and mv, is the momentum of the particle. For an electron with fundamental charge, e, accelerated by a voltage, V_a, the de Broglie wavelength of an electron can be written as:

$$\lambda_{de\ Broglie} = \frac{h}{\sqrt{2 \cdot m_e \cdot e \cdot V_a}}$$

Further, a relativistic correction is typically required. A 300 keV electron has a wavelength of approximately 2 pm.

A few years later in 1932, the first electron microscope was proposed by Knoll & Ruska. [55] Initial attempts at electron microscopes had lower resolution than optical microscopes. This was soon surpassed, and developments in electron lenses and aberration correction since have made sub-atomic imaging widely accessible. [56] A modern TEM is shown in Figure 2.3.

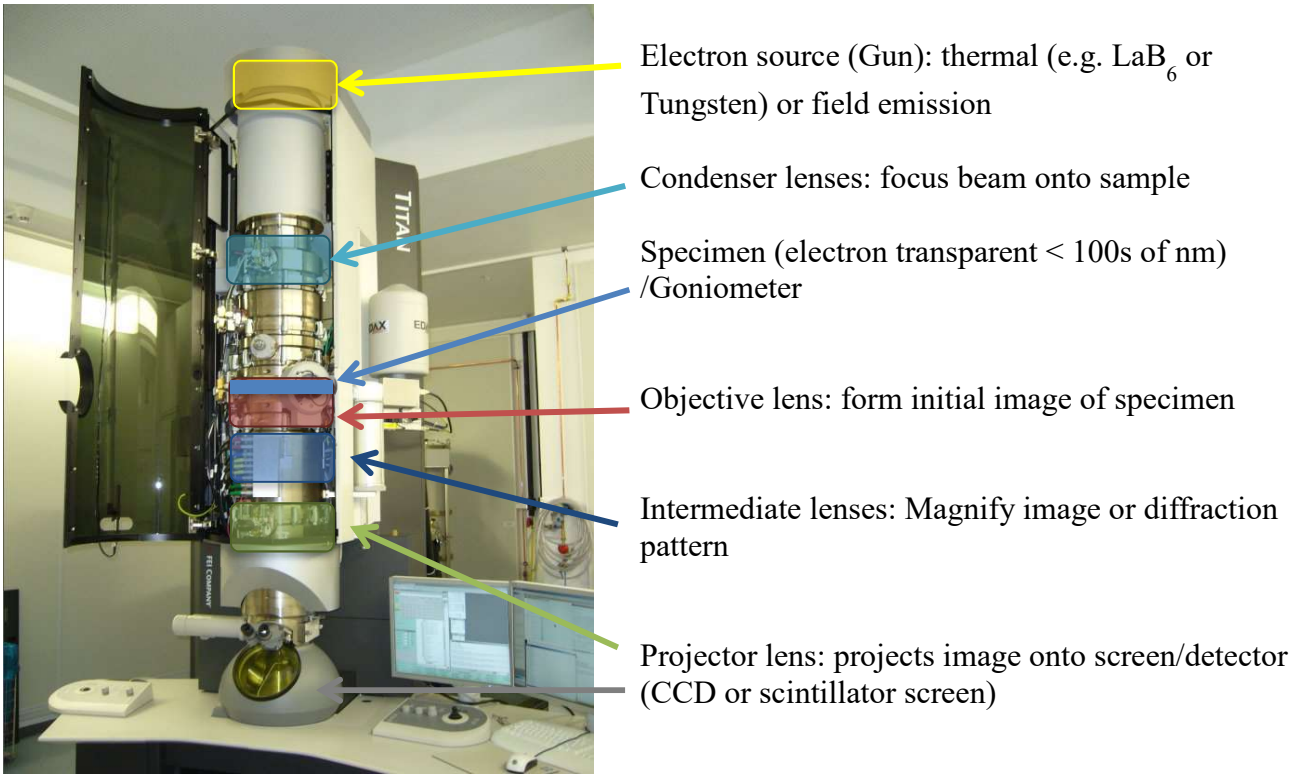

Figure 2.3 Annotated picture of a TEM with descriptions of important components.

In TEM, an electron transparent material is placed in a microscope column under high vacuum. Electrons are generated at the top of the column, either by a filament or a field emission gun (FEG). Source materials, such as tungsten or lanthanum hexaboride (LaB_6), have a high melting point and low work function. The electron beam is focused and modified by a series of electromagnetic lenses, then directed through the sample. Because electrons interact strongly with matter, they will be scattered, often multiple times, transmitting sample information which can be recorded on a scintillator screen or CCD. [56] The variety of signals resulting from electron-specimen interactions are summarized in Figure 2.4.

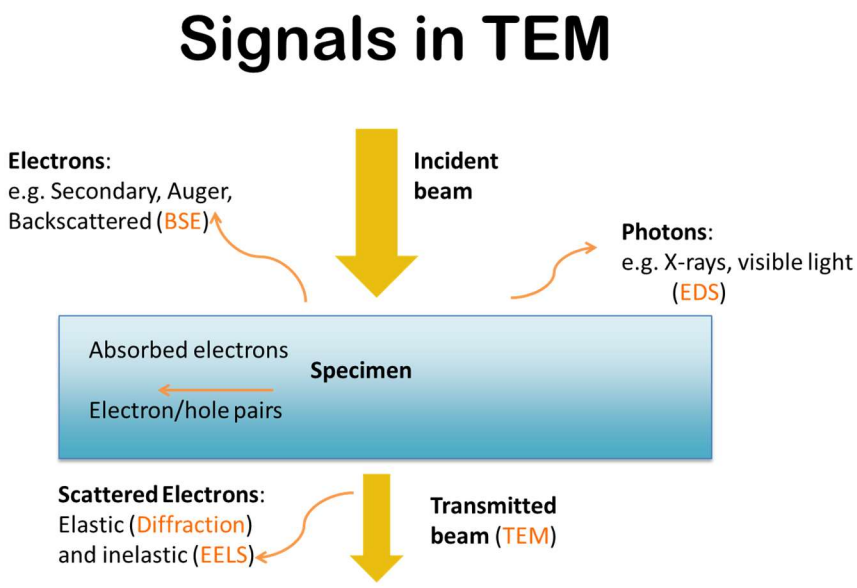

Figure 2.4. TEM is a versatile tool for materials characterization, capable of imaging, diffraction, and spectroscopy in a single instrument.

Many signals are generated in a TEM column, including directly transmitted electrons, forward and backscattered electrons, and various secondary emissions of electrons and electromagnetic radiation. When the transmitted beam is collected, this is called bright field imaging. Conversely, in dark field imaging, scattered electrons are collected.

Conventional TEM illuminates the sample with an approximately parallel beam of electrons. Contrast is generated by interference of scattered and transmitted electrons from variations in both amplitude and phase. Electrons interact with electrostatic potentials in the specimen. Heavier or thicker regions will more strongly scatter and result in amplitude contrast. [56] Interference from Bragg diffraction also gives rise to amplitude contrast. Diffracted beams experience a phase shift, which gives rise to phase contrast, depicted in Figure 2.5.

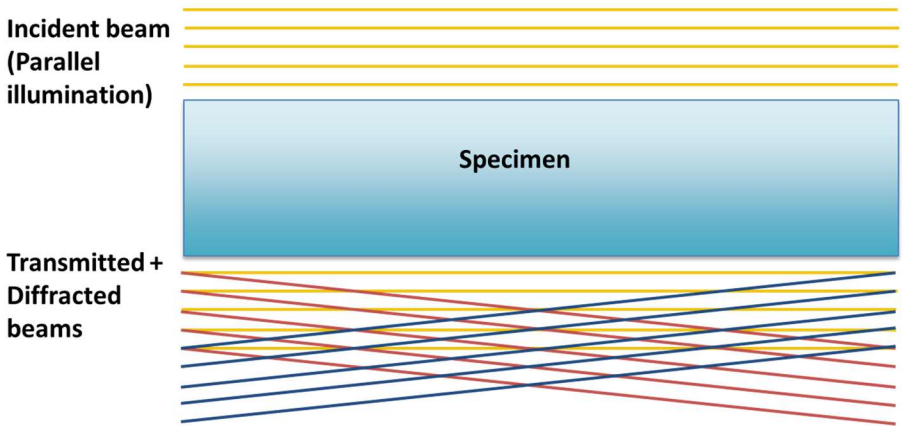

Figure 2.5 In phase contrast imaging, transmitted and diffracted beams are phase shifted after interacting with sample. This leads to the interference pattern visible in high-resolution TEM. While this does transmit atomic information, phase contrast images are difficult to interpret due to the variety of phenomena that can contribute to this contrast.

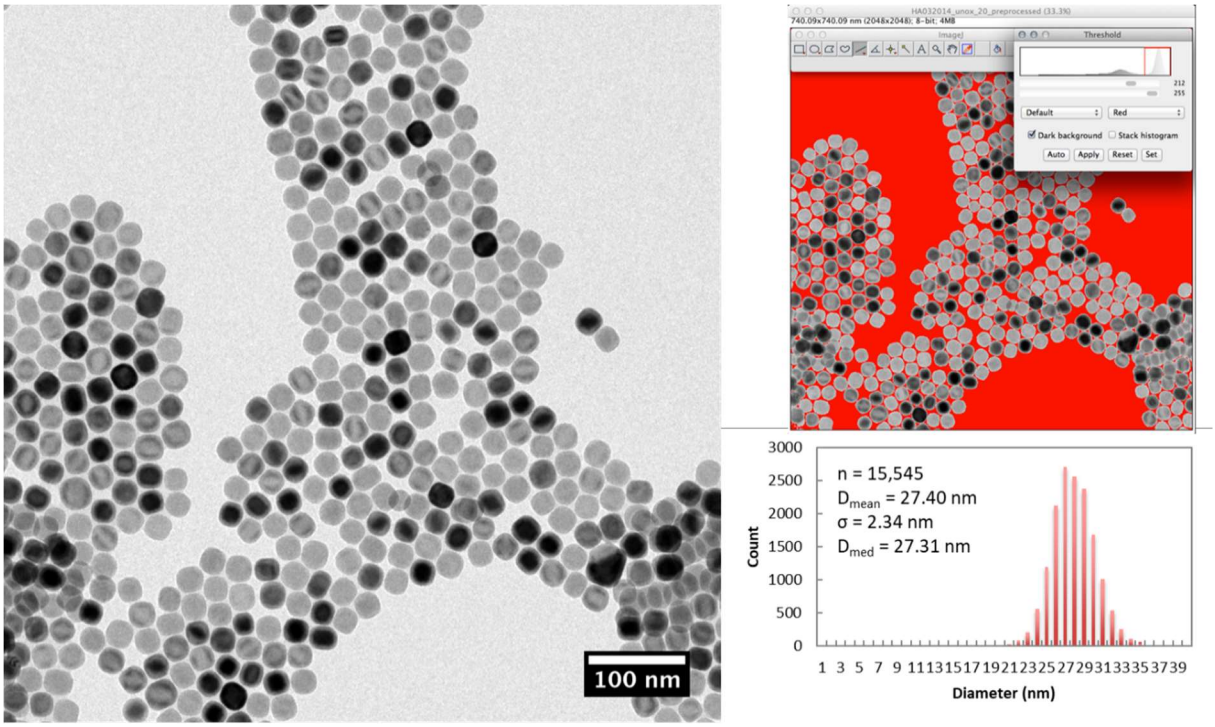

Figure 2.6 Particle size analysis from a bright field TEM image of iron oxide nanoparticles, done using ImageJ. [57]–[59] Automatic thresholding can detect particle edges to count large numbers of particles (here n = 15,545 over many images of this sample), and quantify particle size and size distribution.

In scanning (STEM) mode, lenses converge the beam to a small point of illumination. The STEM beam is rastered across the sample to form an image. In STEM, an annular dark field detector is often used. This is a ring-shaped detector that collects large angle (generally >150 mrad) forward scattered electrons. If an annular detector is used, the space at the center of the column is freed up for other detectors, such as an electron energy-loss spectrometer (EELS). [60] Electron diffraction is also a common use of TEMs. In convergent beam electron diffraction (CBED), pictured in Figure 2.8, forward scattered electrons contain structural information about the sample, where each disc in the diffraction pattern corresponds to a lattice spacing in reciprocal space.

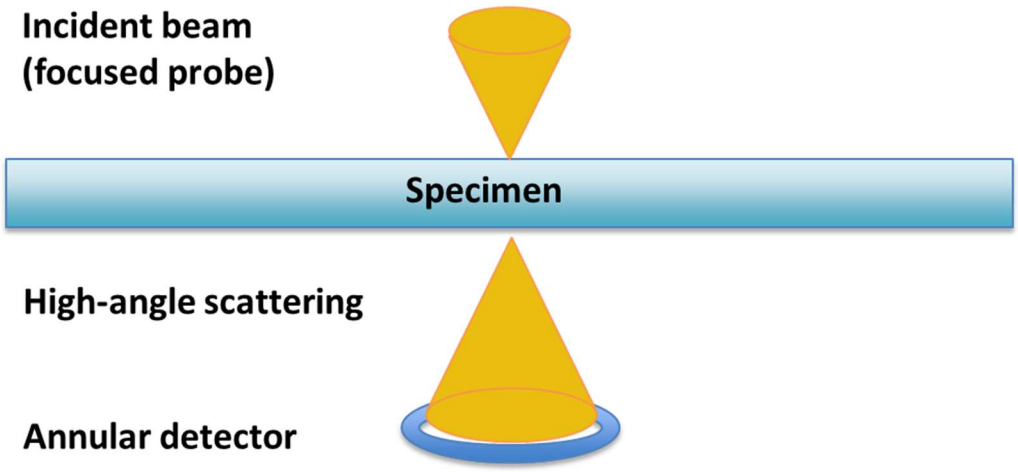

Figure 2.7 STEM geometry.

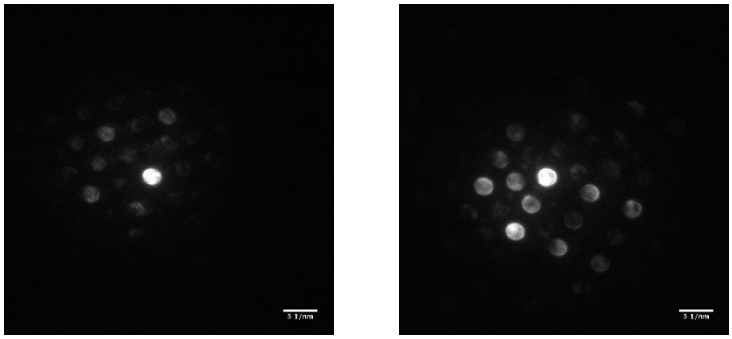

Figure 2.8 Convergent beam electron diffraction spots produced from individual Fe_3O_4 nanoparticles at 2.0 mrad convergence angle. The scattered intensity can be collected on an annular detector, as in STEM, or may be used to determine crystallographic information.

In selected area electron diffraction (SAED), diffracted beams from a particular region of the sample are isolated using a SAED aperture in the TEM. In SAED, the back focal plane is used as the imaging plane, and the reciprocal lattice is projected onto the CCD. Each crystallite produces a diffraction spot from each plane at an angle that satisfies the Bragg condition. In a polycrystalline sample, or in this case hundreds or thousands of single crystalline nanoparticles, a characteristic ring pattern is produced. One dot in each ring represents a single crystallite. This ring pattern is integrated radially to produce a spectrum that can be interpreted in the same way as an X-ray diffraction pattern. The following indexed SAED from iron oxide nanoparticles corresponds to a spinel crystal, with a lattice parameter matching that of magnetite (or maghemite). Combined with Raman spectroscopy, it can be concluded that this sample is magnetite without observable presence of any other phase.

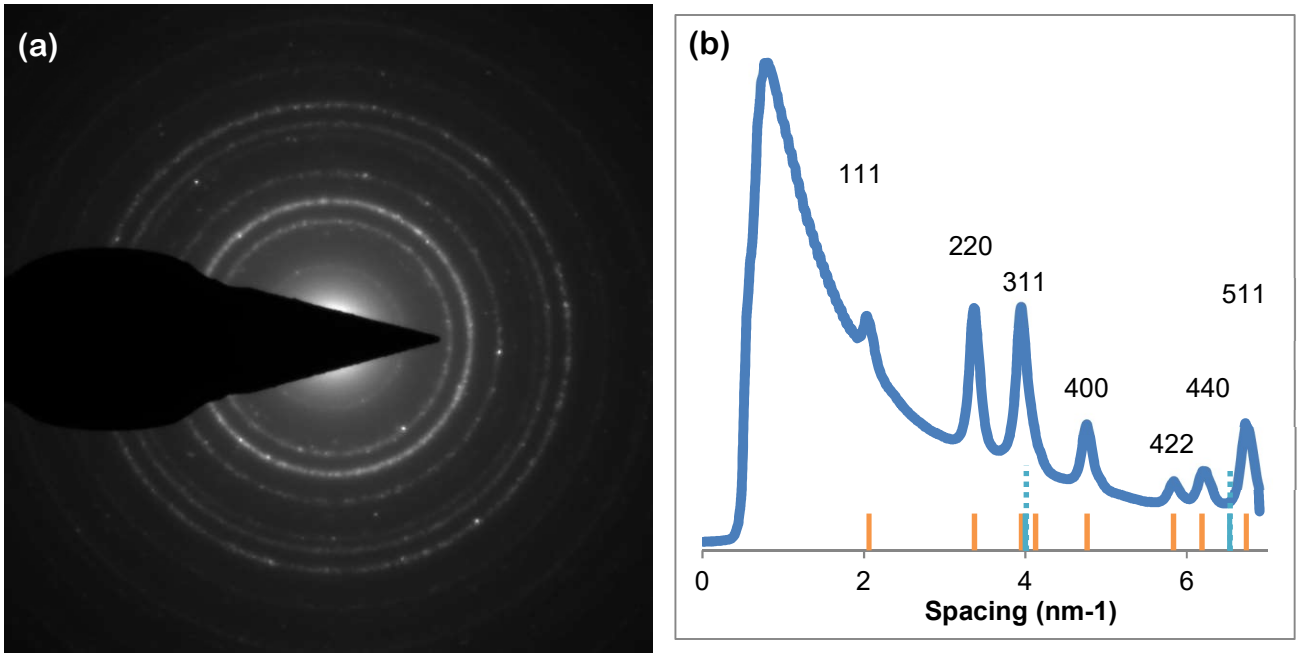

Figure 2.9. SAED of iron oxide nanoparticles, **(a)**, and radially integrated intensity, **(b),** with peak positions indexed for magnetite (orange) and wüstite (blue with dashes) appear as ticks along the axis. The indexed peaks in the spectrum correspond to magnetite lattice planes.

Aberrations typically limit the obtainable resolution in electron microscopes. The primary aberrations of concern in TEM are spherical aberrations, chromatic aberration, coma, and astigmatism. Small octupole electromagnetic lenses called “stigmators” correct for astigmatism and coma in a TEM. Spherical aberration is a primary limiter of resolution, see Figure 2.10, and much effort has been put into its correction. [61], [62] Spherical aberration correction is now standard in many high-resolution microscopes.

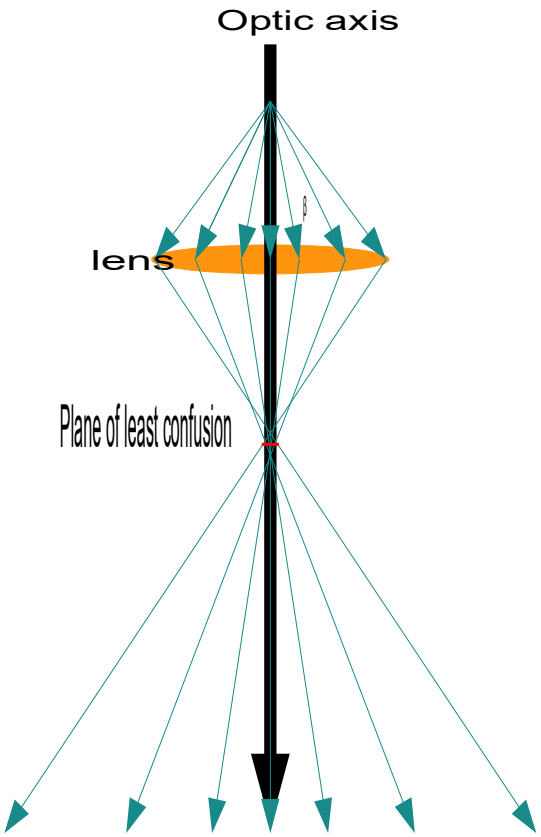

Figure 2.10. Spherical aberration is caused by off-axis rays interacting more strongly with the lens. Instead of a focal point, the smallest probe formed by this lens or lens system is located at the “plane of least confusion.”

Other issues of concern are environmental and power stability. Modern power sources are very reliable, but stability of power supplies during initial development of microscopes was a

major concern. [56] Minute vibrations, temperature fluctuations or other instabilities can limit the resolution of microscopes. The microscopes in EMSL[2] are located in a "quiet wing," with a separate foundation, vibration damping, electromagnetic shielding and other protections to address these stability concerns.

Recently, sample holders have been developed to allow for imaging of liquid and gas phase samples. [63]–[65] The most commonly used holders consist of a sealed sample chamber with a pair of electron-transparent windows, usually SiN, for example, as manufactured by Hummingbird Scientific Inc. Graphene liquid cells have been demonstrated, but remain less tested and presumably less robust. [66] *In situ* TEM is discussed in Chapter 5.

In order to extend temporal resolution, dynamic TEM (DTEM) makes use of ultrafast laser pulses to excite the electron source. [62], [67] DTEM is capable of imaging on the time scales relevant in chemical reactions and opens a wide range of unobserved phenomenon to study. Additionally, by using a secondary laser pulse to excite the sample, the reaction can be precisely coordinated with imaging, and electron beam damage can be minimized. This method is called pump-probe. With the recent developments in both high-speed TEM and liquid/gas phase sample holders, *in situ* microscopy is poised to answer many fundamental questions in materials science.

2.2.1 *High Resolution TEM*

High resolution, particularly atomic resolution, TEM can provide unique insights into particle morphology. Figure 2.11 and Figure 2.12 depicts HRTEM images of iron oxide nanoparticles. The Fourier transform shows the periodicity present in the original image, with a

---

[2] A portion of the research was performed using the William R. Wiley Environmental Molecular Sciences Laboratory (EMSL), a US DOE national scientific user facility sponsored by the DOE's Office of Biological and Environmental Research and located at Pacific Northwest National Lab.

set of spacings (usually lattice planes) represented as a single spot in the transform. This can be interpreted much like a diffraction pattern, however the Fourier transform requires the periodic lattice planes to be resolved in the image. Indexing the transform allows crystallographic directions and faceting to be interpreted. The smallest (12 nm) particle is very spherical, while the larger particle on the right shows much more pronounced faceting. It appear that faceting is more prevalent in larger nanoparticles, which is to be expected as surface area and surface energy increase with r^2, while the surface-to-volume ratio decreases. Figure 2.13 shows simultaneous bright field and dark field STEM images of an iron oxide nanoparticle.

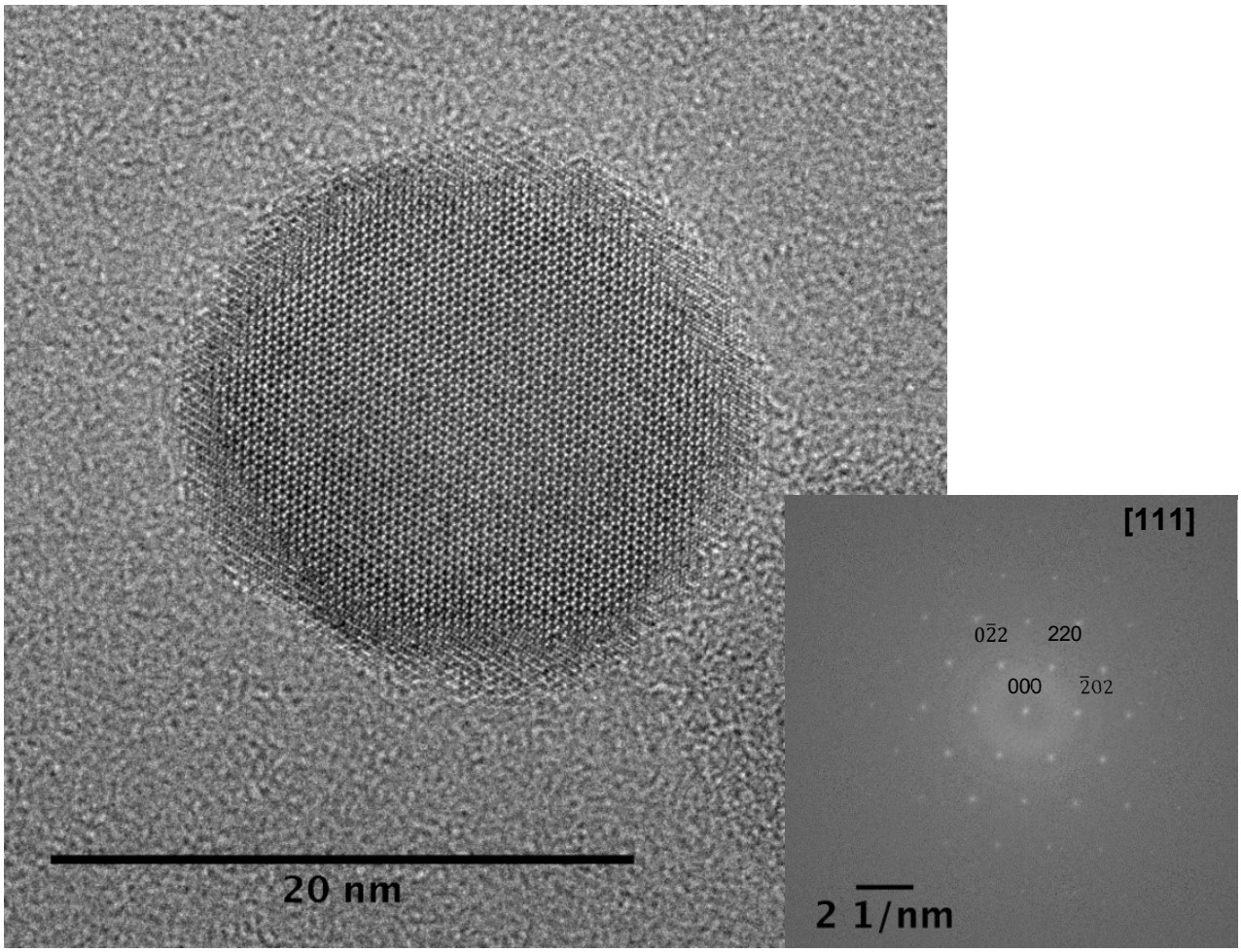

Figure 2.11. High-resolution TEM and FFT, indicating alignment with [111] zone axis.

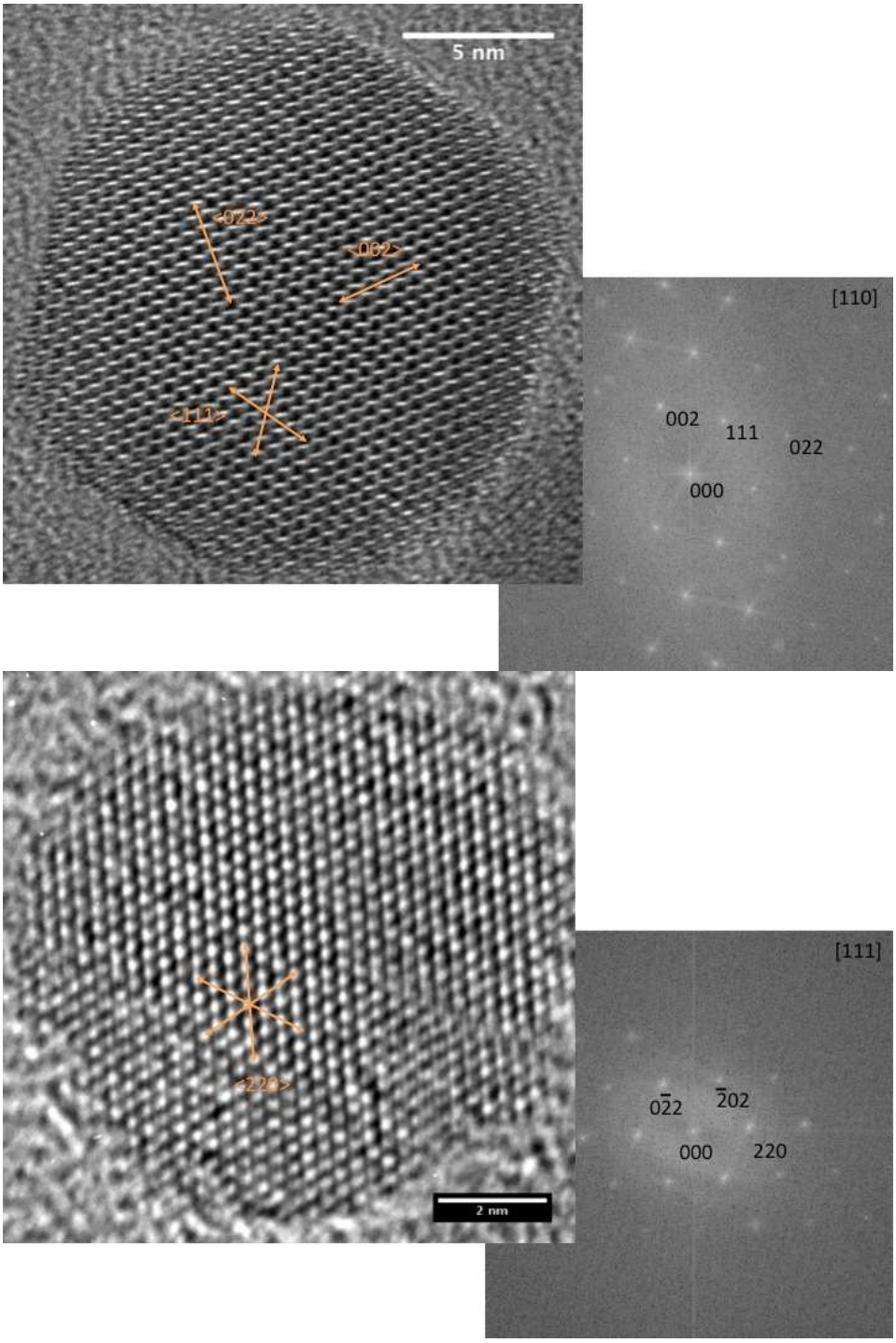

Figure 2.12. High-resolution TEM of iron oxide nanoparticles, with indexed Fourier transforms indicating orientation. The top is aligned along the [110] zone axis, while the bottom is aligned along the [111] zone axis. The corresponding crystallographic directions are marked as arrows in the real-space image, and appear as the indexed spots in the transformed image.

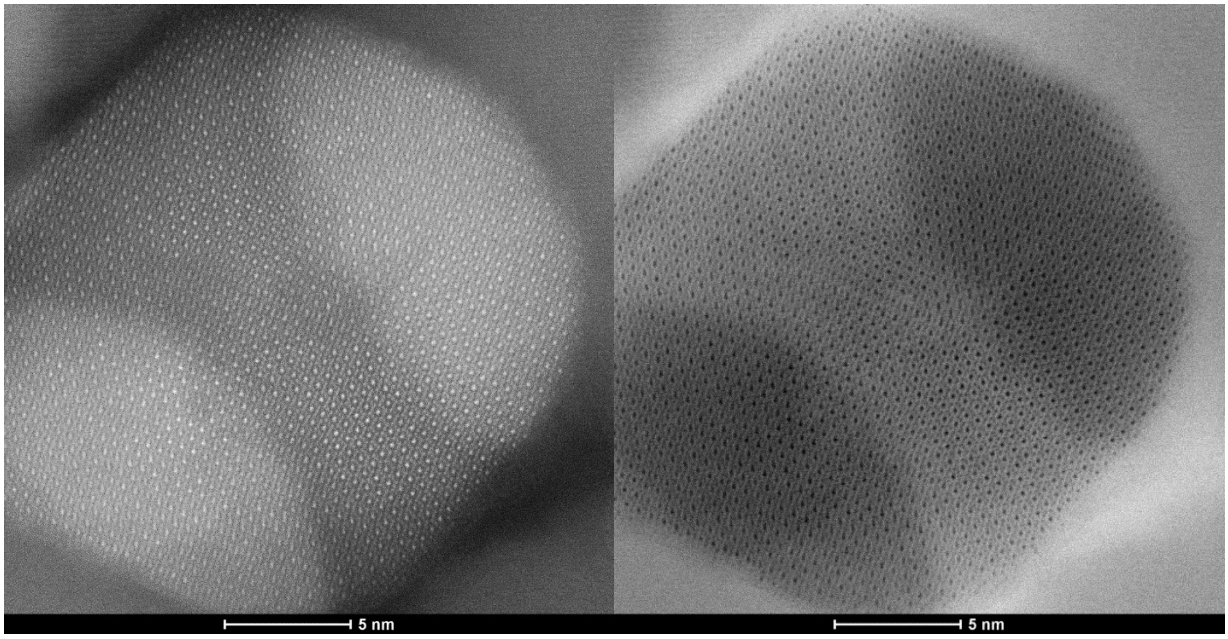

Figure 2.13. Atomic resolution HAADF (left) and bright field (right) STEM iron oxide nanoparticle oriented along the [110] zone axis. This particle is overlapping with two others, hence the increased brightness due to the extra thickness.

2.2.2 *Electron Energy Loss Spectroscopy*

In the TEM, a beam of monochromatic, high energy electrons are incident on a specimen. This beam may be a focused into a small (<1Å) probe as in STEM. The electron beam scatters inelastically due to Coulombic interactions with electrons in the specimen, and energy lost by the beam is absorbed by the specimen. The electron energy spectrum is measured after interacting with the sample, providing a characteristic excitation spectrum for the material. Electron energy loss spectroscopy (EELS) measures electronic excitations in materials. Energy losses typically range from 0 to 3 keV. Energy resolution ranges from several eV, to 0.3 eV for a cold-FEG, down to less than 10 meV for a very stable, monochromated beam. [68]–[70] The FEI Titan 80-300™ and JEOL ARM used throughout these experiments are equipped with a Gatan Image Filter and Electron Energy Loss Spectrometer. The JEOL is equipped with a cold-FEG and has an energy

resolution of 300 meV, while the FEI microscope has an energy resolution of 1-3 eV unless the beam is monochromated.

The various processes that result in energy transfer and their prevalence depend on the material. The most prominent feature is typically the zero-loss peak (ZLP), consisting of electrons that give no energy to the sample. Depending on specimen thickness, most of the electrons will not be scattered, or will elastically Bragg scatter. With a probability that depends on electron energy and sample composition and thickness electrons will inelastically scatter, depositing energy in the specimen—exciting plasmons, electronic transitions, or ionizing the specimen. Plasmonic excitations are low energy (10s of eV) collective oscillations of valence electrons in the material and typically dominate the inelastic scattering. Core loss events are the excitation of inner electrons, with an energy-loss characteristic of the scattering atom. Additionally, core loss fine structure is altered by bonding and the local environment. Above an absorption edge an extended fine structure arises due to backscattering: self-interference of excited electrons as they scatter.

Core loss features are called "edges" (as opposed to peaks) because the transition can be excited by any energy above some threshold, with diminishing probability. Because of this, the background from edges must be subtracted from any overlapping features.

2.2.3 *Thickness Effects*

Probability for inelastic scattering depends on sample thickness and the mean free path in the material, λ. The specimen thickness, t, can be estimated from the relative intensities of the zero-loss peak, I_T, to the rest of the energy loss spectrum, I_0: [71]

$$t = \lambda \ln\left(\frac{I_0}{I_T}\right)$$

In Figure 2.14, for example, experimental EEL spectra for an approximately 200 nm H_2O layer is compared to a 1000 nm water layer, both with 2x50 nm Si_3N_4 membranes. The mean free path is calculated as follows:

$$\lambda = E_M \ln\left(\frac{2\beta E_0}{E_M}\right)$$

Where β is the collection angle, E_0 is the accelerating voltage, and $E_M = 7.6\, {Z_{eff}}^{0.36}$. The effective atomic mass, Z_{eff}, includes the Si_3N_4 and water. Because Z_{eff} is a function of the thickness, i.e. the ratio of water: Si_3N_4, this calculation was iterated until the calculated thickness converged within appropriate error (usually < 0.1 nm).

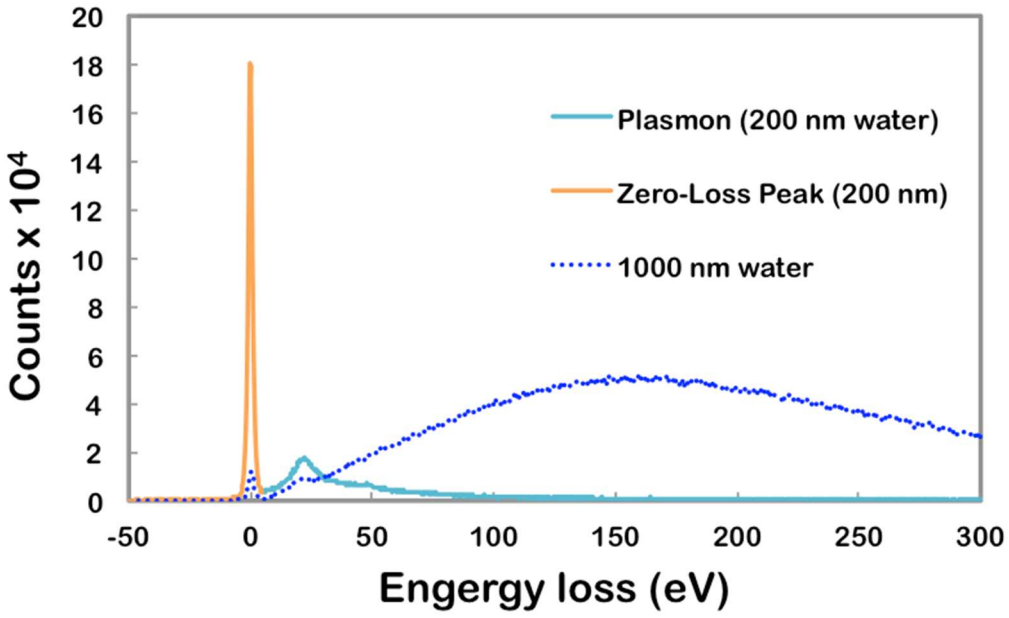

Figure 2.14. The low-loss region of the electron energy loss spectra is dominated by the zero-loss peak. The ratio of the intensity of the ZLP to the rest of the spectra is proportional to thickness of the sample, here water, between two 50 nm silicon nitride membranes.

2.2.4 *Quantification of Core-Loss Spectra*

In EELS, the energy of the electrons after interacting with the sample is measured by a magnetic sector spectrometer, that spreads the transmitted electrons by their energies and collects the resulting spectrum on a detector. Most of the electrons pass through with their energy unchanged. This forms the "zero-loss" peak, followed by gradual decay back to baseline. When energy approaches the onset of an energy transition within the material, such as an electronic transition, there will be an increase in the number of electrons associated with this energy loss, followed by any fine structure, or field splitting, and a gradual decay back to baseline. These energy loss edges can be quantified to interpret the electronic structure of the sample; relative intensities, for example of the iron L edge in Figure 2.15 below, depend on the occupancy of their corresponding electronic states. Fine structure, i.e. of the oxygen K edge, contains information on structure, bonding, and coordination.

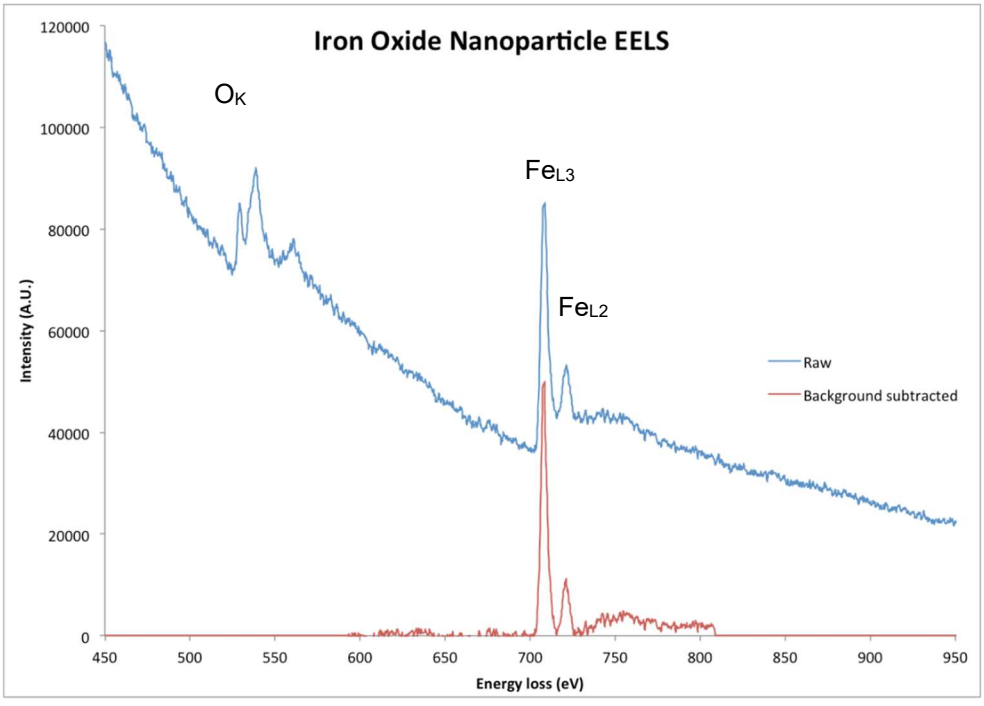

Figure 2.15. EELS of iron oxide nanoparticle sample

For the iron oxide sample shown in Figure 2.15 the most useful edge for quantification of iron chemistry are the iron L_2 and L_3 transitions, or white lines. These correspond to transitions to the partially filled 3d shell, from the 2p shell, with $l + s = ½$ and *3/2*, respectively. These should theoretically have an intensity ratio of 1:2, corresponding to the population of the 2p states. However, the nature of the 3d shell, including valence and field splitting, affects the probability of L_2 relative to the L_3 transitions. This ratio can be calculated to determine the oxidation state of iron, see Figure 2.16.

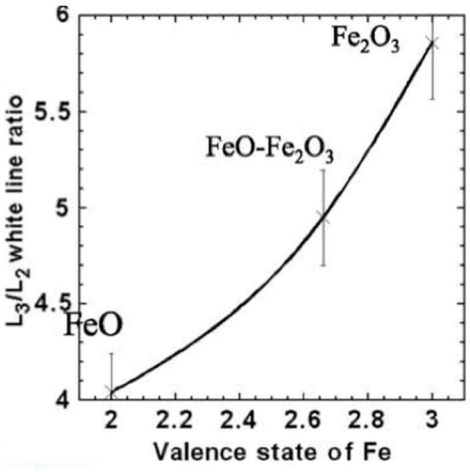

Figure 2.16. The relative intensity of the iron L_3/ L_2 edge correlates with valence in iron oxide phases. Figure courtesy of Nigel Browning. [72]

To quantify a spectrum, some data processing is usually necessary. Firstly, the background is removed by fitting to a power law function ($I = aE^{-k}$) to the ZLP. The background from core-loss features can be modeled as a step function, or involve more detailed quantum mechanical models such as the Hartree-Slater Cross section. [73] After subtracting the background from the EELS spectra, the peaks can be fit to a Gaussian function by a linear least squares regression. Alternately, numerical integration can be less computationally demanding and has been employed frequency in the literature. For Figure 2.15 the integrated intensity in a 2 eV window centered at

each iron L-edge peak is computed, and the ratio calculated is 4.55. Comparing to literature, this corresponds to an average iron valence of approximately 2.5. [72] Magnetite should have 2.75, so this sample may have a slight excess of iron(II).

When measuring low concentrations, it is sometimes useful to apply filters to enhance visibility of weak edges. If the signal to background ratio is poor (< 0.01), small systematic errors in background fitting can be extrapolated into the post-edge spectrum. In this case, the integration window should be restricted to a width approximately the same size as the dominant feature, for example a "white line" in a transition metal.

The first-difference spectrum is the difference between two spectra shifted electrically, by small voltage Δ. If $I(E_n)$ is the intensity corresponding to energy E_n, then the first difference is:

$$I'(E_n) = I(E_n + \Delta/2) - I(E_n - \Delta/2)$$

This is similar to taking the first derivative of the spectrum, and it enhances small features relative to a slowly varying background. If the energy shift, Δ, is approximately the same size as the feature of interest signal-to-noise will improve.

Similarly, the second-difference spectrum, taken by combining three spectra offset sequentially by Δ is given by:

$$I''(E_n) = I(E_n) - I(E_n + \Delta)/2 - I(E_n - \Delta)/2$$

This is similar to the negative second-derivative. Because the same peaks appear in the second-difference spectrum as in the original it can be easier to interpret than the first-difference, and has improved signal-to-noise from the original spectrum. [74], [75] Compare the spectrum to its second-difference in Figure 2.17. While modern detectors are generally sensitive enough to alleviate need for such methods, using digital filters after acquisition can enhance edge visibility and improve detection efficiency. [76] Here, the integrated intensity of the iron L_2 and L_3 peaks

were measured from the second derivative of the raw spectrum using numerical filters available in Gatan Digital Micrograph, with a 4.1 eV positive and 1.7 eV negative window width.[72], [77]

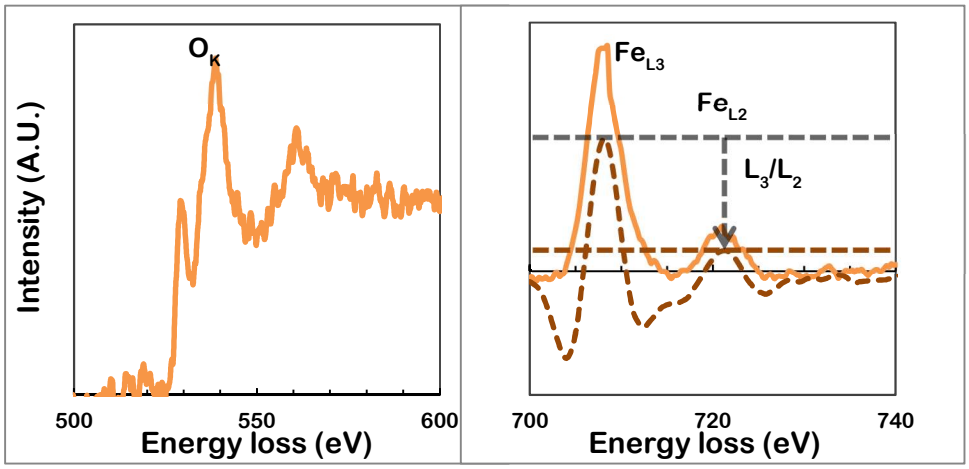

Figure 2.17. Core-loss electron transitions at the oxygen K-edge, and iron L-edge. Iron L-edge transitions depend on the occupancy of iron 3d levels. The solid line shows the background subtracted spectrum, while the dashed line shows the second-difference spectrum.

For the experiments to quantify iron valence and oxidation state, STEM was performed using a JEOL ARM 200CF, with a cold field emission gun operated at 200 kV equipped with a Gatan Image Filter (GIF) and EELS spectrometer. The probe was aberration corrected, with a probe-forming aperture selected to produce a ~1.4 Å STEM probe with a 23 pA probe current. The convergence angle was 27.5 mrad, and EELS collection angle was approximately 82.6 mrad. This also corresponds to the starting angle of the Gatan annular dark field (ADF) detector.

2.3 SUMMARY

To summarize, materials can be characterized in several ways. 1) Samples can be imaged at relevant length scales to directly observe morphology and structure. 2) Diffraction experiments "image" crystals in reciprocal space, characterizing their structure. Or 3) spectroscopies can be used to characterize a material's interaction with electromagnetic probes, which is sensitive to, for example, chemistry, structure, or bonding, depending on the technique. Sometimes materials are characterized in terms of their properties, for example their magnetic performance. In this chapter we have surveyed the techniques that will be used in this work, describing their basic principles and providing examples of results.

Iron oxide nanoparticles can form with a variety of phases, with overlapping structure and chemistry. In order to fully characterize a sample, complementary characterization techniques are typically necessary. That is, it is helpful to combine structural characterization (diffraction), chemical analysis (spectroscopy), and direct imaging at relevant length scales. This is usually in concert with magnetic measurements. Throughout this work, I will use a strategic combination of these described characterization techniques to relate structure and chemistry to the synthesis, processing, and resulting properties of nanoparticles. In the following chapter, I will describe the synthesis of superparamagnetic iron oxide nanoparticles.

Chapter 3. SYNTHESIS OF SUPERPARAMAGNETIC IRON OXIDE NANOPARTICLES

Superparamagnetic iron oxide nanoparticles (SPIONs) are used for a wide range of biomedical applications requiring precise control over their physical and magnetic properties, which all depend on their size and crystallographic phase. This chapter presents a comprehensive template for the design and synthesis of iron oxide nanoparticles with control over size, size distribution, phase, and resulting magnetic properties.[3] These experiments investigate critical parameters for the synthesis of monodisperse SPIONs by organic phase thermal decomposition. Three different, commonly used, iron containing precursors: iron oleate, iron pentacarbonyl, and iron oxyhydroxide, which all share iron oleate as a starting precursor or reaction intermediate, are evaluated under a variety of synthetic conditions. The suitability of these three kinetically controlled synthesis protocols are compared for producing nanoparticles with specific size and magnetic properties. Monodisperse particles were produced with tunable size from approximately 2-30 nm. Reaction parameters such as precursor concentration, addition of surfactant, temperature, ramp rate, and time are adjusted to kinetically control size and size-distribution, phase, and magnetic properties. In particular, large quantities of excess surfactant (up to 25:1 molar ratio) alter reaction kinetics and result in larger particles with uniform size; however, there is often a trade-off between large particles and a narrow size distribution. Iron oxide phase, in addition to nanoparticle size and shape, is critical for establishing magnetic properties such as differential susceptibility (*dm/dH*) and anisotropy. Obtaining the required size and iron oxide phase is

---

[3] Portions of the following chapter were published as "Synthesis of Phase-Pure and Monodisperse Iron Oxide Nanoparticles by Thermal Decomposition" by Ryan Hufschmid, Hamed Arami, R. Matthew Ferguson, Marcela Gonzales, Eric Teeman, Lucien N. Brush, Nigel D. Browning, and Kannan M. Krishnan in *Nanoscale* 7, no. 25 (2015): 11142–54

important for successful application of SPIONs, for example in Magnetic Particle Imaging (MPI). These results provide much of the information needed to determine the best suited iron oxide synthesis protocol for a specific application.

3.1 Applications for SPION and Considerations for their Synthesis

SPIONs have suitable magnetic properties and biocompatibility for a variety of biomedical applications, ranging from imaging to diagnostics, targeting, and therapy. [1] Iron oxide nanoparticles are generally safe for intravenous injection, with years of clinical history, [78]–[80] and multiple examples of clinically approved iron oxide nanomaterials for various applications. [79], [81] The mononuclear phagocyte system captures and clears foreign objects such as iron oxide nanoparticles, which will eventually enter the body's iron metabolism. Iron oxide particles can be tailored for long circulation times with no expected renal involvement in clearance by tuning their hydrodynamic sizes to 15-100 nm. [82], [48], [46] This is particularly important as many current imaging platforms such as iodine-based X-ray and computed tomography (CT) contrast agents and gadolinium-based MRI contrast agents are cleared by the kidneys and cause significant morbidity in patients with chronic kidney disease. [83]–[86] SPIONs have been applied as T_1 and T_2 MRI contrast agents[87], and several compounds have received regulatory approval for clinical use. [79], [81] SPIONs have additionally been used as contrast agents for photoacoustic imaging.[88] Therapeutic applications using the magnetic response of the SPIONs have also been proposed, for example, magnetic fluid hyperthermia (MFH). [24], [51] A recent interest in SPION tracers has focused on Magnetic Particle Imaging (MPI), a novel real-time whole body imaging modality developed by Philips in 2005. [4] Since then, much progress has been made in optimizing synthesis of monodisperse SPION tracers with median core sizes tuned for MPI. [89]–[91]

Particle size, size distribution, phase, morphology, and interactions with immediate environment determine SPION magnetic properties and must be tailored to the specific application. [2], [31] For example, 16 nm SPIONs were shown to be optimal for MFH (with a 373 kHz, 14 kA/m field), with broader distributions decreasing heating efficiency.[92] Monodisperse 24-26 nm SPIONs have shown significantly improved MPI performance (*i.e.* enhanced signal intensity and spatial resolution) at 25 kHz, with smaller 15 nm particles showing better performance at 250 kHz.[89], [90] This is consistent with theoretically modeled MPI tracer performance, although the precise optimal size is dependent on magnetocrystalline and shape anisotropies.[48], [49] In MRI, relaxivity refers to the concentration dependence of a tracer's relaxation time. For T_1 MRI contrast, ultrasmall (<5nm) SPIONs are optimal due to increased r_1 relaxivity, attributed to high surface concentrations of Fe^{3+}. [93] For T_2 MRI contrast, larger SPIONs have shown improved r_2 relaxivity. [94] These applications rely on superparamagnetic behavior of the nanoparticles, generally requiring phase-pure and size-tuned magnetite (Fe_3O_4) or maghemite (γ-Fe_2O_3). Presence of antiferromagnetic wüstite (FeO) or hematite (α-Fe_2O_3) phases significantly reduce performance for most of these applications. Because the size, distribution, and magnetic properties are a direct result of the nanoparticle synthesis, it is necessary to understand how synthetic conditions impact nanoparticle nucleation and growth. Determining and monitoring critical synthesis parameters such as temperature, time, and precursor concentrations also improves reproducibility of SPION synthesis to achieve the required phase and core sizes desired for each application.

Much of the nucleation and growth behavior of these nanoparticle systems can be qualitatively interpreted with classical theories. LaMer supersaturation [95] and Ostwald ripening [96] processes explain much of what is observed, especially in synthetic methods that are

kinetically controlled. More complete models that predict a wider possible range of growth behaviors models have been developed that account for competing diffusion and adsorption rates of growth species. [97], [98] Nucleation and growth models have long been established in the limiting cases of diffusion and interface reaction controlled growth, [98] and more recently in a fully coupled treatment bridging the gap between these two limits. [97] See Appendix A for a review of nucleation and growth models. Diffusivity, reaction coefficient, and surface energy data are not always available for these systems and experimental measurements of these parameters are not always feasible. Nonetheless, it is important to consider how synthetic parameters influence nucleation and growth rates, and how this affects the final crystal structure, morphology and properties of the nanoparticles.

There are several approaches to nanoparticle synthesis, with varying degrees of synthetic control over size and size distribution. Many metal nanoparticles have been produced by aqueous reduction of metallic salts.[10]–[15] Multicomponent nanoparticles, in this case iron oxides, such as Resovist® and Feridex®, can be synthesized by similar aqueous co-precipitation reactions;[16], [17] however, organic phase syntheses generally provide the highest degree of control over size and monodispersity.[18]–[21] These organic phase syntheses typically rely on the decomposition of iron carboxylate salts (e.g. iron [III] oleate), which plays a critical role in the kinetics of the subsequent nucleation and growth processes.[18], [19], [99] Although other precursors have been explored, for example iron oxyhydroxides including goethite or ferrihydrites, iron carboxylates likely form as intermediates in these reactions as well.[99]–[101] The solvent and surfactant can be substituted with other similar fatty acids to adjust the boiling point and subtly alter surface energies for shape control, or oxidation strength for phase control.[102] Presence of impurities can similarly impact the reaction. For example, adding sodium oleate to iron oleate produces wüstite-

magnetite core-shell nanocubes.[103] Because most biomedical applications require phase-pure, spherical SPIONs we use clean glassware and high-purity chemicals to minimize impurities and maximize reproducibility of synthesize.

Here we evaluate and compare iron oxide nanoparticle synthesis from the decomposition of three common iron containing precursors — iron (III) oleate ($Fe[C_{18}H_{33}O_2]_3$), iron oxyhydroxide (FeOOH), or iron pentacarbonyl ($Fe[CO]_5$). These precursors have been selected for comparison because they have been widely used in the synthesis of monodisperse iron oxide nanoparticles by thermal decomposition, and formation and decomposition of iron oleate is critical to all three reactions.[18], [19], [99] While these individual protocols have been previously reported, they have not been compared nor evaluated for their capability to produce iron oxide nanoparticles with specific size and phase-purity requirements. We find that the iron pentacarbonyl synthesis is particularly suited for producing small (<10 nm) SPIONs. Iron oleate can also be used to synthesize small particles, while both iron oleate and oxyhydroxide are suitable for producing larger (10-30 nm) particles. Magnetic and crystalline properties of many nanoparticles are improved by post-synthesis annealing, but this is especially necessary in the iron pentacarbonyl protocol or synthesis of nanoparticles larger than 22nm (with FeOOH or iron oleate methods), where wüstite phase impurities are common. To uniquely determine iron oxide phase, complementary characterization techniques are generally necessary. In this work, X-ray (XRD) and selected area electron diffraction (SAED), Raman spectroscopy, and Electron Energy Loss Spectroscopy (EELS) are used together to characterize SPION phase and phase-purity.

3.2 NANOPARTICLE SYNTHESIS

Magnetite (Fe_3O_4) nanoparticle cores are synthesized by thermal decomposition in organic solvents. Three different precursors have been investigated in the Krishnan Research Group: iron (III) oleate, iron pentacarbonyl, and iron oxyhydroxide, with synthesis protocols adapted from literature. [18], [19], [99] Typically excess surfactant, *i.e.* oleic acid, is added to adjust growth kinetics and tailor size and distribution. We primarily use the surfactant/solvent combination of oleic acid and 1-octadecene for simplicity, ease of comparison, and due to their widespread use for the synthesis of iron oxide nanoparticles. Particles are characterized according to their size, size distribution, morphology, phase, and magnetic properties. An additional controlled oxidation procedure is performed after synthesis when needed to optimize phase purity and magnetic properties. As-synthesized particles are terminated with oleic acid and are hydrophobic and can be kept in organic solvents such as chloroform and hexane for characterization. For most biomedical applications SPIONs are made water soluble by an aqueous phase-transfer procedure. [92], [25], [30], [104] As-synthesized oleic acid terminated nanoparticles are transferred to aqueous phase by coating them with a copolymer of poly(maleic anhydride-*alt*-1-octadecene) and poly(ethylene glycol) (PMAO-PEG). [105], [106] PEG provides a platform for surface functionalization with various functional groups.

These organic phase syntheses typically include a precursor that decomposes rapidly to produce metal cations, plus the addition of surfactants and anti-flocculating agents. Traditionally, one component is rapidly injected into the other, which is held at elevated temperature. The injected precursor quickly decomposes, increasing concentration and producing a nucleation burst, ideally resulting in monodisperse particles. While capable of producing particles with uniform properties, the injection step results in non-uniform mixing, and increases the likelihood for

heterogeneous nucleation. Additionally, if not properly automated an injection step introduces potential for human error into synthesis. Piercing the reaction vessel may expose the reaction to atmosphere. Injection rate and technique are additional variables with inherent reproducibility issues when not automated and human beings are involved. Furthermore, injection may not be scalable, since mixing takes longer in larger vessels. Other recent methods have used different precursors, which are stable when mixed at ambient conditions. The addition of excess surfactant can alter reaction kinetics providing additional synthetic control.

Other iron oxide and hydroxide systems are studied, including goethite (FeOOH) synthesized by Christina J. Newcomb, [12] and the self-assembly of iron Keggin ions (Fe_{13}), synthesized by Omid Sadgheti and May Nyman. [13] See the relevant publications for synthetic protocols, and §5.3 for *in situ* experiments of these systems.

3.2.1 *Synthesis of the Iron Oleate Precursor*

Synthesis of the iron oleate precursor begins with iron(III) chloride ($FeCl_3 \cdot 6H_2O$, Alfa Aesar, 97-100%) and sodium oleate (TCI, 95%) are dissolved in a 4:3:7 ratio solution of ethanol, DI water, and hexanes, with about 300 mL for 10 g $FeCl_3$. This dissolution is exothermic. Dissolved $FeCl_3$ is stirred in a round bottom flask and 50 g of excess oleic acid is added for the batch size described. This solution is titrated with NaOH in methanol. This increases the pH of solution and favors formation of iron oleate complexes. Iron remains in the 3+ oxidization state, but the chloride ions have been exchanged for oleate ligands. After titration, the solution is left to stir for several hours, or overnight, but iron oleate should already be precipitating out. Alternately, the solution can be heated under argon to reflux and held for four hours to form the iron (III) oleate complex. At this point, iron oleate has essentially been synthesized, however cleaning and purification are important to produce a uniform precursor for predictable synthesis of

nanoparticles. The resulting product is then transferred to a separating funnel and the denser, aqueous layer is removed. The remaining organic layer is washed with DI water three times. After washing, the solution is dried with sodium sulfate (anhydrous, Sigma Aldrich) and any remaining solvent is removed in a Rotovap followed by evaporation under argon and/or vacuum, leaving behind the iron (III) oleate complex. The iron (III) oleate is finally dissolved in 1-octadecene (Alfa Aesar, 90%) at the desired molar ratio (0.1698 mmol/g, unless noted) to form the precursor solution.

3.2.2 *Synthesis of Magnetite Nanoparticles*

The most common approach to the synthesis of iron oxide nanoparticles relies on the thermal decomposition of an organometallic precursor. This synthesis was first described by Park and colleagues in 2004.[19] Typically the precursor is iron(III) oleate, a complex consisting of a single iron(III) ion coordinated to three oleate ligands, depicted in Figure 3.1**.** When iron oleate is heated above 318°C the oleate ligands dissociate. This phase change increases the free iron concentration. If this decomposition occurs quickly, the solution will be supersaturated and nucleation will proceed as described by LaMer. [95] Solid iron oxide phases precipitate to alleviate this supersaturation. An excess of surfactant, e.g. oleic acid, is often added to control diffusion and reaction kinetics and tailor particle size. In the iron oleate synthesis, excess surfactant is generally necessary to produce particles larger than several nanometers.

At some point during the synthesis some of the iron must be reduced to iron(II) in order to produce the mixed valence magnetite. As we will see discuss later in §3.6 and Chapter 4, an excess of Fe^{2+} often results in nucleation of wüstite phases. A heat treatment or careful control of oxidation/reduction during synthesis is often necessary to optimize the nanoparticle phase.

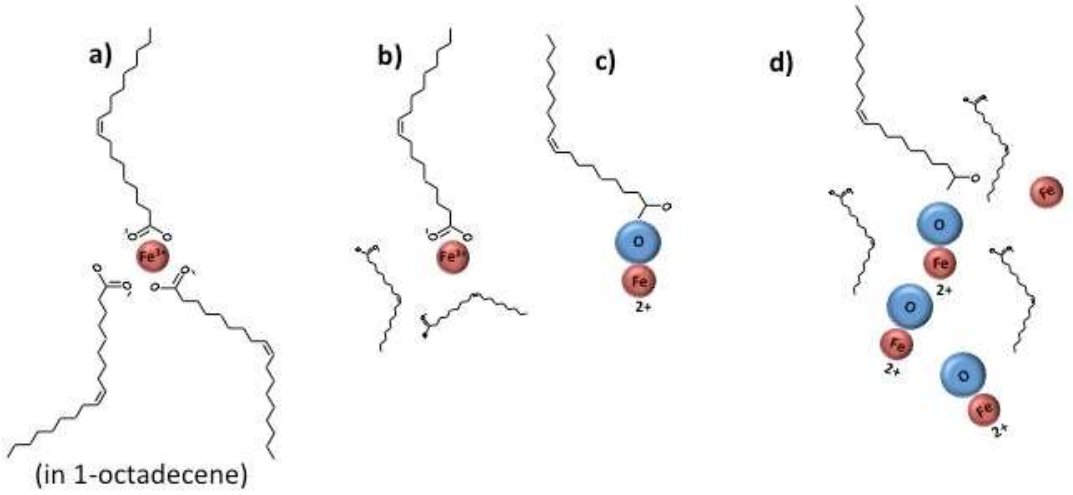

Figure 3.1. Schematic of the iron(III) oleate complex, through various stages of decomposition, interpreted from results of published simulation. [107], [108] a) The equilibrium configuration at room temperature. b) Between 150°C—230°C the two symmetrically bonded ligands dissociate. c) The low energy configuration with one oleate is to form an iron-oxide bond. d) Between 230°C—295°C the final ligand dissociates.

3.2.2.1 Synthesis from Iron (III) Oleate

Monodisperse magnetite nanoparticles are synthesized by the thermal decomposition of iron (III) oleate. A precursor solution of iron oleate (dissolved in 1-octadecene) combined with excess oleic acid is prepared in a round bottom flask. Stoichiometric ratios on the order of 1:20 Fe-Oleate:Oleic acid are routinely used, and the precursor concentration is used to adjust nanoparticle size, see Section 3.5. The precursor solution is stirred and blown with argon for around 30 minutes, while water cools a Graham condenser for argon overpressure throughout the synthesis. The condenser will cause evaporated solvent to condense and intermittently drip, sometime violently, back into solution. It is now routine to replace the condenser with a bump bulb to eliminate this inconsistency. [109] See Figure 3.2 for pictures of the reaction setup.

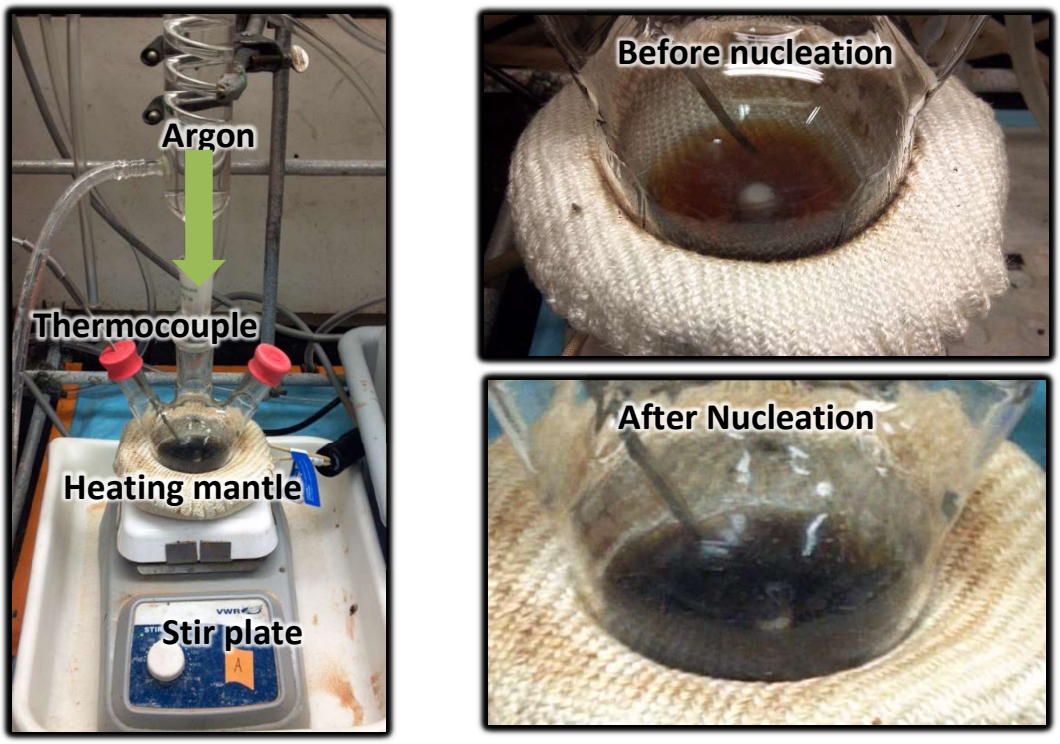

Figure 3.2. Pictures of the nanoparticle synthesis reaction.

A thermocouple probe is placed in solution and connected to a temperature controller. The solution is brought to reflux at 320°C (the boiling point of 1-octadecene is approximately 318°C) at 3°C/min, or 10°C/min in the syntheses without excess oleic acid. Reaching reflux with our setup typically takes 20-30 minutes. The initially rusty brown solution darkens once heated to around 150°C. Starting just above 200°C the solution becomes a translucent orange, tea color. The solution remains this color until nanoparticle nucleation. Several hours after reflux the solution will turn nearly black corresponding with nucleation of iron oxide particles. The clearest place to visually observe this color change is at the edge of the solution where it is thinnest. The time to nucleation varies with precursor concentrations but can be somewhat unpredictable. Control of nucleation time, and its effect on the final nanoparticle dimensions and morphology is discussed later in this

chapter. In syntheses from the as-described precursor, nucleation begins immediately above 250°C. However, by adding excess oleic acid to the precursor, nucleation was delayed up to several hours.

After nucleation, particle growth and aging occur. We typically age our particles for 24 hours or more under argon at 320°C, a length of time which is somewhat unprecedented in the literature. Although the dynamics of this growth phase are not entirely understood, the long aging time does produce larger particles and more importantly, more monodisperse particles. Post-synthesis treatments are discussed in §3.2.5, and nanoparticle phase optimization is discussed later in this Chapter, and in Chapter 4.

After synthesis is complete, particles are washed to remove excess solvent. The typical procedure for large particles (around 20 nm) is to wash with a 60/40 mixture of chloroform and methanol, sonicate, and separate with a magnet. This may act as a size selection process. Larger particles will be more strongly attracted, and small particles may be decanted off with solvent. For preparation of monodisperse particles this size selection is not necessarily a problem, but to fully characterize the growth process a representative sample is required. The particles from earlier aliquots often do not exhibit strong enough magnetism to separate with this method. Samples containing small particles (< 10-15 nm) are cleaned by dissolving particles in minimal chloroform, usually 1:1 volume ratio to particle suspension, and washing in a 4:1 1-isopropanol/ethanol solution. Particles are separated by centrifuging at 2000-3000 rpm for 3-5 minutes. Particles are usually washed 5 times, or 3 for the centrifuge method.

3.2.3 *Synthesis from Iron Pentacabonyl*[4]

Oleic acid (Sigma, 99%) is mixed with octyl ether (10 mL), injected into an argon-purged three-neck flask with a glass syringe, and heated. Upon reaching a temperature of 100°C, 0.2 mL (1.52 mmol) of iron pentacarbonyl (Sigma) is injected into the solution and the temperature is increased to reflux at 283°C. Nucleation becomes evident by a darkening of the solution over approximately 30 seconds. Particle size is controlled by varying the molar ratio of oleic acid to iron pentacarbonyl, where final size is proportional to this ratio. After nucleation, the solution is refluxed for an additional 1.5 hours. At this point iron oxide nanoparticles have formed. As-synthesized nanoparticles show poor crystallinity and presence of anti-ferromagnetic wüstite, so must be subsequently optimized. Following synthesis, nanoparticles are oxidized by the addition of Trimethylamine N-oxide (TMANO) to optimize phase and crystallinity, see §3.2.5.2

When exposed to heat, iron pentacarbonyl decomposes to form iron oxide nanoparticles. A critical difference between this and the previously described iron (III) oleate synthesis, is the additional $Fe(CO)_5$ decomposition step. The iron pentacarbonyl decomposes and releases CO, and oleic acid substitutes onto this partially decomposed intermediate to form an iron oleate complex. This iron oleate complex finally decomposes, and nanocrystals nucleate and grow. When mediated by a surfactant, i.e. oleic acid, size and morphology can be controlled. Excess oleic acid delays nucleation, and results in larger nanoparticle size, from only a few nanometers in diameter at a 1.5:1 excess oleic acid ratio, to more than 10 nm at 2.5:1. Both size and nucleation time increase with the surfactant to iron ratio. Problematically, extension of the nucleation process also results in a broader size distribution. Where uniform nanoparticle properties are required, iron oxide phase

---

[4] The iron pentacarbonyl protocol was adapted by Marcela Gonzales, and is described in detail in her thesis. [23], [18], [24]

purity and crystallite quality are of concern. Using this protocol, iron oxide particles typically form as wüstite, an antiferromagnetic phase with a low Néel temperature and undesirable magnetic properties. Nanoparticles synthesized from $Fe(CO)_5$ are always subjected to an oxidation with TMANO and annealing (*§2.1.4*). Phase purity and control are discussed in more detail in below. The following iron oxyhydroxide synthesis also produces iron (III) oleate as an intermediate without the difficult-to-reproduce injection step used in this $Fe(CO)_5$ protocol.

3.2.4 *Synthesis from Iron Oxyhydroxide*[5]

Iron oxyhydroxide (Iron(III) oxide - hydrated, Sigma-Aldrich), presumably α-FeOOH is mixed with oleic acid, with FeOOH to oleic acid molar ratios ranging from 1:15 to 1:20, and1-octadecene in a 250 mL three-neck round bottom flask. The reaction flask is purged with argon and heated to 120°C for approximately one hour. Then, the temperature is increased to 320°C at 15°C/min and held for 24 hours. The resulting nanoparticles are collected with a permanent magnet and washed with organic solvents as described previously. Crystallographic and magnetic properties may be optimized by annealing after synthesis.

The thermal decomposition of iron oxyhydroxide in the presence of excess oleic acid is similar to the iron pentacarbonyl reaction and association/dissociation with oleic acid is also an important mediating step throughout this reaction. [99] Unlike the $Fe(CO)_5$ protocol, all precursor components are stable when mixed at ambient conditions until heated. This synthesis can therefore be carried out in a single flask and the precursor can be prepared in air, eliminating the injection stem, reducing experimental error, and improves reproducibility. A more detailed explanation of this synthesis protocol appears in [37] and [33].

---

[5] The iron oxyhydroxide protocol was adapted by Hamed Arami. [33], [99]

3.2.5 *Oxidation of As-Synthesized Particles*

3.2.5.1 Oxidation by Annealing

Following synthesis, the reaction products are placed in a 250 mL three neck flask. Two necks are open to ambient air and the third was capped with a septum so the thermocouple could be held in place. The solution is brought to temperature (100°C, unless otherwise noted) at 5°C/min while stirring at 400 rpm. To monitor the phase transformation 5 mL aliquots are taken at semi-regular intervals (0, 3, 6, and 12 hours). The product is then purified by washing several times with 3:2 chloroform/methanol solution and allowed to dry in vacuum before characterization.

3.2.5.2 Trimethylamine N-oxide (TMANO)

For this oxidation procedure, the solution is first cooled to room temperature. One neck of the flask is opened while argon continued to flow, and Trimethylamine N-oxide (TMANO, 0.34 g or 4.66 mmol) is added to the solution, the flask is closed again and everything was allowed to mix at 130°C for 2 hours. During this time the color changes from black to red. Afterwards, the solution is heated to reflux for 1 hour during which time the color turns dark black, indicating the formation of magnetite. The solution is cooled to room temperature and washed with ethanol to remove excess TMANO and unattached oleic acid. While effective, because of the potential error associated with adding powder to the reaction vessel, this oxidation method more challenging to control than annealing.

3.3 THERMAL CHARACTERISTICS OF IRON (III) OLEATE

Understanding the decomposition of the iron (III) oleate complex as a function of temperature and time is critical to designing a nanoparticle synthesis that produces SPIONs of the

required size, size distribution, and phase. Iron (III) oleate is either used as the precursor directly or forms as an intermediate when iron ions associate with oleic acid in solution. [99]

Figure 3.3**a** shows Thermal Gravimetric Analysis (TGA), the derivative of TGA, and Differential Scanning Calorimetry (DSC) for the iron (III) oleate complex. TGA was performed on purified iron (III) oleate. TGA uses a very sensitive balance to measure the mass of the sample, placed in a platinum crucible and heated. Mass loss events, such as decomposition of organics and subsequent off-gassing, are observed with TGA. Three mass losses are distinctly observed, centered approximately at 193.6°C, 260.4°C, and 330.5°C. We attribute the first two mass losses to the dissociation of the oleate ligands. There are three oleate ligands coordinated to each iron atom with differing binding energies, two symmetric ligands (7.0 and 10.5 eV) and a third asymmetric ligand (39.2 eV). [108] The thermal transitions observed correspond to the detachment of the first two ligands, followed by the more tightly bound third. [19], [108] These two mass losses are very small, not accounting for the full mass of the oleate ligands. Well below the boiling point of oleic acid (360°C), this small mass loss is due to off-gassed CO_2 produced during the ketonic decarboxylation reaction. [108] The remaining mass above 400°C is approximately 18%, including the anticipated 8.5% magnetite and residual organics.

DSC was performed on the purified iron (III) oleate complex, dissolved in 1-octadecene at a concentration of 0.1698 mMol iron/g solution is also shown in Figure 3.3a. DSC measures the heat flux required to increase the temperature of the sample. We observed two endothermic events around 165°C and 240°C which correspond to sequential decomposition of the iron (III) oleate complex. These occurred just below the temperature of two key mass loss events observed with TGA and may be attributed to the same ligand dissociation. The temperature ranges we determined for these reactions, bounded by our TGA and DSC events, are 165-195°C (labeled **ii** on Figure

3.3a) for the symmetric ligands, and 240-260°C (Figure 3.3a**,** labeled **i**) for the asymmetric ones, which are consistent with simulations and previous studies. [108] For iron complexed to a single oleate ligand, Density Functional Theory (DFT) calculations predict that the formation of an iron-oxygen bond is energetically favored. [107], [108]

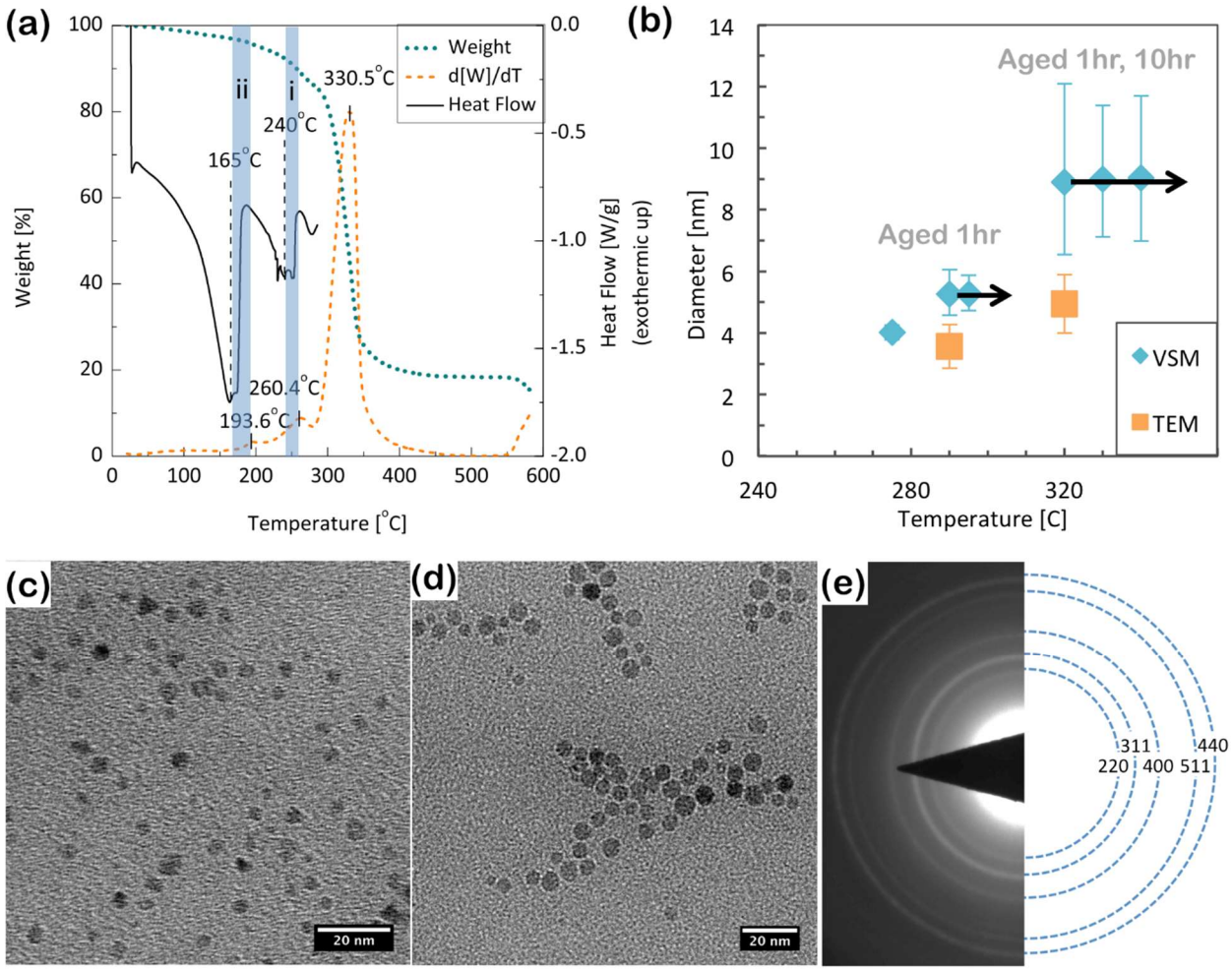

Figure 3.3. **(a)** TGA (W, Weight), derivative of TGA (dW/dT), and DSC (Heat Flow) of iron (III) oleate. **(b)** Size versus temperature for iron oxide nanoparticles synthesized by thermal decomposition of iron (III) oleate in 1-octadecene with a concentration of 0.1698 mmols of iron per gram of solution. Precursor was heated at 10°C/min until the specified temperature was reached, and a 1mL aliquot was removed from heat and quenched. Where indicated, the solution was allowed to age for a number of hours and another aliquot was taken. **(c)** and **(d)** are TEM micrographs of the particles synthesized at 290°C and 320°C, respectively. **(e)** Selected Area Diffraction Pattern from the 320°C sample, indexed as an inverse-spinel structure.

3.4 SYNTHESIS OF ULTRASMALL NANOPARTICLES

To synthesize small (<10 nm) iron oxide nanoparticles, iron oleate was heated in 1-octadecene. The solution was heated toward the set point (275°C, 290°C, or 320°C) at a rate of 10°C/minute. Based on the observed color change, from rusty brown to black, nucleation occurs at approximately 250°C. An aliquot was taken as soon as the solution reached the set temperature, and again after one hour, and 10 hours of aging for the 290°C and 320°C syntheses. Figure 3.3b displays the size as a function of this maximum growth temperature, both as determined from magnetic fitting, and as measured from TEM. For these small particles, there is significant discrepancy in the VSM and TEM size measurements, which may be attributed to loss of TEM contrast at the edge, where the particle may only be a few atoms thick. Further, a magnetic dead layer on the surface, phase impurity (see §3.6 and Chapter 4), or particle interactions cause inaccuracies in Chantrell fitting [47] results.

Table 3.2. Sizes and size distributions of small (< 10 nm) particles produced by thermolysis of iron (III) oleate in 1-octadecene, measured in TEM and by fitting the VSM measurements.

T(°C)	D (VSM)	σ (VSM)	D (TEM)	D_{ave} TEM	σ	n
275	4.01	0.24	-	-	-	-
290	5.26	0.75	3.50	3.57	0.71	313
320	8.89	-	4.92	4.95	0.95	1206

Growth proceeds quickly following nucleation at 250°C and there is little difference in size or distribution between particles at nucleation, or after aging at 320°C for 1 or 10 hours. Under these conditions, the excess iron in this supersaturated solution precipitates rapidly followed by a short growth period without significant effect due to aging. TEM micrographs (Figure 3.3c and d)

show single crystalline particles as indicated by uniform contrast within each particle. The smallest (< 5nm) particles are irregular crystallites and larger particles appear roughly spherical. Figure 3.3**e** shows an example Selected Area Electron Diffraction (SAED) pattern from the 320°C sample, with the characteristic inverse-spinel peaks. Particles up to 10 nm were synthesized using 1-octadecene as solvent, with no additional surfactant. It was previously shown that higher synthesis temperatures, in higher boiling solvents, produce larger particles. [19] To produce larger particles in 1-octadecene, it was necessary to dilute the precursor solution with excess surfactant, *e.g.* oleic acid.

3.5 Tuning Nanoparticle Size by Addition of Surfactant

By adding excess oleic acid, particle size can be increased and tuned from approximately 10 to 25 nm. Excess oleic acid alters the reaction beyond just reducing the concentration of iron in solution. Oleic acid can associate with iron in solution, even above the decomposition temperature of the iron (III) oleate complex, competing with the formation of iron-oxide bonds. Diluting with a non-coordinating solvent, *i.e.* excess 1-octadecene, also increases the size but broadens the size distribution. [28], [37] This is due to reducing the iron supersaturation prior to nucleation, and is qualitatively explained by LaMer supersaturation theory, see Appendix A. [95] To study the kinetics of nanoparticle synthesis, aliquots were taken throughout synthesis. Figure 3.4 shows a histogram of nanoparticle sizes measured by TEM from 0 to 24 hours from nucleation. The lengthy reaction time serves to focus the size distribution and optimize the nanoparticle phase.

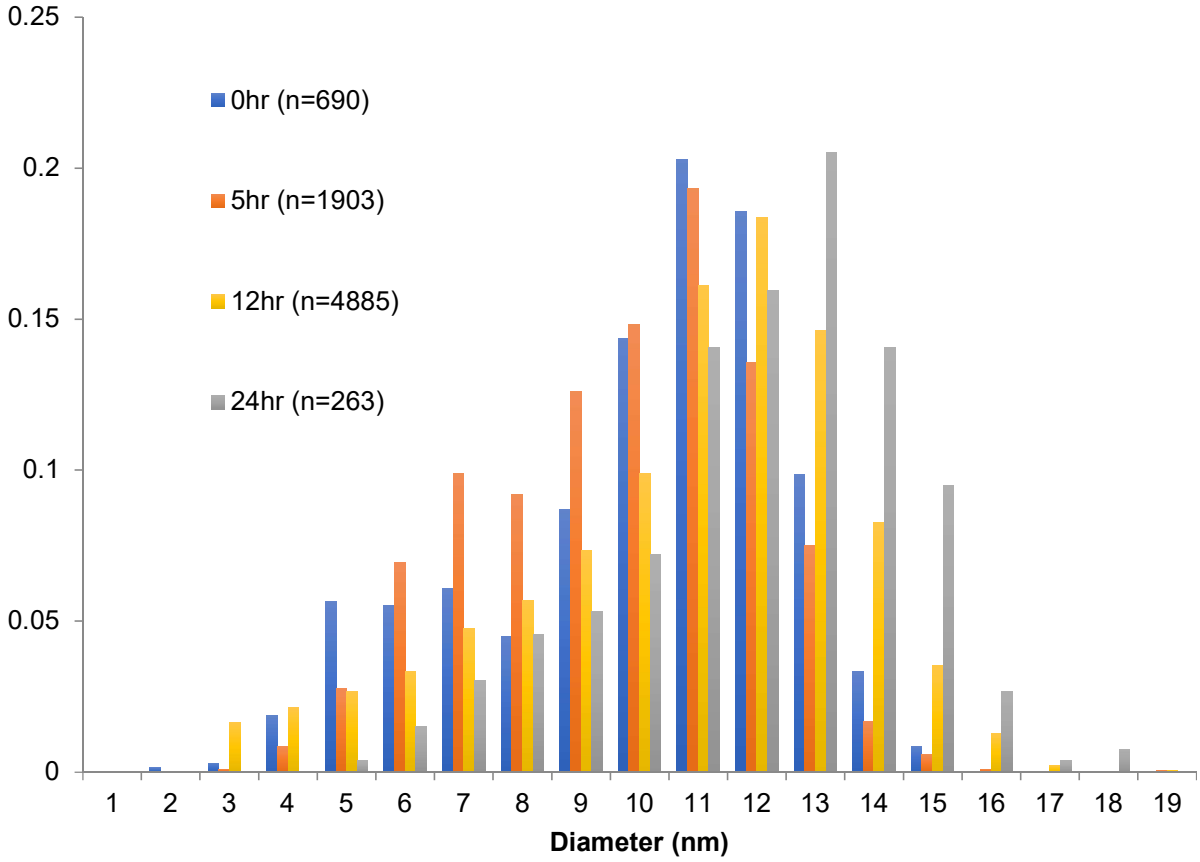

Figure 3.4. TEM size histogram from aliquots taken during a nanoparticle synthesis. A molar ratio of iron(III) oleate to excess oleic acid of 1:19 was used, and in total there are 0.5 mMol of iron in this scale of synthesis.

Magnetic size was also measured by fitting VSM measurements and are compared for this synthesis in Figure 3.5. For superparamagnetic particles, sizes typically agree between the two techniques, however, as we will show later if the distribution becomes large or if particles are mixed-phase or have weak magnetic response, the assumptions made to fit the VSM data will no longer be valid.

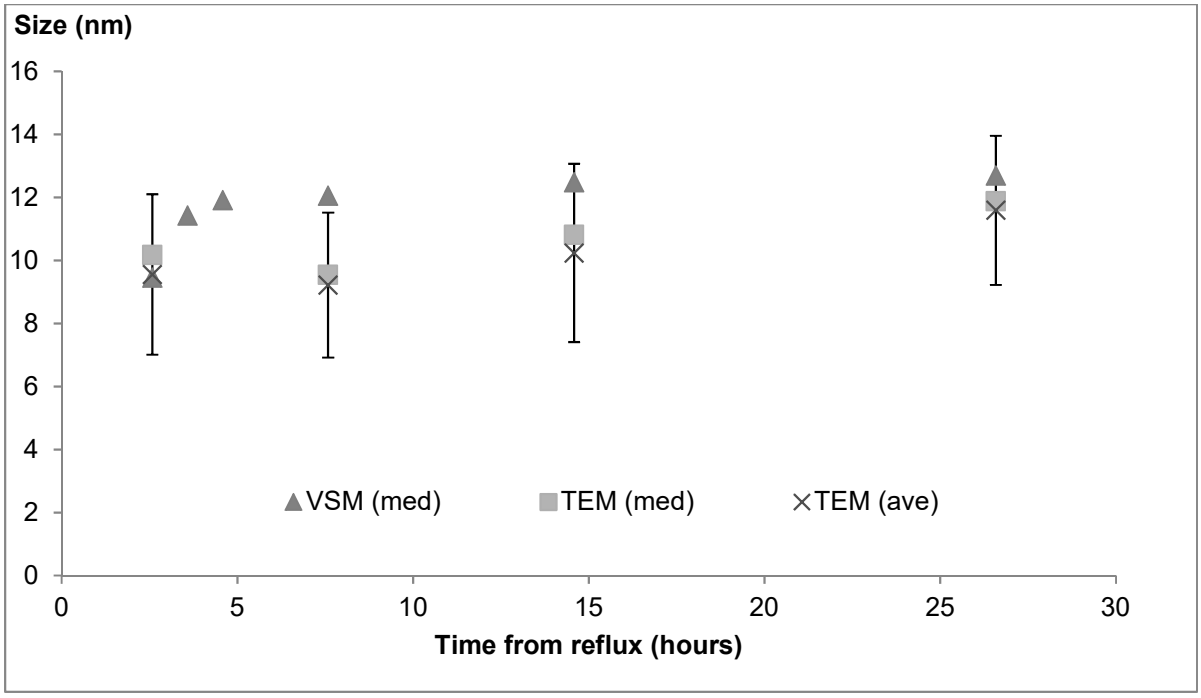

Figure 3.5. Comparison of TEM and VSM size measurements.

Similar syntheses were repeated with different ratios of excess surfactant, and aliquots were taken throughout the reaction to monitor growth. The growth profiles for several excess oleic acid: iron ratios are shown in Figure 3.6. In all cases, 0.5 mmol of iron (III) oleate in 2.95g of 1-octadecene are reacted with the specified ratio of excess oleic acid. One mL aliquots were taken throughout the reaction, quenched to arrest growth, and particle size is determined from magnetic properties. Excess oleic acid delays nucleation from around 1.5 hours for a 1:5 ratio up to approximately 2.5 hours for a 1:19 ratio. Prior to nucleation, no nanoparticles are observed in solution by any of our characterization methods. In this protocol, the magnetic size increases over the course of several hours following nucleation. By 12 hours after nucleation, the particles have nearly reached their maximal magnetic size. Particles are typically monodisperse, although either adding oleic acid or reducing iron concentration increases the size and broadens the size distribution.

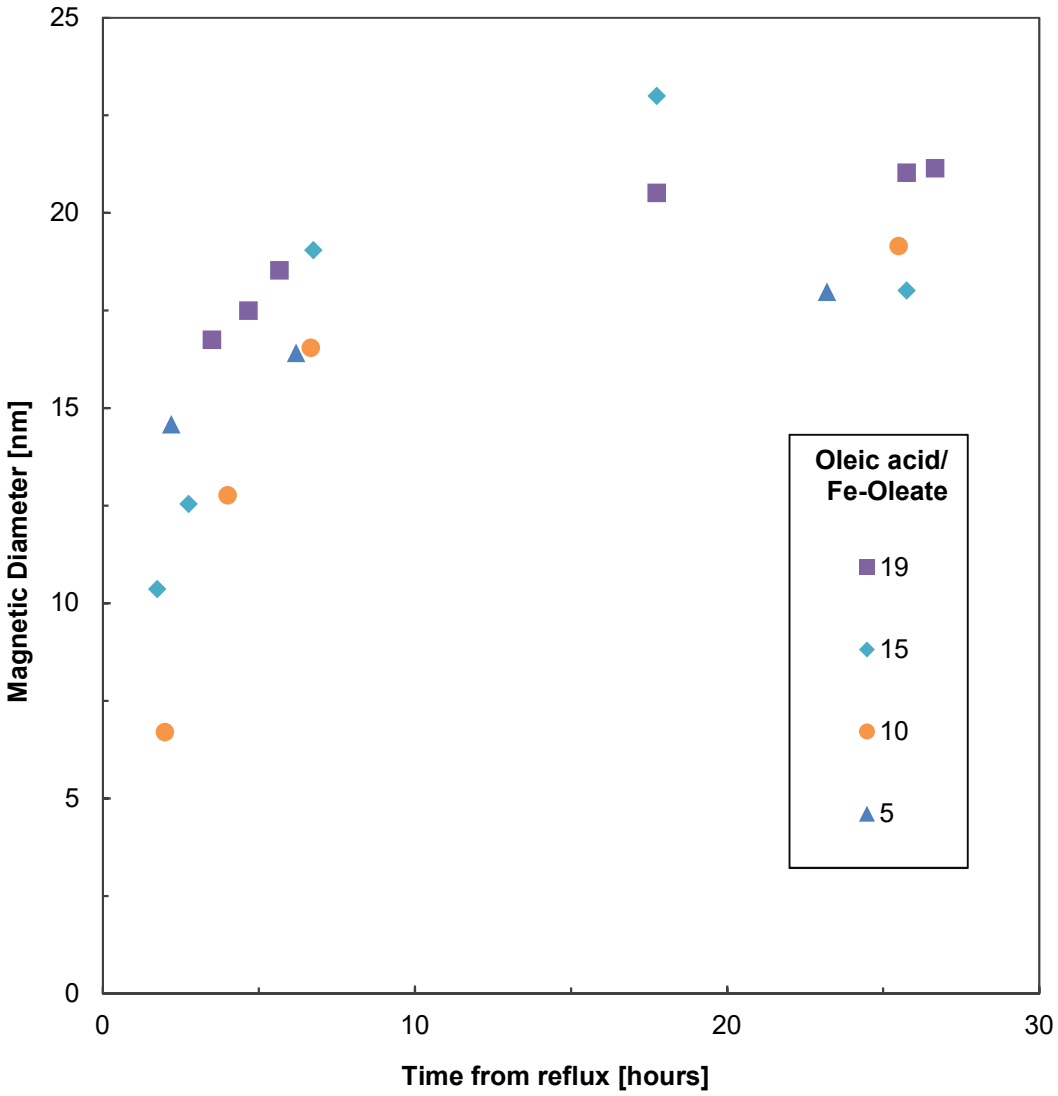

Figure 3.6. Superparamagnetic iron oxide nanoparticles produced by thermal decomposition of iron (III) oleate in the presence of excess oleic acid. Size can be controlled with a precursor concentration, excess oleic acid, and aging time. All sizes are median diameter (D_M) from estimated from VSM measurements.

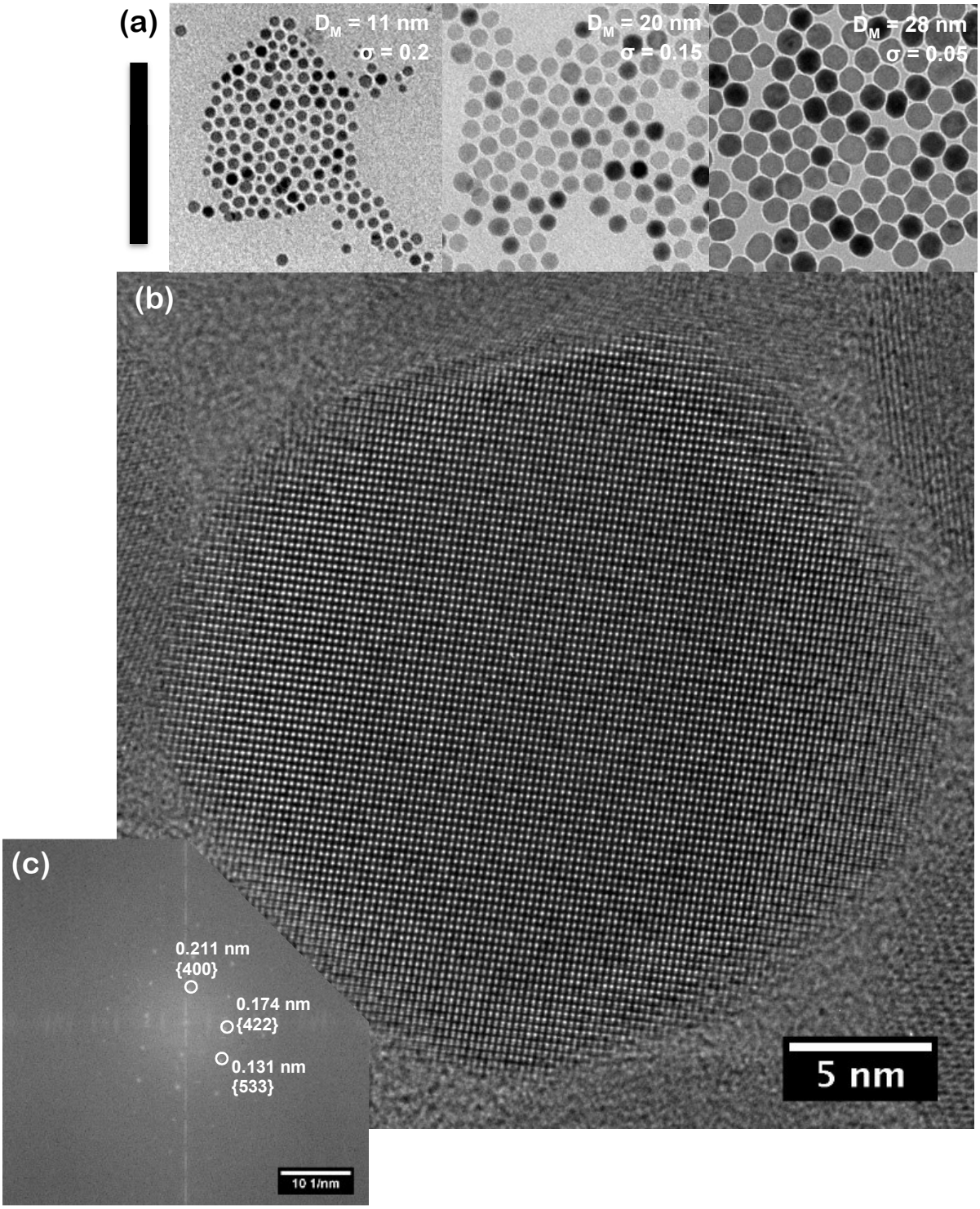

Figure 3.7. TEM images of particles of various sizes (**a**, scale bar 100 nm). All sizes are median diameter (D_M) and error bars represent the first standard deviation of the log-normal size distribution (σ), determined by fitting VSM measurements. High resolution TEM of nanoparticles synthesized from FeOOH **(b)** (5 nm scale) and FFT of this image **(c)**.

Figure 3.7a shows some example TEM images of nanoparticles produced by decomposition of iron oleate. HRTEM confirms that nanoparticles are single crystalline (Figure 3.7b). They are approximately spherical, and facetted. This is to be expected for single crystal nanoparticles with a cubic unit cell. This morphology is a compromise between minimizing surface energy while remaining single crystalline. No defects or twinning are apparent from the micrographs. The particle edges are sharp and well-defined, and no amorphous regions or grain boundaries are observed within the particles. This is consistent with growth from small clusters, and by the surfactant-mediated adsorption of growth species. These observations appear to be true across all size ranges, however, faceting does become more apparent at larger sizes. This is qualitatively explained with an argument similar to the Wulff construction, [110], [111] although these nanoparticles are not formed at equilibrium. High surface energy facets grow fastest, eventually disappearing into the crystal's corners and edges. After a long enough growth time, a nanocrystal will be terminated by its low-energy facets.

3.6 Phase Characterization and Control

Iron oxide phase is a major factor influencing magnetic properties of nanocrystals, and therefore affects performance of SPION tracers for MPI, MRI, and other applications. Magnetic properties of phase-pure magnetite nanoparticles are compared to mixed-phase nanoparticles of similar size, see Figure 2.2. In literature, the performance of these nanoparticles has also been compared to Resovist®, commercially available nanoparticles synthesized by co-precipitation. [37] The FWHM of the differential susceptibility (dm/dH) measured by MPS is an indication of potential MPI spatial resolution, [31], [89] and here is narrowest for phase-pure magnetite nanoparticles. VSM measurements also show decreased saturation field and increased susceptibility for the phase-pure magnetite compared to mixed-phase. Predictably, the mixed phase

nanoparticles performed the worst both in terms of FWHM of MPS and the VSM despite being monodisperse. Phase impurities can have just as important an effect on magnetic properties as SPION size distribution.

Phase control is a critical consideration in iron oxide nanoparticle synthesis. The four stable or metastable iron oxide phases are wüstite (FeO_x), magnetite (Fe_3O_4), maghemite (γ-Fe_2O_3), and hematite (α-Fe_2O_3). Wüstite and hematite are antiferromagnetic and unsuitable for most applications. Fortunately, wüstite can be readily transformed to superparamagnetic magnetite after synthesis by annealing in air (Figure 3.8c), or introducing an oxidizing agent, such as TMNAO.

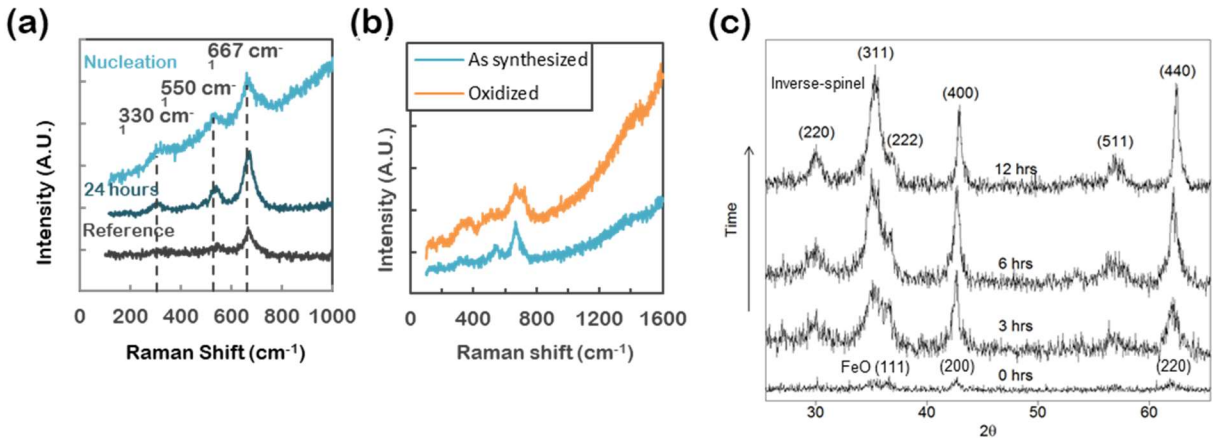

Figure 3.8. **(a)** Raman Spectroscopy of iron oxide nanoparticles synthesized from iron(III) oleate and characterized at nucleation and after 24 hours of aging. **(b)** Synthesized from FeOOH, and oxidized to maghemite **(c)** XRD, θ - 2θ scans, of iron oxide nanoparticles synthesized from iron oleate. As synthesized particles showed low intensity peaks characteristic of wüstite. Particles were annealed at 100°C for various times to optimize phase and crystallinity. The peaks observed on annealing can be readily indexed as magnetite.

Previous studies have shown the importance of gas composition on the resulting iron oxide phase, in particular the effect of CO on reduction of Fe_3O_4 to FeO.[112], [113] Presence of oxygen

in the system transforms CO to CO_2 and prevents reduction of Fe_3O_4 to FeO by CO. The CO and CO_2 are most likely byproducts of partial combustion of organics.[112] For the decomposition of iron pentacarbonyl, CO gas is produced directly by the precipitation reaction, so gas composition has a direct effect on reaction rate and equilibrium.[114] Reactions in this experiment were performed under argon and phase was characterized and optimized after synthesis. Figure 3.8c shows an example of phase optimization by post-reaction annealing. These nanoparticles were synthesized by thermal decomposition of FeOOH. In this example, the as-synthesized particles show poor crystallinity in X-ray diffraction scans; peaks are hardly visible above the noise. The sample may contain nanoparticles of varying oxygen content (multiple phases) or may have poor crystallinity. After annealing for three hours magnetite was detectable. Crystallinity improved with additional annealing, as indicated by the formation of more well-defined magnetite peaks.

Raman Spectroscopy is an inelastic scattering technique that probes vibrational modes in the sample and is sensitive to both chemistry and bonding. Raman spectroscopy is capable of distinguishing between different iron oxide compounds based on characteristic vibrational modes.[6], [45] Raman spectra (Renishaw inVia) were obtained from 1 mg of dried nanoparticle powder on aluminum using a 514nm laser, reduced from 15 mW to approximately 0.15 mW using filters, and six, 60 second scans were summed together. The peaks at 670 cm^{-1}, 540 cm^{-1}, and 310 cm^{-1}, are considered diagnostic of magnetite, consistent with literature. [6] The Raman spectra of nanoparticle synthesized from iron (III) oleate (Figure 3.8a**)** are characteristic of magnetite, with no indication of the presence of any other phases, even shortly after nucleation. Figure 3.8b shows Raman spectra from nanoparticles synthesized from FeOOH. The as-synthesized particles are magnetite: after oxidation at 100°C for 12 hours (see *§2.1.5)* the 670 cm^{-1} peak extends beyond

700 cm^{-1}. Additionally, a broad second harmonic appears in the 1300-1400 cm^{-1} range. Both of these are considered diagnostic of maghemite, and consistent with literature. [6], [45], [115]

Hematite and many other iron oxide and oxyhydroxide phases are also readily identified from Raman spectra. [6], [115] However, thermal and laser induced transformation of many of these phases is a concern. [5], [6] Wüstite in particular is metastable at ambient conditions and is challenging to characterize using Raman Spectroscopy without transforming to magnetite or hematite. A distinct wüstite peak has been reported at approximately 595 cm^{-1} when observed at very low laser powers. [6] Many purported wüstite Raman spectra in literature appear to have been transformed to magnetite. [45], [115]

We have observed issues with phase purity as the reaction volume of the nanoparticle synthesis has been increased toward 1 g of nanoparticle product, resulting in the synthesis of wüstite (FeO) or mixed phase particles. This was not a significant issue at smaller scales. This could be due to increased reaction volume, decreased surface/volume ratio for the solution, and altered glassware setup leading to decreased gas volume, and insufficient availability of oxygen for oxidation. Turbulence due to altered stirring geometry may also have an effect.

Phase composition may be affected by the decomposition of the iron(III) oleate precursor and subsequent oxidation. After removal of the first two, symmetric ligands, the lowest energy configuration is for iron to bind with an oxygen in the oleate's carboxylate group. This is where excess oleic acid can alter kinetics by associating and dissociating with iron, competing for with formation of iron oxide. At this point the oleic acid may reduce the iron from 3^+ to 2^+. These Fe^{2+} ions and FeO monomers form nuclei in the supersaturated solution. Initially particles are probably entirely FeO and are partially oxidized to form magnetite by dissolved oxygen in solution or other solution components. If there is insufficient oxidizing agents, or if growth proceeds faster than

oxidation, wüstite particles may persist. In my previous experiments, only magnetite was detected even immediately after nucleation and in the smallest particles. However, at larger scales wüstite particles have been produced.

Wüstite is anti-ferromagnetic with a Néel temperature of 198K, so at room temperature it is effectively paramagnetic and this is unacceptable for most applications. To recover these nanoparticles, we have explored annealing to transform to magnetite and optimize magnetic ordering. Beginning with as-synthesized wüstite-containing nanoparticles,[6] the solution was annealed under air at elevated temperature. We used temperatures of 100ºC, 150ºC, and 200ºC for times ranging from 12-24 hours. Following is my TEM analyses of the 100ºC, 16 hour anneal, one of the more successful protocols. Figure 3.9 depicts the radially integrated selected area electron diffraction from this sample before and after annealing. The as synthesized particles match well with predicted pattern for wüstite. A small quantity of magnetite is present, as indicated by the 220 peak at ~3.2 nm^{-1}. After annealing, there is a clear transformation, as indicated by the presence of magnetite peaks. There is still some indication of wüstite, indicating incomplete oxidation.

[6] These nanoparticles were synthesized by Hamed Arami.[33]

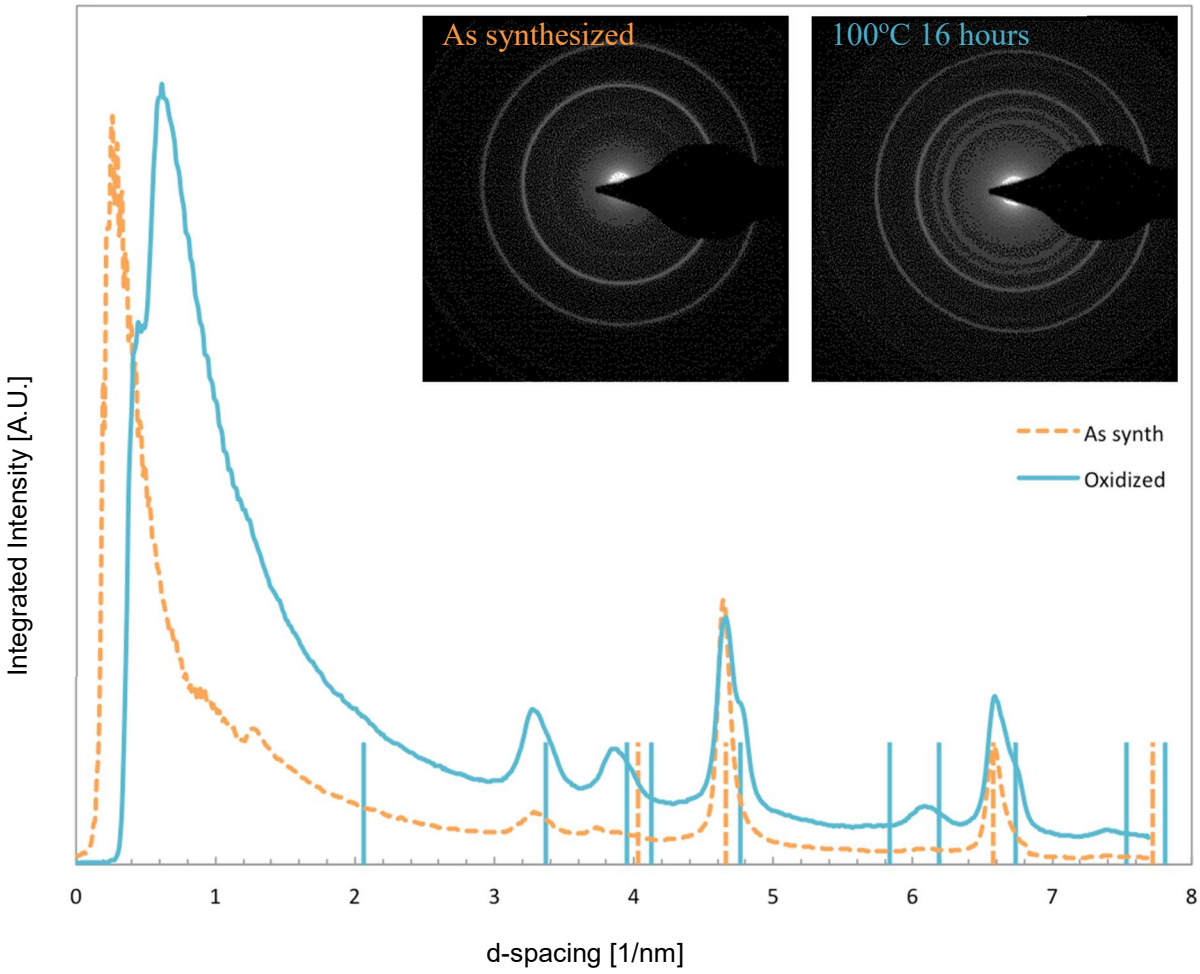

Figure 3.9. Selected Area Electron Diffraction performed at 200 kV, from the iron oxide nanoparticles, as synthesized, and after a 16 hour, 100°C oxidation. Vertical lines indicated predicted peaks for magnetite (blue) and wüstite (orange dashed).

The TEM micrographs in Figure 3.10 and Figure 3.11 depict these particles before and after annealing. The size of the particles does not significantly change, 27.4 +/- 2.3 (n = 15,545) before, and 27.7 +/- 1.4 (n = 2420) after. The phase transformation occurs without disrupting particle morphology, and without particles agglomerating.

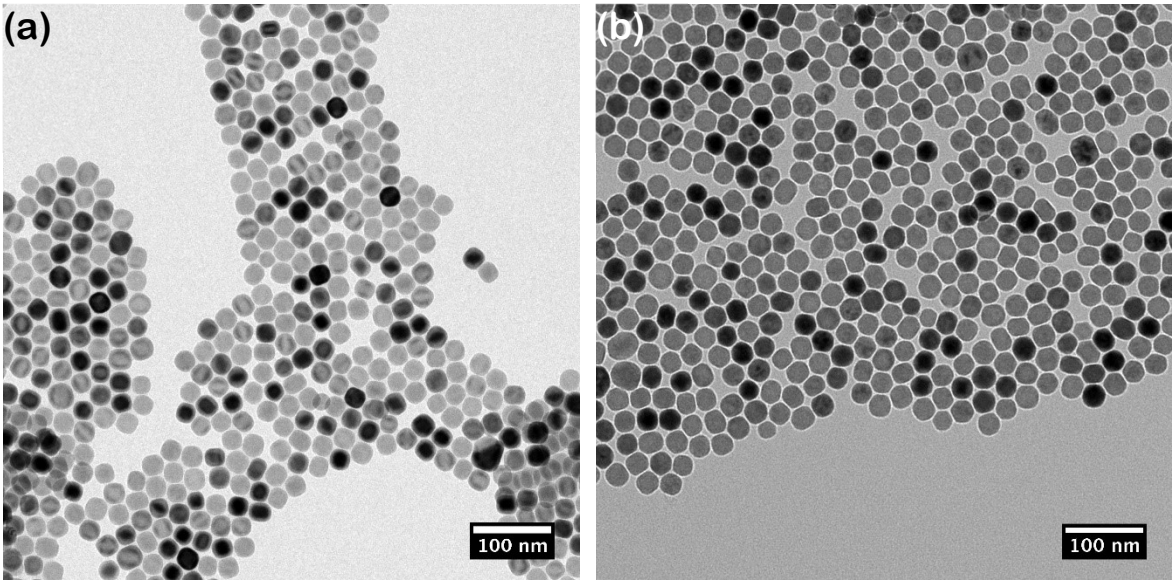

Figure 3.10. TEM images of nanoparticles as-synthesized **(a)**, and after oxidation **(b)**.

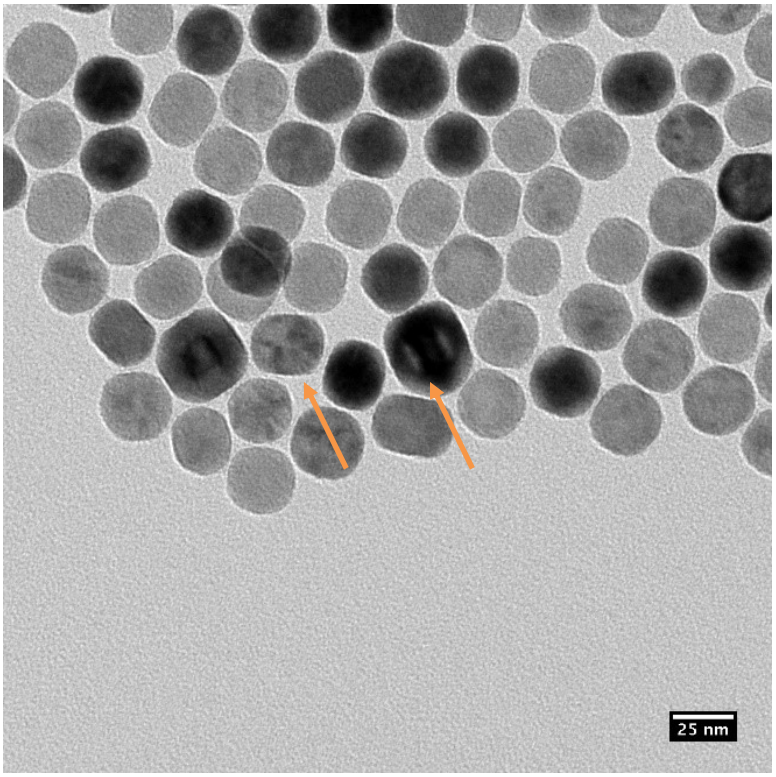

Figure 3.11. Higher magnification TEM image, notice the contrast variations within individual particles, probably caused by strain due to secondary wüstite phase.

Contrast variations within individual particles are visible in Figure 3.11. This is most likely diffraction contrast caused by strains within the nanoparticles interfering with the lattice spacing, due to the presence of wüstite in nanoparticles. They do appear to be single crystalline. Magnetite and wüstite can coexist and can be considered as a different occupation of iron in interstitial sites in the FCC oxygen lattice. However, there will be a lattice mismatch of 2-3% (a_M = 8.397 Å, a_W = 2·4.332 Å = 8.664 Å), which can account for these strains. These particles may be wüstite cores with magnetite shells or some other arrangement of iron valence and site occupation. Future study is necessary to say more about the structure of these mixed phase particles, which is discussed in Chapter 4.

Even after oxidation some strain-induced contrast is visible. Particles possibly oxidize from the outside in and if enough time is not given the wüstite core may not fully transform to magnetite. The procedure needs to be optimized for each batch size and recipe to ensure a complete transformation to magnetite and optimized magnetic ordering and properties. It may be reasonable to include an annealing step after synthesis as a precautionary measure, but directly monitoring the phase composition and evolution is essential for producing optimized nanoparticles.

EELS is also used to compare as-synthesized SPIONs with nanoparticles annealed at 100°C under atmosphere for 12 hours to form maghemite. These samples were also characterized using Raman Spectroscopy in Figure 3.8b. The iron L_3/L_2 ratio, here measured from second derivative of the EELS (Figure 3.12), is proportional to valence, with a larger ratio indicating a higher valence. These iron L edges correspond to transitions to the partially filled 3d shell, from the 2p shell, with spins of -½ and + ½, respectively. Population of the valence shell alters the probability for these transitions, with EELS fine structure depending on local bonding and coordination. The iron L_3/L_2 ratio is measured to be 4.54 for the as-synthesized nanoparticles and 5.63 for the

annealed sample. Comparing to references, we estimate the valence of these samples is approximately +2.4 for the as-synthesized sample (+2.67 theoretical for magnetite), and +2.9 for the annealed sample (+3 theoretical for maghemite). [72], [116] These references agree with each other within ~10%, although Cavé, et al. [67] used a different method for determining peak intensity. The comparably small L_3/L_2 ratio for the as-synthesized sample may indicate presence of wüstite, which is not readily detectable with Raman Spectroscopy, while the annealed sample appears to be nearly fully transformed to maghemite.

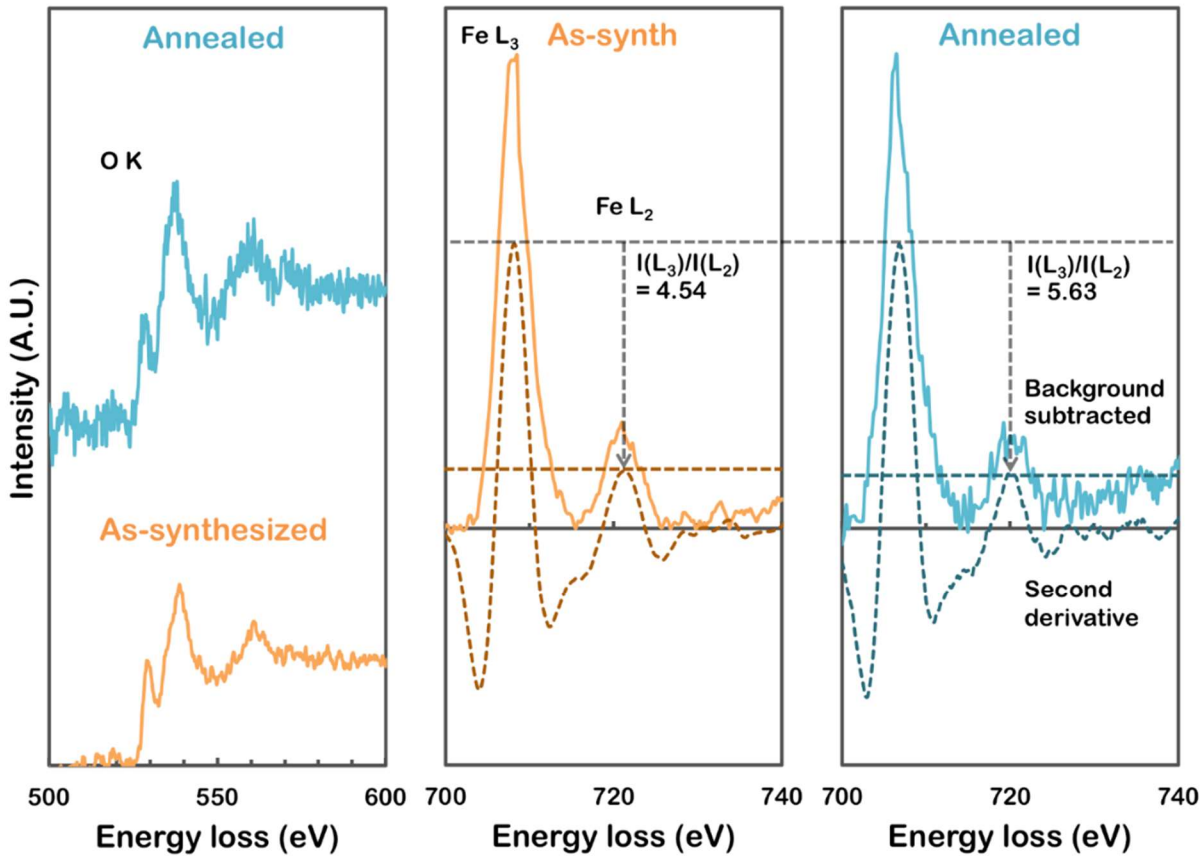

Figure 3.12. Electron energy loss spectra from iron oxide nanoparticles synthesized from FeOOH before and after annealing at 100°C for 12 hours, showing the oxygen K-edge (onset ~532 eV) and iron-L edge (onset ~708 eV). The intensity ratio of iron L_3 to L_2 edges is proportional to oxidation state, increasing as particles transform from magnetite to maghemite.

As described previously, under certain circumstances wüstite (FeO) phase may be present in as-synthesized nanoparticles. Particularly, phase impurities are often detected in nanoparticles larger than 22 nm synthesized with FeOOH or iron oleate protocols, and for smaller nanoparticles synthesized via the $Fe(CO)_5$ protocol. Wüstite is difficult to detect with Raman spectroscopy, as wüstite rapidly transforms to magnetite under laser irradiation. X-ray or electron diffraction experiments can readily identify the wüstite phase. When applied together, diffraction and Raman spectroscopy can be used to determine the phase of any unknown iron oxide. Additionally, iron valence can be calculated using EELS to confirm the diffraction and Raman results.

3.7 Summary of SPION Synthesis

Iron oxide nanoparticles have been synthesized by the thermal decomposition of three different precursors, all sharing iron (III) oleate as an important reaction intermediate. By adjusting thermal parameters as well as precursor concentration and composition we have demonstrated size control between approximately 2 nm and 30 nm. In all three procedures, the iron forms complexes with oleic acid to form iron (III) oleate. Due to the importance of the iron (III) oleate complex in all syntheses, it is the focus of the thermal characterizations. Breakdown of iron (III) oleate occurs above around 250°C. For iron (III) oleate in 1-octadecene, increasing the synthesis temperature beyond 250°C with a constant ramp rate results in increasingly larger particles, up to around 10 nm. If this iron (III) oleate precursor is diluted with excess oleic acid, nucleation is delayed and growth is slowed. The excess oleic acid acts as a surfactant, coating particles and competing with iron and oxygen species for attachment. Particles grown in the presence of excess surfactant and given sufficient aging times are single crystalline and monodisperse. By increasing the oleic acid to iron oleate ratio from 5:1 up to 20:1 or more, particle size can be tuned up to approximately 25 nm. A similar relationship between excess surfactant ratio and particle size has been demonstrated

in the $Fe(CO)_5$ and FeOOH thermal decompositions. The $Fe(CO)_5$ protocol is particularly suited for smaller (<10 nm) nanoparticles, while the FeOOH protocol can produce monodisperse nanoparticles in the 10-25 nm range. By increasing the surfactant (oleic acid) concentration, particle size increases, however above a certain ratio (around 20:1 molar ratio for iron (III) oleate, 2.5:1 for $Fe(CO)_5$, and 16.5:1 for FeOOH) the distribution broadens. Monodisperse particles are required for most applications, so this effectively places an upper limit of around 30 nm on the synthetic approaches described. Care must be taken to ensure nanoparticles are not only the appropriate size, but also that phase and crystallinity are optimized for their desired properties. In our experience, nanoparticles synthesized with the $Fe(CO)_5$ protocol and larger nanoparticles (>22nm) synthesized with FeOOH and iron oleate methods must be oxidized following synthesis to eliminate oxygen deficiencies and form single crystalline and pure magnetite or maghemite. Phase can be manipulated during synthesis by considering oxygen availability, or post synthesis by introducing an annealing or oxidation step.

Following this work, I continue in the next chapter with additional analysis of iron oxide nanoparticles phase in more detail and relate these characterizations to the nanoparticle properties.

Chapter 4. PHYSICAL AND CHEMICAL STRUCTURE OF SUPERPARAMAGNETIC IRON OXIDE NANOPARTICLES

In this chapter, the role of the nanoscale chemical and magnetic structure on relaxation dynamics of iron oxide nanoparticles in the context of Magnetic Particle Imaging (MPI) is investigated using Mössbauer Spectroscopy (MS) and Electron Energy Loss Spectroscopy (EELS).[7] Two samples of 27 nm monodisperse iron oxide nanoparticles are compared, with and without an additional oxidation optimization step, and with corresponding differences in structure and properties. Iron oxide nanoparticles synthesized in the presence of sufficient oxygen form single crystalline, inverse-spinel magnetite (Fe_3O_4), and display magnetic properties suitable for MPI. A secondary wüstite (FeO) phase is observed in the diffraction pattern of unoptimized nanoparticles, which is antiferromagnetic and therefore unsuitable for MPI. Mössbauer spectra confirm the composition of the optimized nanoparticles to be ca. 70% magnetite, with the remaining 30% oxidized to maghemite; in contrast, the as-synthesized particles (without the oxidation step) contained about 40% wüstite and 60% magnetite. We use Scanning Transmission Electron Microscopy (STEM) with Electron Energy Loss Spectroscopy (EELS) to probe iron 2*p*-3*d* electronic transitions and correlate their intensities with the oxidation state, with sub-nanometer spatial resolution. The optimally oxidized nanoparticles are uniform in crystallography and phase, while the mixed phase nanoparticles are core-shell wüstite/magnetite. Further confirming the core-shell structure of the mixed phase nanoparticles, we observe considerable spin canting in the in-field Mössbauer spectrum, likely caused by interface coupling.

---

[7] Portions of the following chapter are published as "Nanoscale Physical and Chemical Structure of Iron Oxide Nanoparticles for Magnetic Particle Imaging" by Ryan Hufschmid, Joachim Landers, Carolyn Shasha, Soma Salamon, Heiko Wende, and Kannan M. Krishnan in *physica status solidi (a)* 2018.

4.1 Physiochemical Structure of Iron Oxide Nanoparticles for Biomedical Applications

Iron oxide nanoparticles are ideal for many biomedical applications that rely on their superparamagnetic properties. A prime example is Magnetic Particle Imaging (MPI), an emerging medical imaging platform currently in the preclinical stage that enables direct spatial mapping of SPIONs *in vivo*. In theory, MPI will provide significantly greater sensitivity and image contrast than other clinically available tomographic modalities, including magnetic resonance imaging (MRI), positron emission tomography (PET), and computed tomography (CT) due to its shorter image acquisition time, and quantitative, linear contrast at a relatively low cost.[1], [26], [83], [117]–[119], [22], [120]–[122] MPI is also enabling the development of 'theranostic' tools: platforms that combine diagnostic imaging with therapeutic functions. such as targeted drug and gene delivery[123]–[130] and hyperthermia cancer treatment.[131]–[134] Finally, their ability to be guided and detected by an external magnetic field has allowed these therapeutic techniques to be combined with diagnostic imaging using MPI.[22], [135]–[140] The superparamagnetic properties that prevent their agglomeration *in vivo,* plus biocompatibility and chemical stability make SPIONs ideal for these applications.

The physical properties of the SPIONs on the nanoscale contribute to performance in MPI, which employs a combination of magnetic field gradients and alternating magnetic fields to generate an image from the dynamic response of superparamagnetic nanoparticles. [83], [118], [121] For the best MPI performance, i.e. sensitivity and resolution in imaging, optimization of size, size distribution, and magnetic response of SPIONs to the applied alternating field amplitude and frequency is critical. [26], [46], [89] Of the three phases of iron oxide – magnetite (Fe_3O_4), maghemite (γ-Fe_2O_3), and wüstite (FeO) — typically produced during solvo-thermal synthesis,

magnetite is optimal, given its ferrimagnetism and high saturation magnetization. Ferro- and ferrimagnetic materials will exhibit superparamagnetic behavior when their size is reduced below a certain critical diameter, on a given measurement timescale, usualy 100 seconds. [141] Often overlooked, the oxidation state of the iron oxide nanoparticles has a significant impact on their magnetic properties. During the nanoparticle synthesis process, a controlled heat treatment (annealing) of nanoparticles is required to ensure optimal oxidation to magnetite. If under-oxidized, wüstite, which is antiferromagnetic and not suitable for MPI purposes, will form. Mixed-phase, wüstite-magnetite nanocubes have been observed. [103], [113] When annealed in air magnetite will gradually undergo an oxidative transformation to maghemite. [3]

Magnetite (Fe_3O_4) has an inverse spinel structure and contains both ferric and ferrous ions. Above the Verwey transition temperature (~120 K), tetrahedral (A) sites are populated by Fe^{3+} ions, and octahedral (B) sites contain both Fe^{3+} and Fe^{2+} ions, where the electrons are delocalized. Below the Verwey transition, the electrons become localized and alternate B sites are occupied by either Fe^{3+} or Fe^{2+} ions, resulting in a drop in electrical conductivity. The crystallographic structure of maghemite (γ-Fe_2O_3) is similar to magnetite but contains only ferric ions on both the A and B sites. Maghemite may also be considered as Fe^{2+} deficient magnetite, with vacancies on some of the B sites. The ratio of ferrous to ferric ions in an iron oxide sample determines its oxidation state and is a major indication of iron oxide phase. Wüstite (FeO) is a complex nonstoichiometric oxide that can exist in a variety of structure types. Wüstite can contain ferrous ions in B sites, ferric irons in both A and B sites, Fe^{2+} vacancies, and varying degrees of defect clusters, and undergoes a structural distortion at the Néel temperature (~ 200K). [3]

To determine the oxidation state, phase, and morphology at the nanoscale, complementary crystallographic and electronic structure characterization methods are necessary. Here, we

investigate two nanoparticle samples: the first consists of homogeneous magnetite nanoparticles, ~27 nm in diameter, designed and synthesized with an *in situ* anneal during synthesis for optimal oxidation and 25 kHz MPI performance; the second, synthesized without *in situ* annealing, is of similar size but is under-oxidized and contains wüstite and magnetite mixed-phase nanoparticles.

Characterizing the oxidation state of SPIONs including the morphology or spatial distribution of phases within individual nanoparticles is important in ensuring optimal magnetic properties for their use in MPI. Return to Figure 2.2 for an example of the magnetic performance of optimized and mixed phase iron oxide nanoparticles. The two samples are both approximately 27 nm in diameter and nearly indistinguishable via TEM as shown in Figure 4.1 Wüstite is observed in the diffraction pattern of the unoptimized sample in addition to the inverse-spinel peaks, indicating a mixed phase particle.

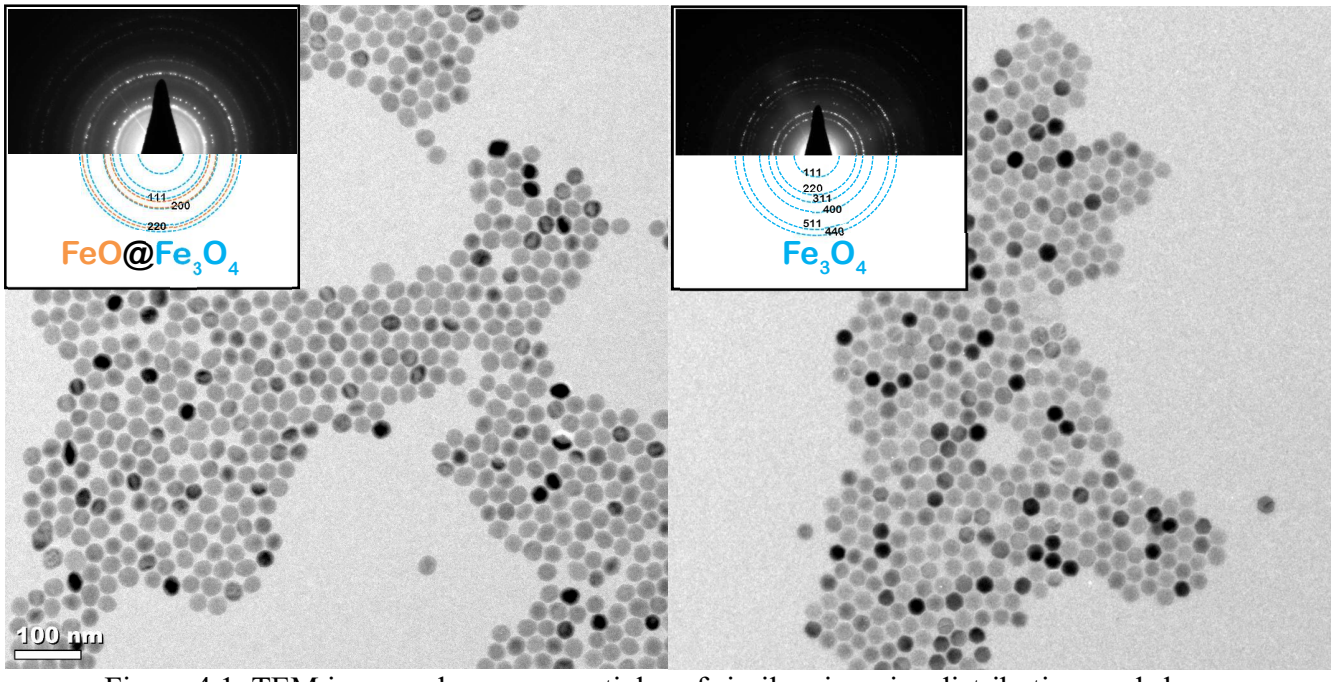

Figure 4.1. TEM images show nanoparticles of similar size, size distribution, and shape. Presence of wüstite is observed in the inset FeO@ Fe_3O_4 diffraction pattern, however this phase difference is not evident in the bright field TEM images. The optimized Fe_3O_4 nanoparticles show only inverse-spinel diffraction peaks.

There is little indication of the arrangement of these two phases from the image, i.e. whether phase pure nanoparticles of each are present separately, or if multiple phases occur within individual nanoparticles. Thus, to investigate the nanoscale electronic structure and phase homogeneity of *individual* nanoparticles, I employ scanning transmission electron microscopy (STEM) with electron energy-loss spectroscopy (EELS). Using a highly focused sub-nm diameter probe, STEM can measure the electronic structure of the unoccupied levels of individual nanoparticles at the highest spatial resolution. Measured with EELS, the ratio of intensities of L_3 and L_2 edges is proportional to transition metal valence (see §2.2.2) [142], [116], [143] and is applied here to measure iron valence in SPIONs.

4.2 Characterizing Individual Nanoparticles with STEM/EELS

To understand the structure and chemical origin of these observations at high spatial resolution, we perform STEM using a high angle annular dark-field (HAADF) detector. Here, large-angle scattered electrons are collected on an annular detector as the probe is scanned across the sample. At high angles (> 50 mrad) Rutherford scattering dominates, where the contrast is proportional to the atomic number and the spatial resolution is essentially determined by the probe size.[144]–[146] If the probe size is sub-atomic (in this case it is ~1.4 Å) this technique not only produces atomic resolution images that are relatively straightforward to interpret, but also leaves the beam transmitted down the optic axis available for other measurements. Here, STEM is combined with EELS for sub-nanometer electronic and chemical characterization.

Spectroscopy in a TEM is based on measuring the intensity distributions of the inelastically scattered fast electrons, i.e. electron energy-loss spectroscopy (EELS), using a post-column magnetic sector spectrometer. The inner-shell excitations are principally determined by the matrix

element $\langle\Psi_f|\exp(i\,\mathbf{q}\cdot\mathbf{r})|\Psi_i\rangle$, where Ψ_i is the initial core-electron state, Ψ_f is the final ionized electron state, and **q** is the momentum transfer. The electron energy-loss spectrum observed in a TEM is largely forward peaked, i.e. **q** is small and the main contribution to the inelastic scattering is the linear term $\langle\Psi_f|(i\,\mathbf{q}\cdot\mathbf{r})|\Psi_i\rangle$ and dipole selection rules, $\Delta l = \pm 1$ apply. For the transition metals (Fe, Co, Mn) the $2p \rightarrow 3d$ (unoccupied) transitions, known as "white lines" due to their appearance when recorded on film, show strong features in the EELS spectrum in the 500-1000 eV range optimal for practical measurements in existing instruments. The edge onset and the fine structure of both the oxygen K edge and iron L edge can also be used to identify physical or chemical variation in iron oxides. [143], [147], [148] In particular, splitting of the iron L edge pre-peak is dependent on the oxidation state as well as coordination and may be useful for phase identification if sufficient energy resolution is achieved with a monochromated instrument.

Valence in transition metal oxides is proportional to the onset energy and intensity ratio of various core-loss edges. Electronic transitions from the $2p$ levels to unoccupied $3d$ states (L-edge) are sensitive to atomic electronic structure and can be used to specify the iron oxide phase at hand. L-edge electrons absorb different energies due to spin-orbit splitting of the $3d$ states. For iron, the lower energy L_3-edge onset is approximately 708 eV, and the higher energy L_2-edge onset is approximately 721 eV. Considering only the relative population of the initial states an L_3/L_2 intensity ratio of 2:1 may be expected; however, spin coupling between the $2p$ core hole and the final $3d$ state causes deviation from this ratio. This L_3/L_2 ratio has been shown to depend on the oxidation state of the transition metal, with an increasing iron oxidation state resulting in a larger relative intensity of the iron L_3 edge. [72], [116] Quantification of the white line ratio for transition metals can be done by curve fitting, using different integration windows, and/or various digital filters. [72], [74], [76], [116], [143] Here, we compute the intensity ratio of the L_3 to L_2 edges from

the second difference spectrum to improve detection efficiency, minimizing dose to the sample. [72], [76] Regardless of the method of calculation, the intensity ratios of the iron L_3 to L_2 edges are generally consistent and proportional to the oxidation state for the iron oxide phases. For iron oxides, the L_3/L_2 ratio varies from approximately 4:1 for Fe^{2+} to 6:1 for Fe^{3+}. By acquiring the EEL spectra at points across individual nanoparticles, the iron L_3/L_2 intensity ratio and the nanoscale variation in iron oxidation state and phase is measurable within a single nanoparticle. Figure 4.2 shows an atomic resolution STEM image and the L_3/L_2 intensity ratio measured from an EELS line scan across the nanoparticle.

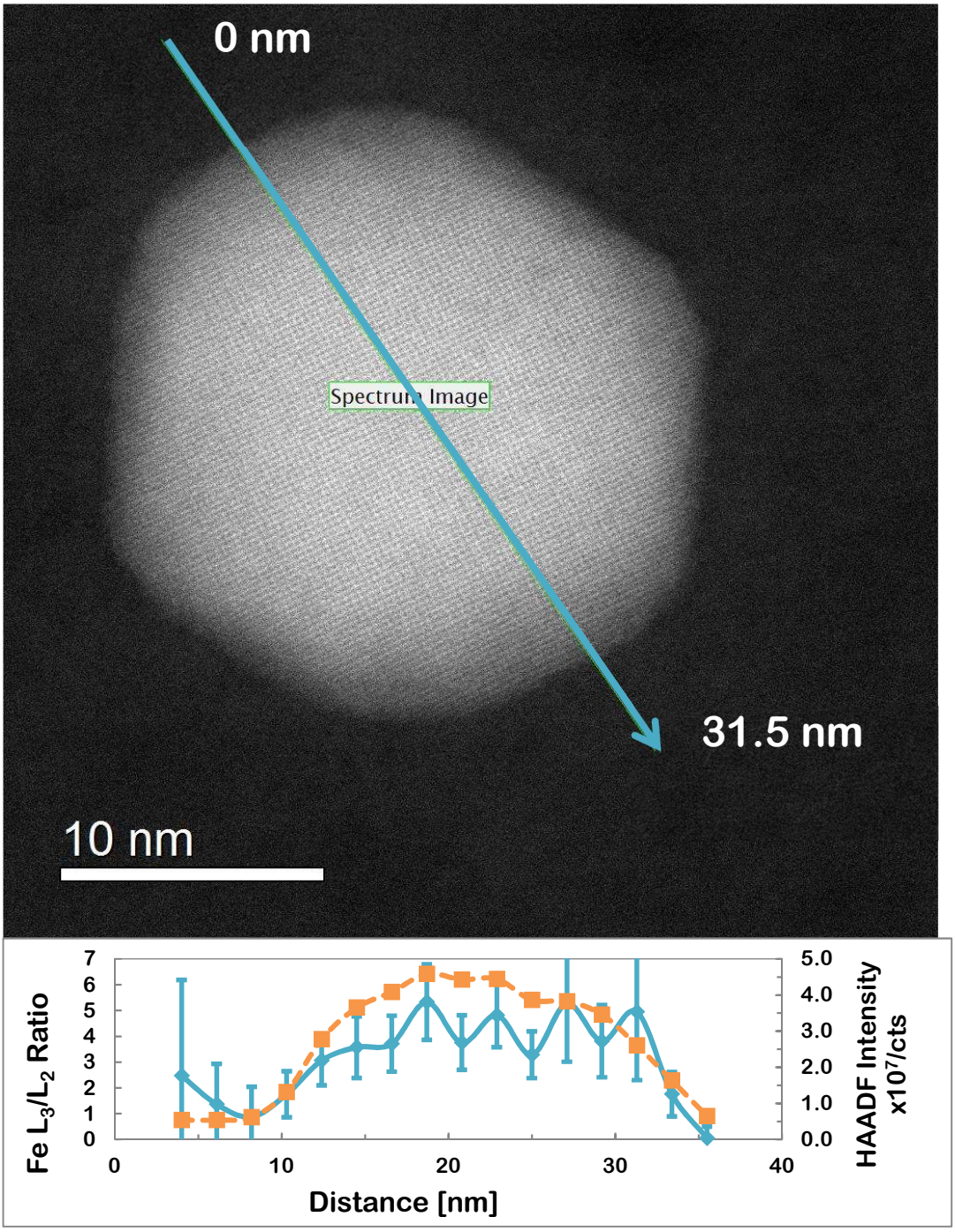

Figure 4.2. HAADF STEM image and corresponding EELS line scan of a superparamagnetic iron oxide nanoparticle. Atomic columns are visible, and this particle is single crystalline and faceted. Plot shows the HAADF intensity (dashed orange) to locate the particle, and the L_3/L_2 ratio (solid blue) across the particle.

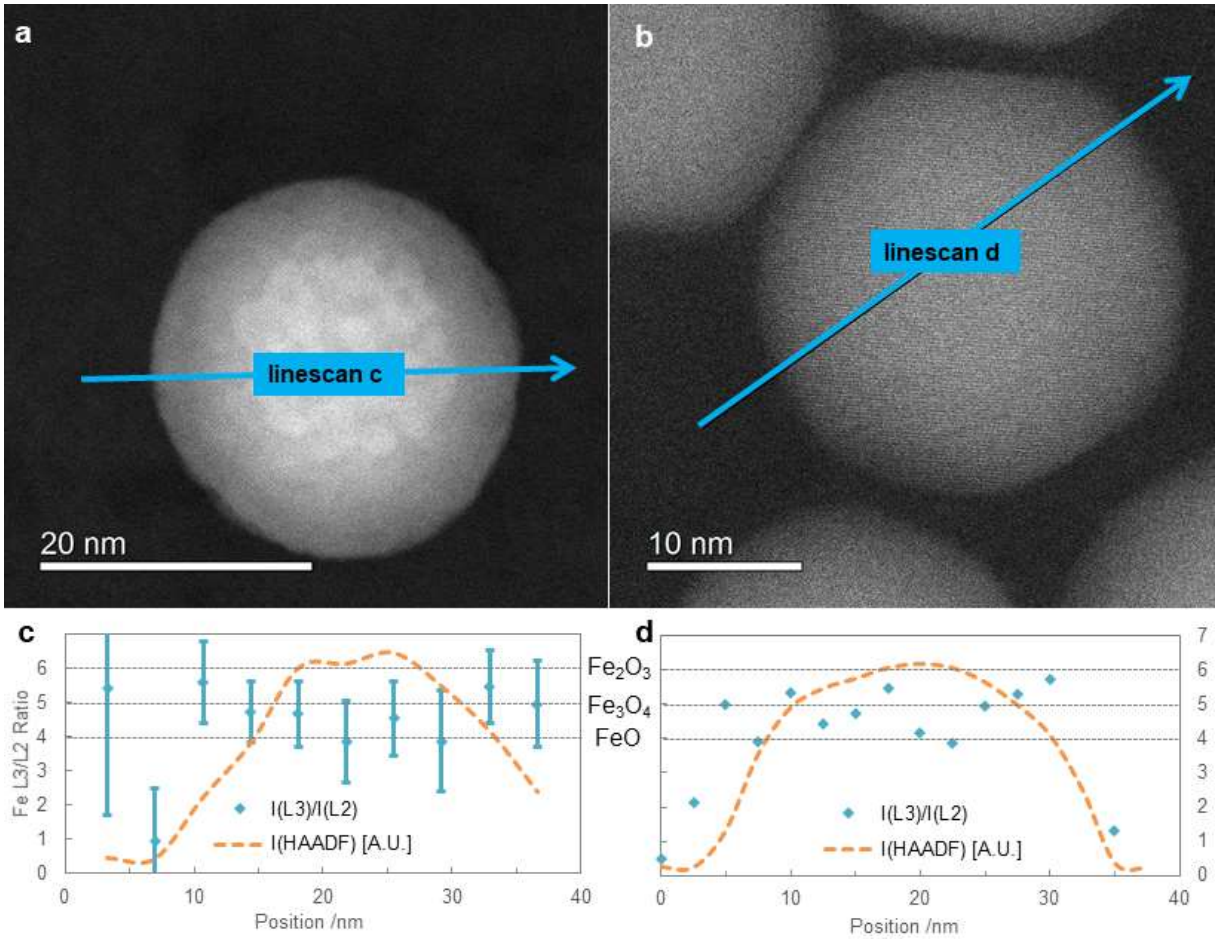

Figure 4.3. High resolution STEM images of nanoparticles reveal the core-shell structure in the unoptimized sample (a). The L_3:L_2 intensity ratio measured across the particle (c) indicates an increased oxidation state on the surface, consistent with a wüstite core and magnetite shell. In contrast, the optimized, spinel iron oxide nanoparticle (b) shows uniform contrast indicating a defect-free crystal, and consistent L_3:L_2 ratio (d). The HAADF scattering intensity, indicative of relative mass/thickness, is included to indicate the position of the particle.

First, we consider the optimized magnetite nanoparticles. The average L_3/L_2 ratio for all particles analyzed in the sample was 4.9, corresponding to a mix of Fe^{2+} and Fe^{3+} and consistent with magnetite.[72], [116] An example STEM image of one representative nanoparticle is shown in Figure 4.3b. This sample is single crystalline and defect free, as is demonstrated by the uniform contrast and continuity of lattice fringes. An EELS line scan was performed, where EEL spectra

were collected as the probe was rastered along the nanoparticle diameter. The line was divided into 16 segments and each spectrum was collected for 0.5 seconds with the beam continuously scanning during this time to distribute the incident electron dose and avoid radiation damage. For each spectrum, the intensity ratio of the L_3/L_2 edges was calculated and plotted as a function of distance across the particle. The dashed lines represent reference ratios for wüstite, magnetite, and hematite.[72] For this particle, the average L_3/L_2 ratio is 4.8, roughly corresponding to magnetite, with a slight excess of Fe^{2+}. There is significant point to point variance in the ratio due to local variations in composition and measurement uncertainty, represented by a standard deviation of 0.6. Within this uncertainty, this sample has a consistent L_3/L_2 ratio, and a corresponding oxidation state of approximately 2.5+ throughout the individual particle.

Next, we consider the mixed phase iron oxide nanoparticles. The SAED pattern, inset in Figure 4.1b, already shows presence of both wüstite and spinel crystal structures. Curiously, there is no indication of whether the two phases occur as separate nanocrystals or if there is phase separation *within an individual* nanoparticle. Immediately apparent from the contrast in the STEM images is the core-shell structure of these nanoparticles, shown in Figure 4.3a. The higher contrast suggests that the core is a denser phase than the shell. To confirm this, we perform an EELS line scan across the particle. The shell has a L_3/L_2 ratio of approximately 5 (corresponding to magnetite) while the core has a smaller L_3/L_2 ratio of 4-4.5 corresponding to the lower oxidation state of wüstite. This arrangement indicates the particles oxidized from the surface but the phase transformation is not complete, resulting in a wüstite/magnetite core/shell nanoparticle. The particle is 23% wüstite core by volume measured on the HAADF images, or 13% wüstite by nanoparticle volume measuring the from the EELS signal.

Overall, STEM-EELS is a unique combination of high spatial resolution imaging with high energy resolution chemical analysis. This is particularly suited for measuring local variations, but without proper reference samples or correlated measurements, precise quantification is challenging. The primary constraint of using STEM to characterize nanoparticles is the sample size, and is typically limited to several nanoparticles in a microscopy session. To address this sampling issue, we study these same samples by Mössbauer spectroscopy, providing a measure of the average properties of the nanoparticles.

4.3 Mössbauer Spectroscopy of Iron Oxide Nanoparticles

Mössbauer Spectroscopy is a nuclear scattering technique wherein the energy shift of gamma rays emitted from ^{57}Fe are measured after interaction with a specimen. In this way changes in the nuclear energy levels due to hyperfine fields are measured, providing information about the electronic structure and magnetic properties of the sample. In Mössbauer Spectroscopy, resonant absorption of γ-rays is caused by transitions between nuclear energy levels and hyperfine interactions between nuclei and surrounding electrons will be represented in the Mössbauer spectra. The primary interactions are 1) chemical or isomer shift due to interactions between the nucleus and *s*-electrons, 2) quadrupole splitting due to electric field gradients producing doublet peaks, and 3) magnetic hyperfine, or Zeeman, splitting due to interactions with valence electrons and magnetic fields producing sextet peaks. Iron oxides exhibit all of these interactions, depending on the phase and magnetic properties. An external magnetic field can be applied parallel to the γ-ray propagation during the measurement to distinguish antiferromagnetic (FeO) from ferrimagnetic (inverse-spinel) phases. Tetrahedral and octahedral iron will have the opposite response to the applied field, so this can be used to improve resolution of the two sites. [3]

SPIONs will exhibit different temperature-dependent behavior than bulk iron oxide. Above the superparamagnetic blocking temperature, T_B, the particles will show rapid magnetic relaxation, similar to paramagnetism.[149] This will result in increased line widths and asymmetry in the Mössbauer sextet spectrum, or, alternatively, in the observation of a doublet structure upon reaching fast superparamagnetic relaxation at higher temperatures. Below T_B relaxation is slow and the magnetization is quasi-static over the course of the measurement time (so this phenomena is also time dependent) and the superparamagnetic behavior will be blocked. [141], [150], [151]

Mössbauer spectroscopy was used to characterize the composition and magnetic structure of the two samples.[8] Figure 4.4 shows Mössbauer spectra from 27 nm inverse-spinel particles recorded from 4.2 – 295K. At 4.2K, the spectrum displays the characteristic inverse-spinel structure with three major sextet components corresponding to octahedral Fe^{3+} (green) and Fe^{2+} (blue) and tetrahedral Fe^{3+} (cyan). The intensity of each subspectrum is approximately proportional to the number of corresponding iron atoms and we can estimate the fraction of iron ions in the Fe^{2+} valence state and the composition of magnetite and maghemite by comparing it to the intensity of the Fe^{3+} subspectra of tetrahedral A- and octahedral B-sites. In magnetite ($[Fe^{3+}]_A[Fe^{3+}Fe^{2+}]_BO_4$), the relative intensity of the three subspectra should be identical, corresponding to the equal proportions of Fe^{3+} (A), Fe^{3+} (B), and Fe^{2+} (B). In maghemite, which can be understood as Fe^{2+}-deficient magnetite ($[Fe^{3+}]_A[Fe^{3+}_{5/3}\square_{1/3}]_BO_4$, with □ representing B-site vacancies) no Fe^{2+} is present, corresponding to a ratio of Fe^{3+} (A) to Fe^{3+} (B) and Fe^{2+} (B) given by 1:5/3:0. By fitting the experimental spectra to these subspectra using a least-squares fitting routine, a magnetite contribution of 70% is determined, with the remaining 30% from maghemite.

---

[8] Mössbauer spectroscopy and analysis were performed by colleagues Joachim Landers, Soma Salamon, and Heiko Wende at University of Duisburg-Essen. [44]

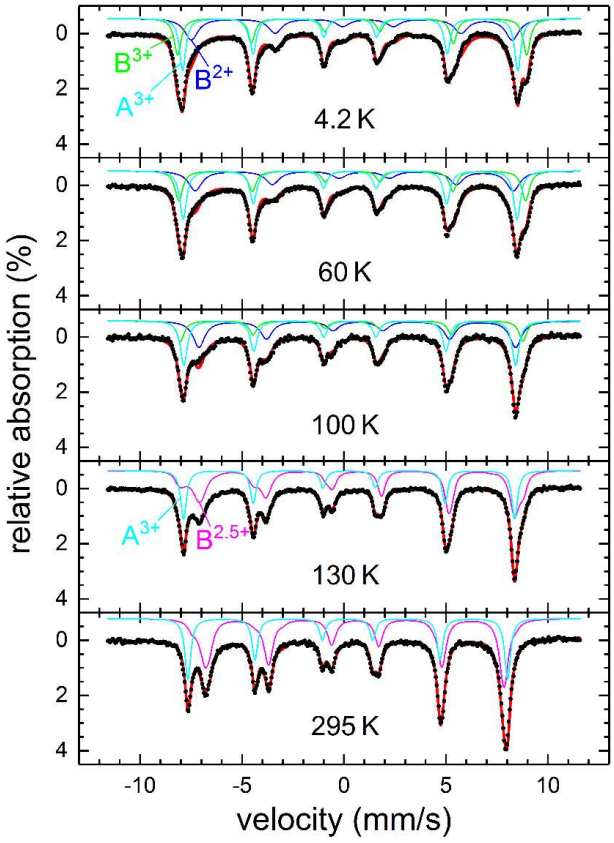

Figure 4.4. Mössbauer spectra of 27 nm optimized iron oxide nanoparticles measured at temperatures from 4.2K-295K. Experimental data (black dots) is fit (red) to subspectra: B-site Fe^{3+}(green), B-site Fe^{2+}(blue), B-site$^{2.5+}$(magenta), A-site Fe^{3+}(cyan)

In addition to the presence of the B-site Fe^{2+} subspectrum, magnetite can also be distinguished at low temperatures by the Verwey transition, taking place at about 120K in bulk Fe_3O_4, [152] accompanied by a distinct change in spectral structure. [153], [154]. Here, the merging of B-site Fe^{2+} and Fe^{3+} subspectra is most prominent between 100K and 130K. At higher temperatures (130K and 295K), they merge to one sextet sub-spectrum representing both sites in a mixed $Fe^{+2.5}$ valence state (magenta). Despite the expectation that this sample should exhibit superparamagnetism, this Mössbauer spectrum shows static properties without distinct signs of

fast superparamagnetic relaxation. This could be explained by the nanosecond time scale of the Mössbauer experiment, resulting in much higher blocking temperatures compared to slower techniques, such as MPS. Figure 4.5 shows Mössbauer spectra of the mixed phase, wüstite-magnetite core-shell particles recorded from 30-240K.

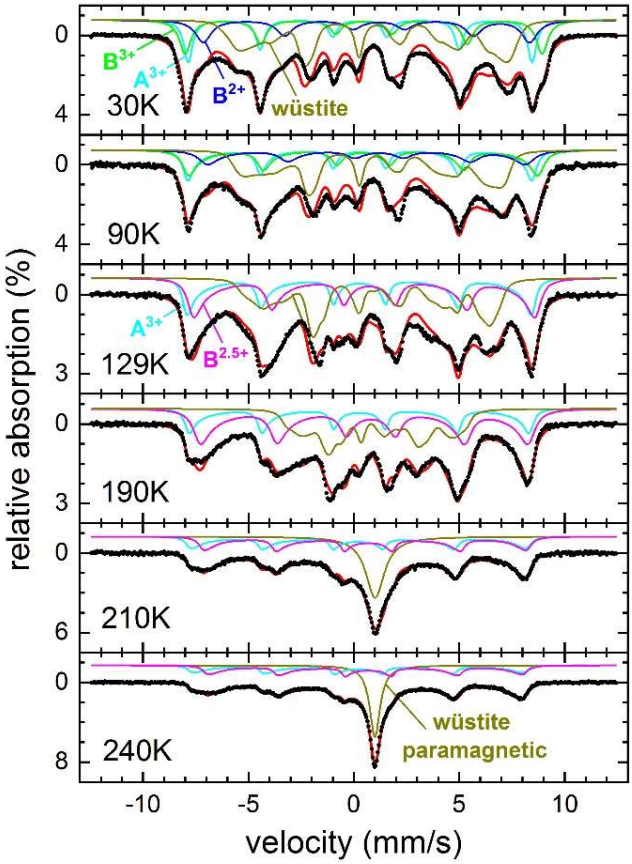

Figure 4.5. Mössbauer spectra of wüstite-magnetite core-shell particles recorded from 30-240K. Experimental data (black dots), least-squares fits (red lines), and fitted subspectra: B-site Fe^{3+}(green), B-site Fe^{2+}(blue), B-site$^{2.5+}$(magenta), A-site Fe^{3+}(cyan) and wüstite(olive)

The different iron sites in magnetite in the mixed phase particles are represented by 3 subspectra (green, cyan, blue) below and two subspectra (cyan, magenta) above the Verwey transition. The transition is not clearly visible, unlike in the pure magnetite sample, due to the superposition with the wüstite subspectrum (olive) and changes in spectral structure due to Néel-

type relaxation. To reproduce the increasingly asymmetric lineshape as the temperature is increased and approaches the blocking temperature, TB, of the particles, the Jones-Srivastava many-state relaxation model was used. [155] Considering both superposition and line broadening, the magnetite/maghemite composition of the shell cannot be completely determined by this measurement. Nonetheless, the considerable difference in isomer shift (the center position of the spectrum) between B-site subspectra (e.g. green to violet at 240K) indicates an Fe2.5+ state, suggesting that there is at least some magnetite in the particle shell.

The remaining 35-40% of the spectral area can be assigned to the additional wüstite phase in the particle cores, as the prevalence of the paramagnetic singlet at 210K and above agrees well with the bulk wüstite Néel temperature TN, which is close to 200K. However, wüstite is known to exhibit very complex Mössbauer spectra, as it often manifests in off-stoichiometric composition (FexO instead of FeO), resulting in vacancies and Fe3+ ions in addition to Fe2+. The observation of a slightly broadened singlet instead of a doublet above TN may indicate oxygen deficiency, as higher oxygen content in off-stoichiometric wüstite samples in the paramagnetic state are reported to display an increasing doublet line splitting. [156]

To study the orientational behavior of particle magnetic moments and to enhance resolution of individual subspectra, Mössbauer spectra of both samples have been recorded in an external magnetic field of 5T as shown in Figure 4.6. Magnetite nanoparticles show nearly complete spin alignment, as indicated by the low intensity of sextet lines 2 and 5 (marked by arrows), reflecting a state close to saturation magnetization. A- and B-site contributions can be clearly resolved, as the antiparallel arrangement of magnetic moments on tetrahedral and octahedral lattice positions results in a considerable increase in sextet splitting for the A-site and decrease for the B-site when an external field is applied. [157]

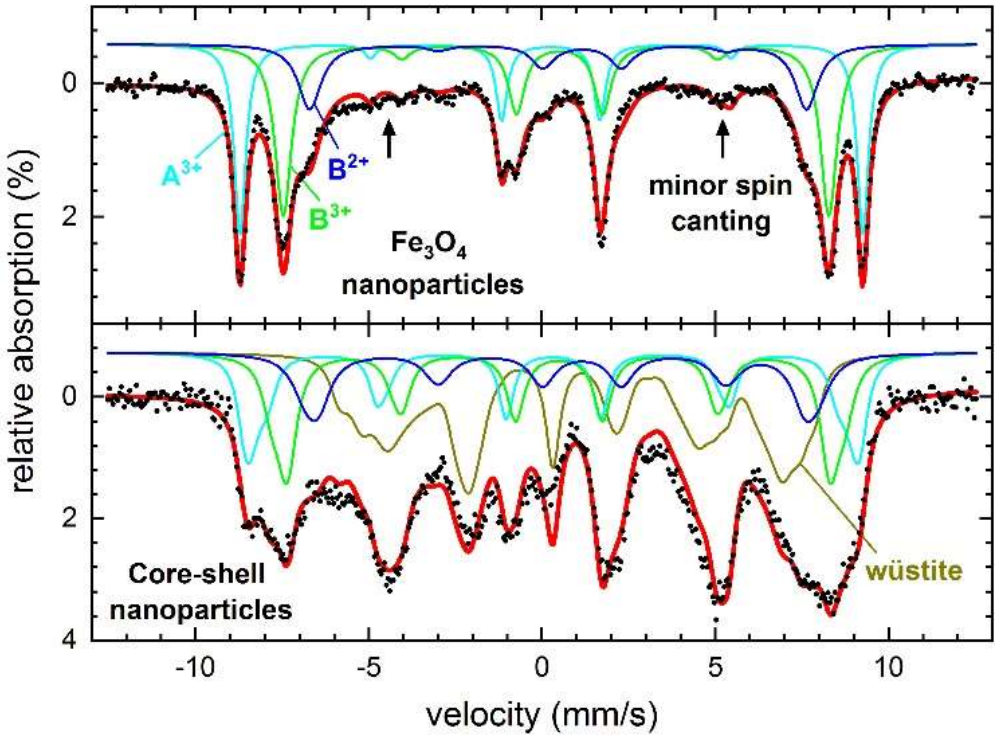

Figure 4.6. Mössbauer spectra of wüstite core-shell particles (bottom) and spherical magnetite nanoparticles (top) measured at 4.3K under an applied field of 5T.

In comparison, mixed phase core-shell particles display distinct spin canting, where spins are tilted slightly off axis rather than being exactly antiparallel, visible by the enhanced intensity of lines 2 and 5 of the magnetite subspectra and in the broad sextet distribution representative of the antiferromagnetic wüstite phase. Poor resolution of A- and B-site subspectra is obtained, due to the low degree in magnetic alignment along the external field. Strong spin canting in wüstite is to be expected, as antiferromagnetically coupled magnetic moments show negligible alignment in applied magnetic fields. Magnetite usually exhibits low magnetic anisotropy, resulting in low degrees of spin canting, as seen for the optimized sample. Spin canting often occurs at the surface, and is more pronounce in smaller nanoparticles. [158] The observation of spin canting in the

magnetite subspectrum of the mixed-phase sample therefore indicates strong interface coupling to the non-aligning wüstite phase, being consistent with the observation of the core-shell particle structure from TEM.

4.4 Summary of IONP Phase Characterization

By combining Mössbauer Spectroscopy with EELS, we have successfully differentiated iron oxide phases, quantified the phase composition, and determined the chemical as well as the spin structure of individual mixed phase nanoparticles. By identifying iron oxide phases from their characteristic chemical shifts and spectral structure, the composition of the two SPION samples is quantified using Mössbauer spectroscopy. The optimized sample is composed of pure inverse-spinel iron oxide, resulting in magnetic behavior suitable for biomedical applications. Meanwhile, the as-synthesized sample contains approximately 40% wüstite, resulting in undesirable magnetic properties. Since Mössbauer spectroscopy is a bulk technique probing the collective response of many nanoparticles, it is not clear from Mössbauer spectroscopy alone whether the phases observed were from separate nanoparticles or if each nanoparticle contained multiple phases, although strong spin canting in the magnetite subspectra of the mixed phase samples is evidence of a core-shell structure. To determine the local composition, EELS was performed on individual nanoparticles within each of these samples. This demonstrated that the as-synthesized, mixed phase particles have a core-shell structure, consisting of a 10-20% wüstite core and the remainder a magnetite shell. Due to the small number of particles studied by EELS, this does not contradict the phase quantification of 40% wüstite from Mössbauer, which is more representative of the entire sample. Complementary characterization techniques are necessary to determine iron oxide nanoparticle phase and structure. STEM-EELS was used to characterize structure at the nanometer level, however by their nature, high-resolution techniques can only sample a limited area. Here,

Mössbauer Spectroscopy provided a statistically robust characterization of phase morphology on the nanoscale, oxidation state, and the spin structure. For applications such as MPI where desirable properties depend on nanoscale structure and composition, correlation of bulk and nanoscale measurements provides insight into developing particles with optimal magnetic characteristics.

Following the detailed materials characterizations discussed in the previous chapters I will now return to nanoparticle nucleation, growth, and colloidal kinetics. Because SPIONs are synthesized by non-equilibrium reactions, kinetics are inherently important to their structure and properties. The most direct way to quantify kinetics is by observing chemical reactions in real-time, i.e. *in situ,* which will be covered in the following chapter.

Chapter 5. *IN SITU* TRANSMISSION ELECTRON MICROSCOPY OF IRON OXIDE NANOPARTICLES

Nanoscale colloidal processes such as nucleation, growth, dissolution, and self-assembly govern many environmental and biological systems. [159], [42], [160] Many diverse and important technologies also depend on the properties of colloidal nanoparticles, from catalysis [161], [162] and energy storage [163] to medical applications. [1], [22], [164] For targeted applications of nanoparticles, it is critical to understand how colloidal stability is determined by the dynamics of the solid-liquid interface. This is particularly important at the interface of nanoparticles with complex biological systems, where safety and efficacy of therapeutics depend on our understanding of these phenomena. [165]–[168] Iron oxide nanoparticles are one prominent example, with a wide variety of biomedical imaging and therapeutic applications. [1], [22] Iron oxides are prevalent in nature, generally non-toxic, and inexpensive to synthesize. [17], [19], [169], [32] These benefits, combined with their magnetic properties, make iron oxide nanoparticles an ideal platform for many engineered biomedical applications. Stability of iron oxide nanoparticles depends on their environment—inside biological cells, iron oxide nanoparticles accumulate in lysosomes, which break down foreign objects in part by dissolving in their acidic enzymatic environments. [78], [170]–[172] While iron oxide nanoparticles may be functionalized with various chemical species for targeting or other functionality, [31], [173], [174] this modification affects the nanoparticle surface chemistry and charge, mediating interactions with ions or other species in solution, and affecting their colloidal stability. [175]–[178]

The solid-liquid interface is often considered as an electric double layer (EDL)—an inner layer of strongly adsorbed solvent ions forms at the surface, while further away from the particle, in the Stern and diffuse layers, loosely associated ions move under the influence of Columbic

forces and Brownian motion.[179]–[181] To predict colloidal stability, the zeta potential (ζ) is defined as the electric potential, relative to the bulk solution, at the slipping plane of the solid-liquid interface. While convenient to measure experimentally using dynamic light scattering (DLS), ζ does not directly describe conditions within the EDL or the Stern layer where ion exchange, adsorption, and other important interfacial phenomena occur. Furthermore, the classical EDL model does not provide an analytical description for spherical particles or in ionic liquids.[182] Recent investigations of solid-liquid interfaces have relied on a combination of molecular dynamic simulations,[183]–[186] and experimental observation with scanning probe techniques.[160], [182], [187] Understanding the interfacial kinetics of colloidal stability ultimately requires development of techniques capable of direct, real-time observation. In this chapter, we directly observe iron oxide nanoparticles *in situ,* with liquid cell Transmission Electron Microscopy (TEM), to quantify how surface chemistry and solution conditions affect nano-colloidal stability.

5.1 Liquid Phase TEM

Transmission Electron Microscopy (TEM) is a powerful tool for characterizing structure and chemistry at the nanoscale, and modern detectors and dynamic TEMs have pushed temporal resolution to the timescales necessary to study many chemical reactions.[188], [189] *In situ* techniques aim to simulate relevant environmental conditions, e.g. liquids,[190], [191], [63], [192] gasses [193], [194] or external stimuli [188], [195] inside the TEM column. While *in situ* TEM is not a new approach, [55] the recent development of specialized holders and instruments have made *in-situ* experiments more practical. Developments in *in situ* Transmission Electron Microscopy (TEM) have enabled the observation of many chemical and materials processes in relevant environmental conditions and at the necessary length and timescales. The understanding of

nanoparticle nucleation and growth phenomena is one area that has benefited tremendously from this technology. By encapsulating a liquid sample between impermeable, electron transparent membranes, i.e. Si_3N_4 [190] or Graphene [196], nanoparticles can be synthesized inside the TEM and imaged throughout the reaction. In this way platinum, [197] gold, [198], [63] and lead sulfide, [64] have been synthesized *in situ.* In these systems the electron beam facilitates reduction of an aqueous metallic salt precursor, so electron dose calibration and control is crucial. [192] There has been some investigation of surfactant mediated nanoparticle growth[65], but *in situ* TEM techniques have not yet been applied to the wide variety of organic-phase nanoparticle syntheses.

Liquid TEM enables observation of nanoparticle growth and stability, [65], [197], [199], [200] oriented attachment, [185] and electrochemistry, [201]–[203] providing unique insight into the nature of the solid-liquid interface. Imaging with TEM exposes the sample to high-energy electrons, which can initiate secondary reactions or phase changes including nucleation, growth, or dissolution. [65], [197], [199] An excellent example of this is the pH and electron dose dependent stability of gold nanoparticles shown with *in situ* TEM. [200] TEM irradiation of water lowers the solution pH as a function of electron flux density. [199], [204] Importantly, the lowered pH under electron irradiation can be used to induce nanoparticle transformations in conditions analogous to other acidic aqueous conditions.

5.1.1 *Graphene Liquid Cells*

An option for performing *in situ* TEM synthesis experiments is encapsulation in graphene Liquid Cells (GLCs) where a liquid sample is encapsulated between two monolayers of graphene. Typically, one layer of graphene is on TEM grid and the liquid sample is deposited on the graphene. The top layer is chemical vapor deposited (CVD) graphene on a copper foil. The copper foil is etched away, and the graphene monolayer is retrieved and placed on top of the liquid droplet.

GLCs offer several advantages over conventional liquid stages. Primarily, a monolayer of graphene produces much less contrast than tens of nanometers of Si_3N_4, allowing for higher resolution imaging. Secondly, a GLC can be used with any holder, on any microscope. GLCs can be stable for months. Graphene is impermeable to gas, and loss of sample occurs mainly when material leaks out the side, between the two layers. In this way, I prepared GLCs from an aqueous iron oxide nanoparticle sample, shown in Figure 5.1. Iron oxide nanoparticles are observed to be encapsulated between Graphene layers.

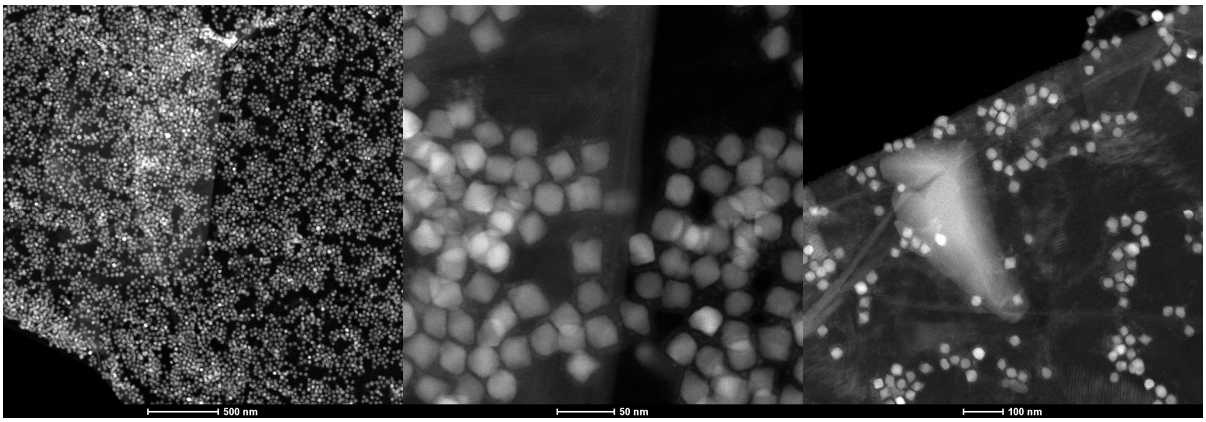

Figure 5.1. GLCs prepared with aqueous sample of iron oxide nanoparticles.

GLCs have been successfully implemented to study gold nanoparticle [196] nucleation and growth of as well as the ferratin complex, [205] and appears to be well-suited to high-resolution studies of small molecules or particles in solution. I have sealed hydrated iron oxide nanoparticles between graphene layers, but for this sample GLCs were not the best option for studying liquid phase phenomena. Because these particles were relatively large (nearly 30 nm) the graphene layers were too tight fitting, conforming to the particles, immobilizing them, limiting motion, and diffusion of water and solutes.

5.1.2 *Liquid TEM Sample Holders*

In situ TEM experiments are performed on an FEI Titan 80-300™ STEM with Hummingbird liquid stage, using closed cell (no flow) and SiN_x with no spacers. Fluid thickness determined with EELS is 100-200 nm near the window edge where these experiments are performed. STEM probe current is calibrated with a Faraday cup sample holder; the electron flux density ($e^- Å^{-2} s^{-1}$), sometimes referred to as "dose rate," is calculated my multiplying the current by the frame time, including flyback time.[192] For these experiments the calibrated probe current is approximately 10 pA at the specimen plane, except when otherwise noted, and electron flux density is controlled by increasing STEM magnification to scan the probe over a smaller area.

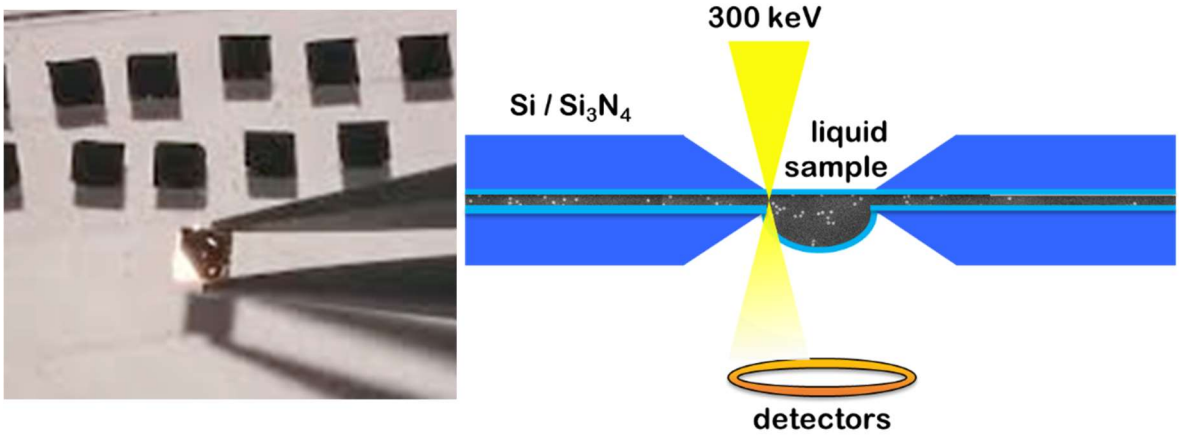

Figure 5.2. Picture of chips with SiN_x windows for liquid cell TEM and a schematic of the assembled TEM liquid cell in cross section. The windows are flat under ambient conditions, but pressure gradients in the vacuum of the TEM cause window bulging of 1 µm or more.

Figure 5.3 shows some examples of iron oxide nanoparticles imaged *in situ* in both aqueous and organic solvents in STEM and TEM.

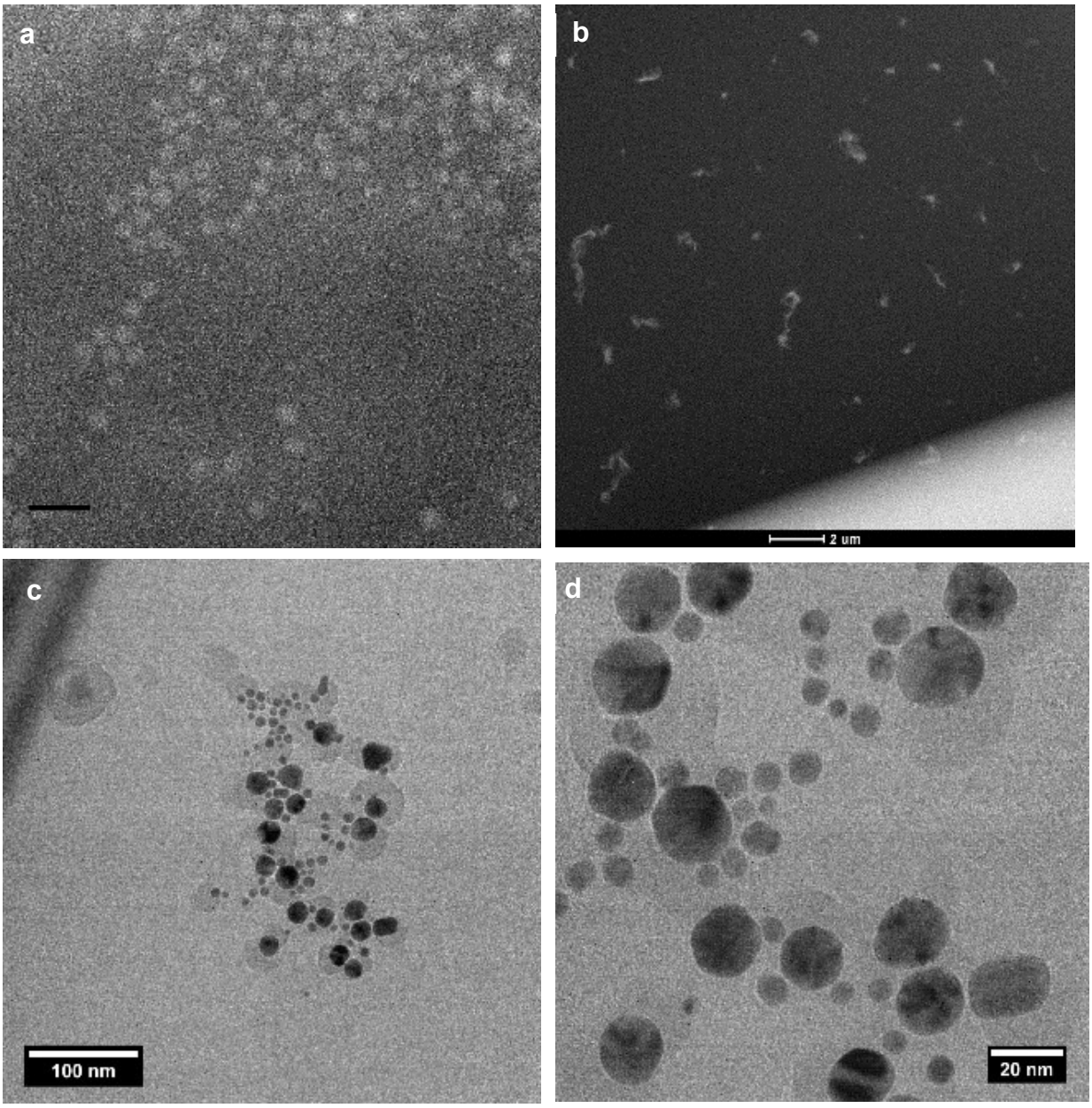

Figure 5.3. *In situ* TEM images of iron oxide nanoparticles. **(a)** STEM of iron oxide nanoparticles in growth solution (1-octadecene and oleic acid), scale 50 nm. **(b)** STEM of iron oxide nanoparticles in water assembled into chains and clusters. (**c** and **d**) Bright-field TEM of PMAO-PEG coated iron oxide nanoparticles in water.

There is suitable contrast to detect nanoparticles in both 1-octadecene and water. In all these samples no spacers were used. Thickness can be estimated with EELS, using the log-ratio of the zero-loss and Plasmon peaks. [206] In my experience, liquid layer thickness is generally around 100 nm near the edge of the window and 500 nm or more closer to the center, with these 50 nm thick, 250x250 um^2 windows. In the bright field TEM of aqueous nanoparticles, Figure 5.3 c and d, the PMAO-PEG coatings encapsulating the particles are visible. This sample is polydisperse but was the first aqueous sample available and is suitable for purposes of testing resolution and liquid cell assembly.

5.2 *IN SITU* ELECTROLYTIC DECOMPOSITION OF IRON OLEATE

A primary goal of my research is synthesizing iron oxide nanoparticles (NPs) *in situ* in the TEM. This will allow for direct imaging of nanoparticles during nucleation and growth in order to observe the dynamics of NPs during and after synthesis. This can lead to a better understanding of the effects that different synthesis parameters such as composition, surface chemistry, time, and temperature (or electron dose) have on the resulting nanoparticles or their stability in solution. These results would allow for improved synthetic control and reproducibility. Additionally, by comparing the results of *in situ* TEM synthesis with the *ex situ* syntheses, we hope to correlate electron dose to temperature.

The holder used for these liquid TEM experiments is a modified gas stage manufactured by Hummingbird Scientific (Lacey, WA). A liquid sample is sandwiched between two silicon chips with electron transparent silicon nitride (Si_3N_4) windows (Hummingbird Scientific or Norcada) and clip over the tip of the holder compresses an O-ring and applies pressure to the windows from both sides. Spacers can be used, or the thickness can be determined by the

encapsulated liquid. The cell can be connected to an external line for continuous flow or experiments can be closed cell. Most of the experiments presented here are closed cell.

Generally for TEM experiments, and especially for liquid phase experiments, it is important to monitor electron dose. Dose in this experiment was calculated using the equation $(i_e \bullet t)/(e \bullet A)$, where i_e is the calibrated beam current at the sample, t is time, e is the electron charge, and A is the illumination area. [192] For TEM mode, the parameters used to control dose rate are the current (manipulated, e.g., with spot size and condenser apertures) and illumination area. In STEM mode, dose is controlled with the probe current, dwell time, and area (magnification). Dose is usually set and measured at the beginning of an experiment, so throughout the experiment only the magnification (and beam spread in TEM) are changed.

Iron (III) oleate is a common precursor used in the synthesis of iron oxide nanoparticles. Our group has extensively optimized and characterized this system to produce monodisperse, superparamagnetic iron oxide nanoparticles. Decomposition of iron (III) oleate, with 1-octadecene as the solvent, results in iron supersaturation followed by nucleation and growth of iron oxide nanoparticles. Reaction kinetics are often tailored with the addition of excess oleic acid.

Iron (III) oleate has been electrolytically decomposed with *in situ* TEM. A solution of iron (III) oleate in 1-octadecene (0.1695 mMol/g) with no excess oleic acid was placed between two silicon nitride membranes in the Hummingbird stage and imaged with bright field TEM. Time series screen shots from the recorded movies are shown in Figure 5.4 below. Under the influence of the electron beam at doses above approximately 10^3 A/m^2 (~60 e^-/Å^2 s), the precursor decomposes and particles nucleate. Below this dose, no transformations are observed within 5 minutes of continuous illumination. The growth rate is dose dependent, with particles first visible at around 75 seconds at a dose rate of 5.7 x 10^3 A/m^2 and not until 105 seconds at 3.9 x 10^3 A/m^2.

Particles are large compared to similar reactions *ex situ,* first visible at 10s of nanometers, and quickly growing to over 100 nm. When performed *ex situ* at approximately 300 °C particles do not grow above approximately 10 nm. *Ex situ* and without excess oleic acid particles nucleate almost as soon as temperature exceeds 250 °C. As a first approximation, the electron dose required to nucleate particles may be compared to this temperature. Based on these experiments that necessary dose is 105 seconds at 3.9 x 10^3 A/m^2 (25,557 electrons), or 75 seconds at 5.7 x 10^3 A/m^2 (18,255 electrons), with a threshold dose rate of ~60 e^-/Å^2 s.

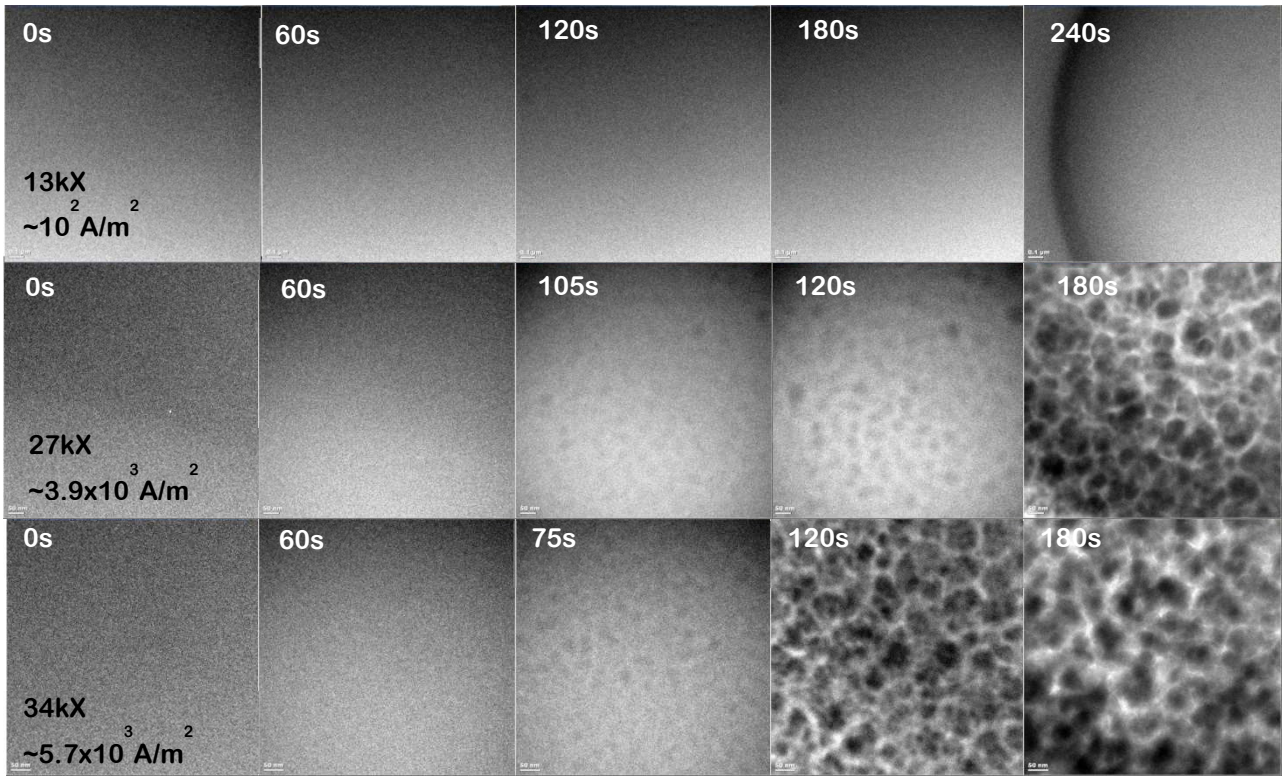

Figure 5.4. Bright field TEM images (screen shots from movies) of the electron beam induced decomposition of iron (III) oleate. Top row: at 10^2 A/m^2 and below no nanoparticle growth occurs; Middle: 10^3 A/m^2 Above dark contrast, iron-rich nanoparticles nucleate by 105 seconds; Bottom: Nucleation time decreases with increasing dose, at 5.7 x 10^3 A/m^2 nanoparticles nucleate by 75 seconds. Scale bar is 50 nm for all images.

STEM mode does not induce the decomposition of iron oleate across a wide range of doses, from several $e^-/Å^2$ s up to in excess of 500 $e^-/Å^2$ s (approximately the same dose as in TEM). No effects from the electron beam in STEM mode were observed in this system. A critical difference between TEM and STEM is the dose delivery area. To achieve approximately 500 $e^-/Å^2$s in STEM the magnification was 910 kX (several nm^2 illumination area), while in TEM mode it was 69kX. This suggests that longer range diffusion of growth species (10s of nm) may play a role. There may be a requirement for a greater total number for species in an area beyond just a threshold concentration. Some local heating is expected, for example increases of 5 – 30 K under 30 keV SEM illumination has been reported, [207] however, electrolysis is the primary mechanism responsible *in situ* phase transformations.

5.3 Aggregation and Particle Mediated Growth

In systems with strong interparticle interactions, growth may be mediated by the oriented attachment of particles rather than molecular units. An alternate pathway is for growth to be mediated by existing particles, a la Ostwald ripening or by aggregation. Other pathways can be imagined, including phase separation followed by crystallization. [208] In organo-metallic systems, nucleation of complexes and amorphous phases may precede crystallization. In practice, more than one growth mode may occur in a given system, simultaneously or sequentially.

5.3.1 *Self Assembly of Pre-Nucleation Clusters*

Rather than atom-by-atom growth, in many natural minerals growth proceeds by aggregation of pre-nucleation clusters, molecular clusters too small to grow on their own. Ferrihydrite is an iron oxyhydroxide phase prevalent in soils [209], and its structure is composed of a framework of iron Keggin units. Iron Keggin is a 13 iron cluster, plus associated oxygen and

capping ligands, and is a structural building block to ferrihydrite, magnetite, and ferratin. [210] This cluster has only recently been isolated, [210] and provides the opportunity to study particle-mediated growth of iron oxides in a controlled way. The iron keggin cluster is highly charged and reactive and must be stabilized, here by bisumuth (Bi^{3+}) counter ions. With the addition of an appropriate surfactant, cetyltrimethylammonium chloride (CTACl), the cluster disperses in water. Solutions of the dissolved iron keggin clusters in water and acetone were characterized by TEM. In solution, pre-nucleation clusters self-assemble into linear chains, and are imaged using STEM in Figure 5.5 a-c. The structure of these assemblies is reminiscent of ferrihydrite, seen in the electron diffraction in Figure 5.5 e. High-resolution TEM imaging reveals a highly disordered crystal structure. For more information or details on these clusters and experiments see reference [41].

5.3.2 *Aggregation*

Soils are composed of primarily of aggregates of minerals and organic matter. Soils provide a large and poorly understood reservoir of carbon, and persistence of organic matter in soil depends on interactions with minerals. This organic-mineral interaction depends on the chemistry of the organic and mineral surface, and is mediated by environmental conditions including hydration, pH, and ionic strength of solution. To directly observe and quantify these interactions, we have devised a model system for *in situ* TEM consisting of aqueous goethite (α-FeOOH), an earth-abundant iron oxide hydroxide phase, and poly-lysine. Results from these *in situ* STEM movies are shown in Figure 5.6 and further details can be found in reference [42].

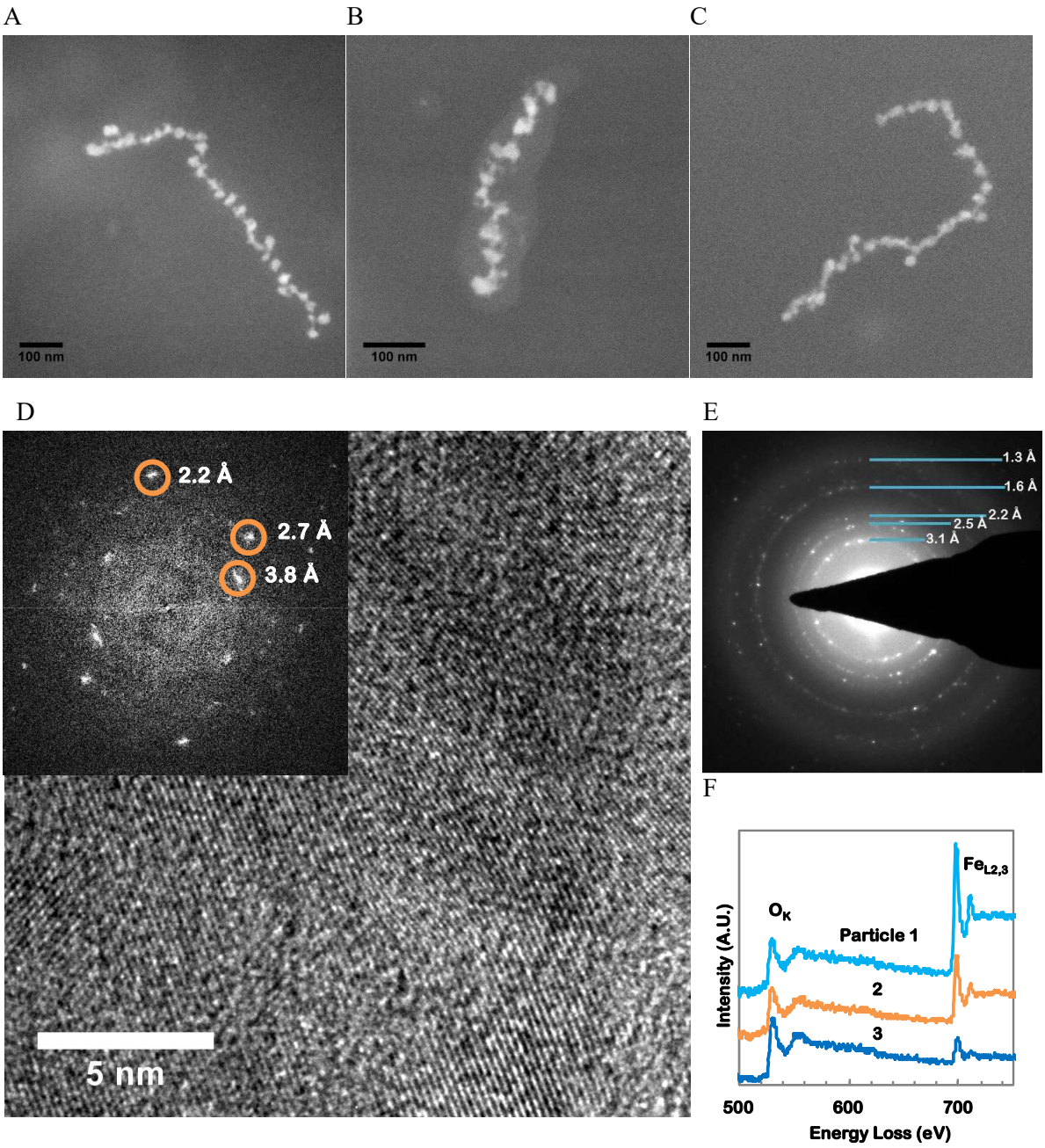

Figure 5.5. Growth of hydrated iron oxide, mediated by self-assembly of iron Keggin ions. [41] *In situ* STEM images of products of Fe_{13} in solution (A-C). Iron oxide/hydroxide particles self-assemble from $Fe_{13}Bi_6(TCA)_{12}$ (A) after 24 hours in acetone or in aqueous solution (B). Similar particles form *in situ* from $Fe_{13}Bi_6(TFA)_{10}(H_2O)_2$,(C) which was otherwise stable in water. Post-mortem analyses confirm structure and phase. Filtered [211] HRTEM (D) shows the highly disordered polycrystalline structure. Lattice spacings in SAD pattern (E) approximately match with ferrihydrite, while iron white-line ratios from EELS indicate a mix of Fe^{2+} and Fe^{3+}.

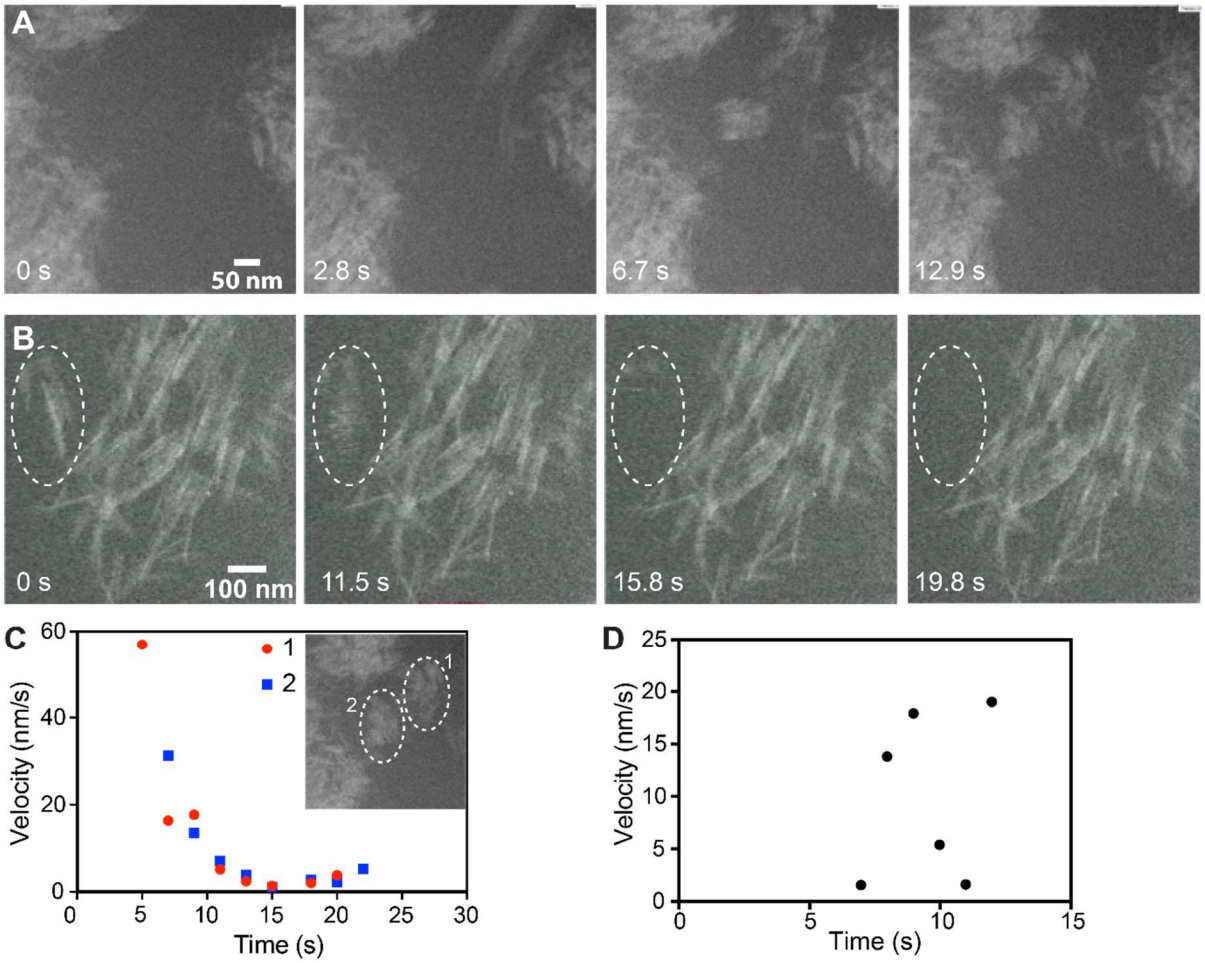

Figure 5.6. *In situ* STEM monitoring the dynamics of goethite nanoparticles in real time. (**A**) Time series demonstrating aggregation with particles interacting with existing assemblages. Images were acquired with an electron dose rate of 1.2 $e^{-}Å^{-2}s^{-1}$. **(B)** Time series demonstrating disaggregation with particles leaving the region of interest (dotted oval). Images were acquired with an electron dose rate of 0.9 $e^{-}Å^{-2}s^{-1}$. (**C**) Velocity is determined by interpolating the change in position between movie frames, of two different assemblages (outlined with dotted ovals, inset) approaching existing mineral clusters in the field of view (**A**). (**D**) Velocity of an assemblage leaving the field of view (dotted oval from panel **(B)**). [42]

5.4 *IN SITU* COLLOIDAL STABILITY OF IRON OXIDE NANOPARTICLES

Colloidal processes including nucleation, growth, ripening, and dissolution are fundamental to the synthesis and application of engineered nanoparticles and numerous natural systems.[9] In nano-colloids consisting of a dispersion of nanoparticles in solution, colloidal stability is influenced by factors such as the particle surface facet and capping layer, as well as local temperature, chemistry, and pH. This relationship is investigated through the real-time manipulation of aqueous colloidal stability of nanoparticles using Scanning Transmission Electron Microscopy (STEM). In a distribution of uniform iron oxide nanoparticles, we use the electron beam to precisely control the local chemistry of the solution and show the critical role that surface chemistry plays in nanoparticle stability. Iron oxide nanoparticles dissolve in acidic environments, and dissolution rates are quantified with direct STEM imaging. By functionalizing the nanoparticle surfaces with charged amino acids and peptides, stability can be tuned to promote dissolution, growth, or agglomeration, sometimes reversibly. In this way, we show how individual nanoparticles can have vastly differing properties from the average nano-colloidal stability, providing insights applicable to nanoparticle synthesis and functionalization, the latter in the context of biomedical applications.

5.4.1 *Acidic Dissolution of Iron Oxide and TEM Liquid Cell Chemistry*

Iron oxides will dissolve in aqueous environments, facilitated by excess hydrogen ions.

$$Fe_3O_4 + 8H^+ \rightarrow Fe^{2+} + 2Fe^{3+} + 4H_2O$$

[9] Portions of this section have been submitted as a manuscript to *Nanoscale* with co-authors Eric Teeman, B. Layla Mehdi, Kannan M. Krishnan, and Nigel D. Browning.

In acidic solutions, Fe^{2+} is the favored equilibrium product, as indicated by the Pourbaix diagram in Figure 1.4. If reductive species are present, represented below as aqueous electrons, further reduction of iron is possible.

$$Fe^{3+} + e^-_{aq} \rightarrow Fe^{2+}$$

$$Fe^{2+} + 2e^-_{aq} \rightarrow Fe$$

Acidification produced by the reductive potential of the electron dose in liquids may be representative of environmentally and biologically significant conditions. Small perturbations of the local conditions, e.g. pH, caused even by relatively low doses of electrons (<1 $e^{-}Å^{-2}\ s^{-1}$) can catalyze dynamic and unexpected phase transformations. This reinforces the importance of understanding, measuring, and reporting *in situ* TEM conditions. [191], [192], [199], [204] The electron flux density and total dose are monitored and kept below damage thresholds. However, if electron-specimen interactions are not considered, beam damage can confuse interpretation. *In-situ* electron microscopy inherently involves interaction between high-energy electrons and the sample. [191], [192], [199] An important consequence of electron-water interactions is the production of charged species in solution. [199], [204] The number of possible reactants is quite manageable for pure H_2O:

$$H_2O + e^- \xrightarrow{\substack{ionization/\\excitation}} e^-_{aq}, H\cdot, HO\cdot, HO_2\cdot, OH^-, H_3O^+, H_2, O_2, H_2O_2$$

Equilibrium is quickly reached between these species and has been simulated for parallel-illumination TEM geometry. [204] To convert from the calibrated TEM flux [192] to the energy deposited, the stopping power of the specimen is required. This acidifies pure water but with a properly formulated solution, this approach enables direct nanoscale observation of systems of biological, environmental, and technological significance. If calibrated, the electron beam can be an electrochemical stimulus to study relevant oxidation-reduction systems.[65], [197], [199]–[203]

With an acidic pH in the TEM liquid cell, dissolution of iron oxide nanoparticles is thermodynamically favorable except when other species, namely surface functionalization, alter the solution chemistry. Electron irradiation produces reactive species, namely H^+ and aqueous electrons, in solution as a function of dose.[199], [204] Simulations have predicted that this will have the overall effect of reducing the pH of the system, as shown in Figure 5.7. [204]

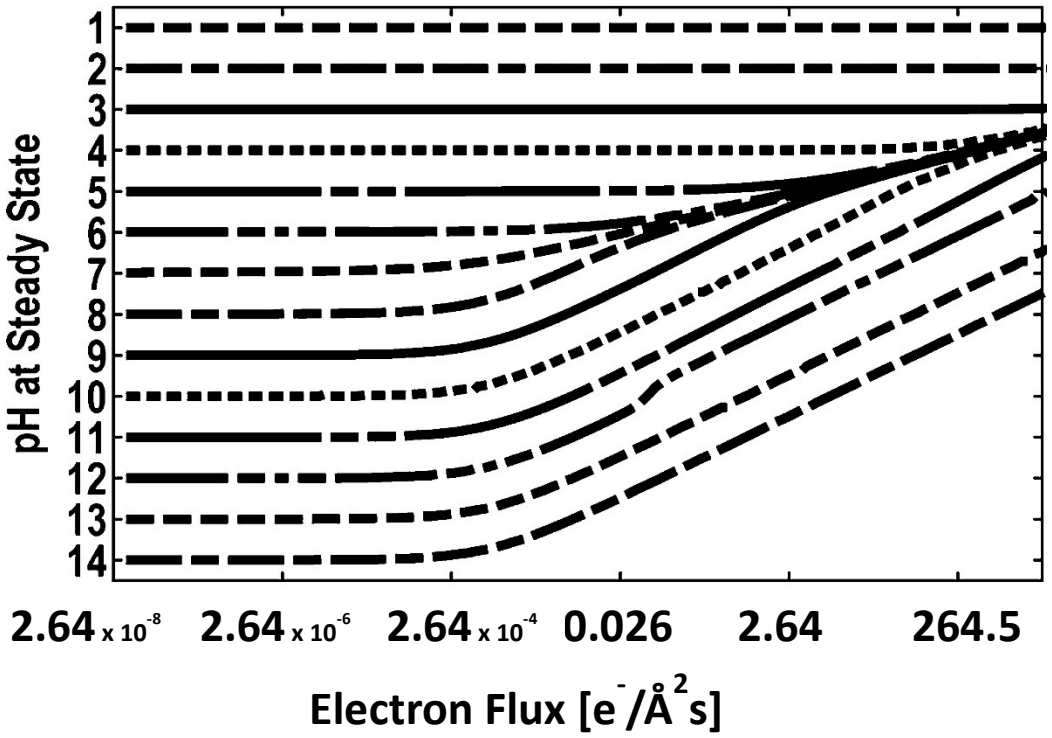

Figure 5.7. The steady state pH as a function of electron flux, starting from initial pH along left axis. Figure modified from [204], converted to electron flux using 1 e/Å^{2}s = 3,780,720 Gy/s and a density stopping power of 2.360 Mev cm2/g for 300 keV electrons in water, from NIST ESTAR database. [212]

I used this code to calculate pH for the doses used in these STEM experiments, however these simulations assume uniform illumination over the beam area, as is the case in TEM mode. This will not apply in STEM mode where a focused probe is rastered across the sample, so dose

delivery is non-uniform. That is, the irradiation is delivered locally to a ~1 Å spot that periodically (once per frame) moves across the sample. Local delivery of radiation would need to be considered as well as the diffusion of reactive species during the imaging time. Future work remains to simulate the effect of STEM imaging on liquids to improve interpretation of *in situ* experiments. But for the time being, the approach presented in [204] provides an approximation of *in situ* pH. For the electron fluxes used in these experiments, water with initial pH 7.0 acidifies to between pH 5.1 at 0.8 e^{-} $Å^{-2}$ s^{-1} and pH 4.5 at 25 e^{-} $Å^{-2}$ s^{-1}.

5.4.2 *Nanoparticle Surface Coatings*

To understand the effect of surface chemistry on colloidal stability, Fe_3O_4 nanoparticles with three different surface coatings[10] are prepared for *in-situ* imaging. Fe_3O_4 nanoparticles with hydrophobic capping ligands, synthesized in organic solvents, are coated with an amphiphilic polymer to stabilize in aqueous solutions.[37], [30], [106] Here we use a (PMAO-PEG) for aqueous phase transfer. PEG is generally biocompatible, and offers many options for functionalization. First, methoxy terminated PEG coated (Methoxy-PEG) nanoparticles are used to establish the behavior of uniform iron oxide nanoparticles in water under electron irradiation in the TEM. Then, particles functionalized with the amino acid L-cysteine (L-cys-PEG) and an arginine-rich cell penetrating peptide (CPP-PEG) are characterized to investigate the role of surface chemistry on interactions in solution, Figure 5.8 shows a schematic of nanoparticle surface coatings.

[10] These nanoparticles were synthesized and coated by my colleague, Eric Teeman. [35]

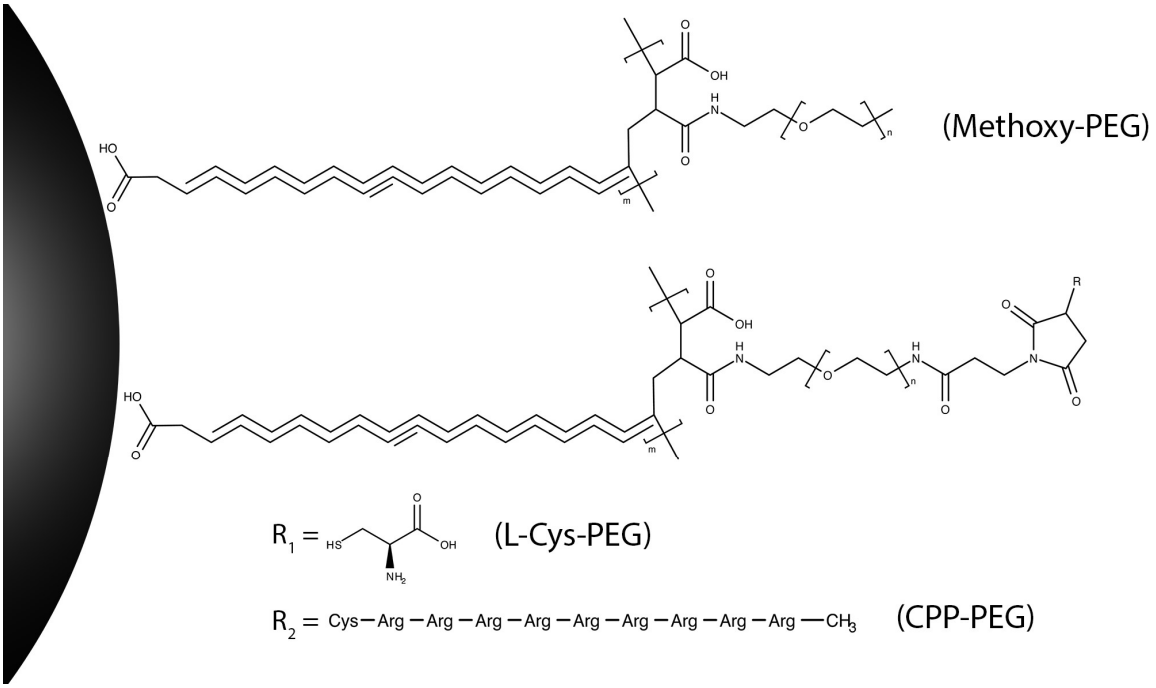

Figure 5.8. Schematic of the nanoparticle coating. Monodisperse superparamagnetic iron oxide nanoparticle cores with diameter, d_C, are coated with PMAO-PEG increasing the hydrodynamic size, d_H. PEG terminated nanoparticles may be functionalized, L-cysteine shown, which changes surface properties such as the zeta potential, ζ. Adapted from [35].

Average core diameter (d_C) and lognormal size distribution (σ) are fit to Vibrating Sample Magnetometry (VSM) measurements,[47] and confirmed with TEM. For these optimized nanoparticles, their physical size (TEM) matches within 2 % their magnetic size (VSM). The zeta potential (ζ) and hydrodynamic size (d_H) are measured by Dynamic Light Scattering (DLS) for the three different surface coatings at room temperature in DI water. These physio-chemical properties are summarized in Table 5.3.

Table 5.3. Physio-chemical properties of the iron oxide nanoparticle samples. Core diameter (d_C) and log-normal size distribution, σ, are fit to VSM data and confirmed with TEM (n = 5216 particles). Hydrodynamic diameter (d_H) and zeta potential (ζ) are measured by DLS in DI water. STEM stability summarizes the critical electron flux values that changed colloidal stability in these experiments.

d_C [nm]	σ log-normal		d_H [nm]	ζ [mV]	Liquid STEM Stability
27.2 (VSM) 27.7 (TEM)	0.15 (VSM) 0.06 (TEM)	*Fe_3O_4@ Methoxy-PEG*	90	-7	Stable < 0.8 e^- $Å^{-2}$ s^1 Dissolves ≥ 0.8 e^- $Å^{-2}$ s^{-1}
		Fe_3O_4@ CPP-PEG	77	23	Stable < 1.3 e^- $Å^{-2}$ s^1 Growth ≥ 1.3 e^- $Å^{-2}$ s^1 Dissolves ≥ 14 e^- $Å^{-2}$ s^{-1}
		Fe_3O_4@ L-Cys-PEG	70	-40	Stable < 1 e^- $Å^{-2}$ s^1 Growth ≥ 5.2 e^- $Å^{-2}$ s^{-1} After 1st cycle: Dissolves ≥ 1.8 e^- $Å^{-2}$ s^{-1}

Previous works have measured the pH dependence of the zeta potential for magnetite nanoparticles functionalized with chitosan [173] or peptide dendrimers. [174] The pH behavior of functionalized magnetite nanoparticles is similar to most colloidal systems: ζ is negative and stabilized at basic pH, and as pH is decreased ζ passes through the isoelectric point before approaching a positive ζ at acidic pH. As the solution becomes more acidic, the zeta potential increases and positive ions, including iron 2+/3+, are driven out of the primary particle where depending on the local chemistry ions may either occupy the nanoparticle Stern layer or diffuse into solution. Increasing the local iron concentration increases stability of solid iron oxide phases, see Figure 1.4, and may produce supersaturation, prompting growth of iron oxide phases.

5.4.3 *In situ* Dissolution of PEG Coated SPIONs

Methoxy-PEG coated Fe_3O_4 nanoparticles dissolve with time and dose when observed in a liquid cell in the TEM, as shown in Figure 5.9. The dissolution is dependent on the electron flux

density, with particle size (diameter) decreasing with accumulated dose (Figure 5.9d). Increasing the magnification (and thus the flux density) increases the rate of dissolution from 0.02 nm/s at 0.8 $e^- Å^{-2} s^{-1}$ to 0.10 nm/s at 6.6 $e^- Å^{-2} s^{-1}$ to 0.19 nm/s at 25 $e^- Å^{-2} s^{-1}$. Curiously, the diameter appears to decrease linearly with time. If the dissolution rate were limited by the surface reaction an r^2 surface area dependence is expected, so this reaction must be diffusion limited either in the availability of reactive ions or in the transport of iron. For Methoxy-PEG coated Fe_3O_4, we do not observe a threshold dose below which particles are stable. Even under relatively low dose conditions (< 1 $e^- Å^{-2} s^{-1}$), observable dissolution occurs within hundreds of seconds.

5.4.4 *Controlling Stability with Surface Chemistry*

To observe the effect of the surface chemistry on stability, we next observe the PMAO-PEG coated particles functionalized with the amino acid L-cysteine. Cysteine is zwitterionic, with both positive and negative charge. L-cys-PEG particles grow when exposed to sufficient electron flux density (here > 5 $e^- Å^{-2} s^{-1}$), as iron is driven from the initial particle into the surface coating**.** When the flux density is reduced back to 1 $e^- Å^{-2} s^{-1}$, by decreasing the magnification, the surface layer dissolves. This reversible growth is shown in the time series in Figure 5.10. In this experiment, one particle was imaged at high magnification and irradiated with sufficient electron flux to promote dissolution and recrystallization. Growth occurs immediately outside of the particle within the polymer layer (not visible in STEM) that extends an additional ~30 nm from the particle surface. Even after three cycles of growth and dissolution we still see a gap around the initial particle, indicating that the thickness of the polymer coating has not been permanently changed. However, the growth kinetics do appear to change between cycles: for the first cycle, the iron oxide interface moves at approximately 0.2 nm/s, while growth during second and third cycle increases to 0.4 nm/s. It is likely that not all of the iron is able to diffuse out of the coating and

back into the crystal in the time allowed for recovery, increasing recrystallization kinetics on subsequent runs.

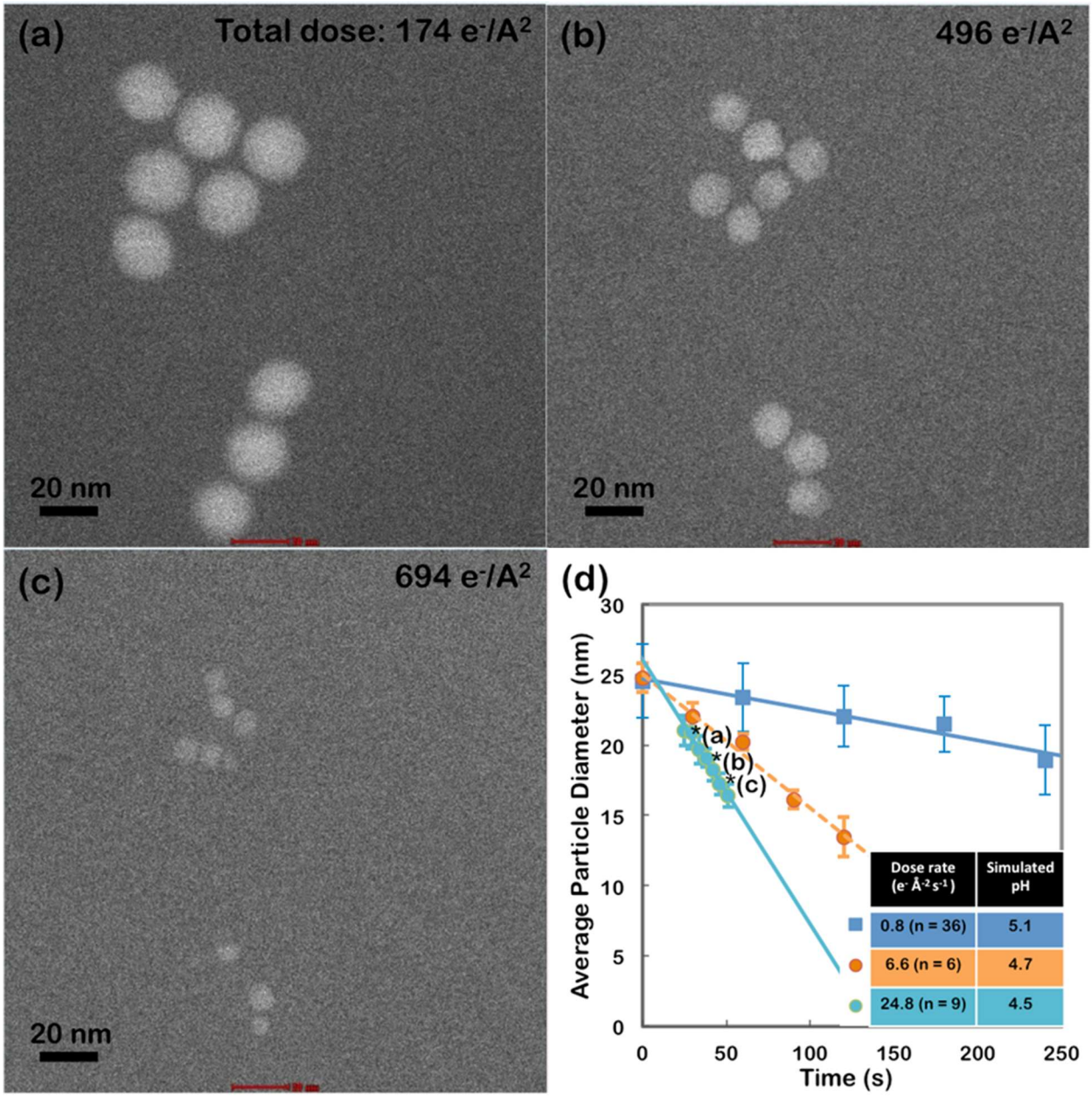

Figure 5.9. Magnetite nanoparticles terminated with PEG dissolve in water during electron irradiation. This is dependent on total dose. **(a)-(c)** are movie frames (total electron dose noted) throughout dissolution at 25 $e^{-}Å^{-2}\,s^{-1}$, **(d)** plot showing decrease in average particle size versus accumulated electron dose. The steady state pH is estimated for a thin film of water, starting at pH 7 and subjected to the respective electron flux density, using published code. [204]

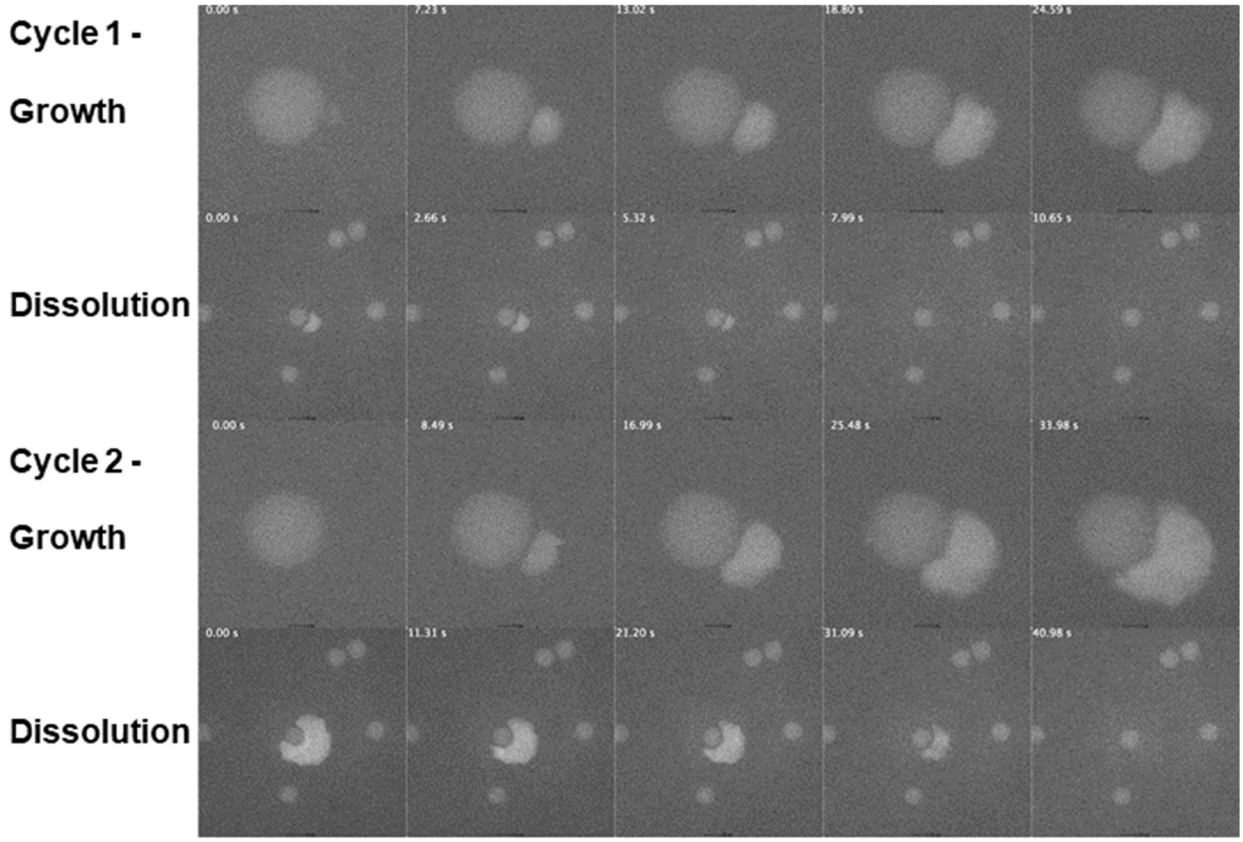

Figure 5.10. Growth at the surface of L-cysteine functionalized nanoparticle is reversed by reducing magnification and electron flux density. At higher magnification and electron flux density, here 5.2 $e^{-}Å^{-2}\,s^{-1}$, ions accumulate at the particle surface forming an amorphous iron-rich phase. When the flux density is reduced to 1.8 $e^{-}\,Å^{-2}\,s^{-1}$ by reducing the STEM magnification, iron flows back into the primary particle.

Imaging contrast in high-angle annular dark field (HAADF) STEM is proportional to atomic number; [60] in this system, iron is significantly heavier and scatters more strongly than any of the other elemental constituents. Accumulation of iron at the particle surface appears as increased contrast in the images. In this way we can quantify particle growth by radially integrating the intensity measured from the HAADF detector, as shown in Figure 5.11.

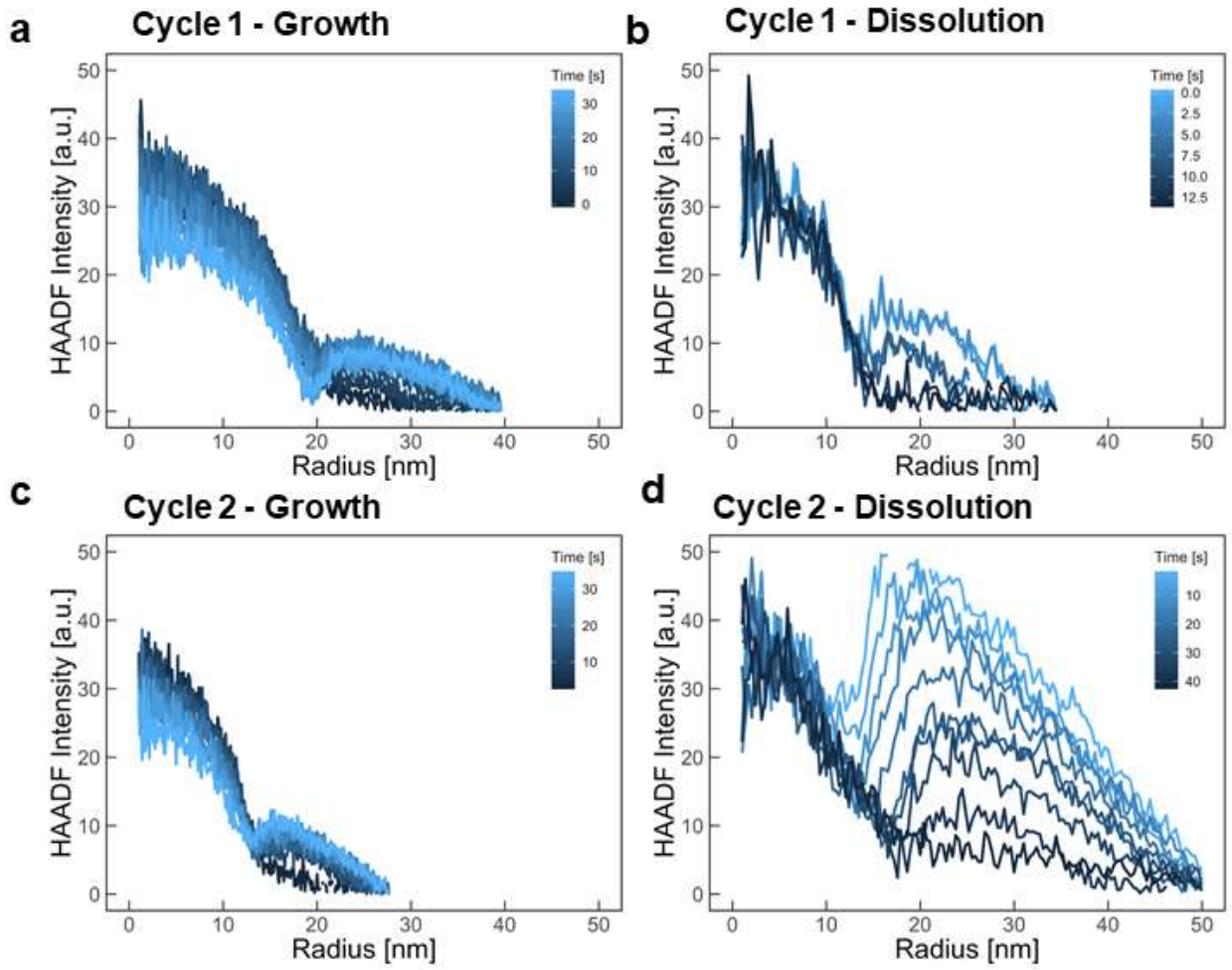

Figure 5.11. The radially integrated HAADF intensity is shown for the second cycle. From this, the average velocity of the interface is measured to be 0.4 nm/s for the growth, and -0.2 nm/s for the dissolution.

5.4.5 *STEM Induced Growth*

Unlike the reaction facilitated by L-cys-PEG, growth of CPP-PEG functionalized Fe3O4 nanoparticles is not reversible. When these particles are imaged in the TEM liquid cell, at low doses (electron flux density <1 e– Å–2 s–1) we do not observe any growth. At a flux density of 1.3 e– Å–2 s–1, the particles grow in size as iron diffuses out of primary particles, shown for an ensemble of nanoparticles in Figure 5.12. The charged peptides act as nucleation sites for a secondary iron phase. No growth species, i.e. iron, are added to solution so iron that precipitates

during the imaging is from previously dissolved particles in solution. This dissolution and subsequent growth was reproduced in multiple experiments. When the CPP-PEG particles were left to sit with the beam off for 20 minutes, they recrystallized, forming a disordered hydrated iron oxide phase, shown in Figure 5.13c. When flux density is increased to 14.1 e^{-} $Å^{-2}$ s^{-1}, these CPP-PEG particles dissolve. We expect iron oxide nanoparticles in aqueous environments will typically dissolve under moderate TEM doses of 10-100 e^{-} $Å^{-2}$ s^{-1}, regardless of the capping layer.

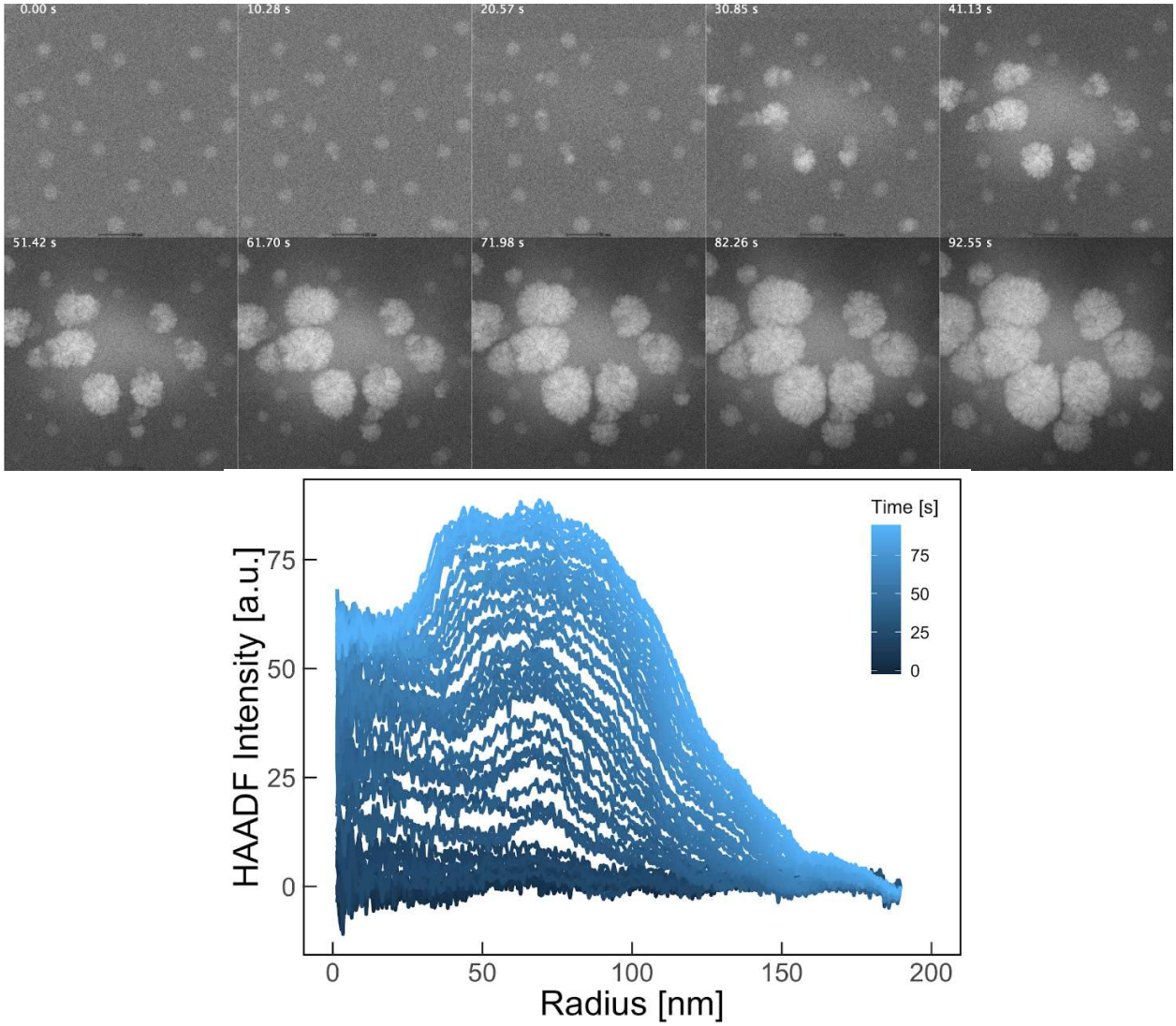

Figure 5.12. Iron oxide nanoparticle coated with poly-cationic peptides (CPP-PEG) dissolve, then re-nucleate as hydrated iron oxides in solution. Growth is quantified by measuring the integrated intensity on the HAADF detector.

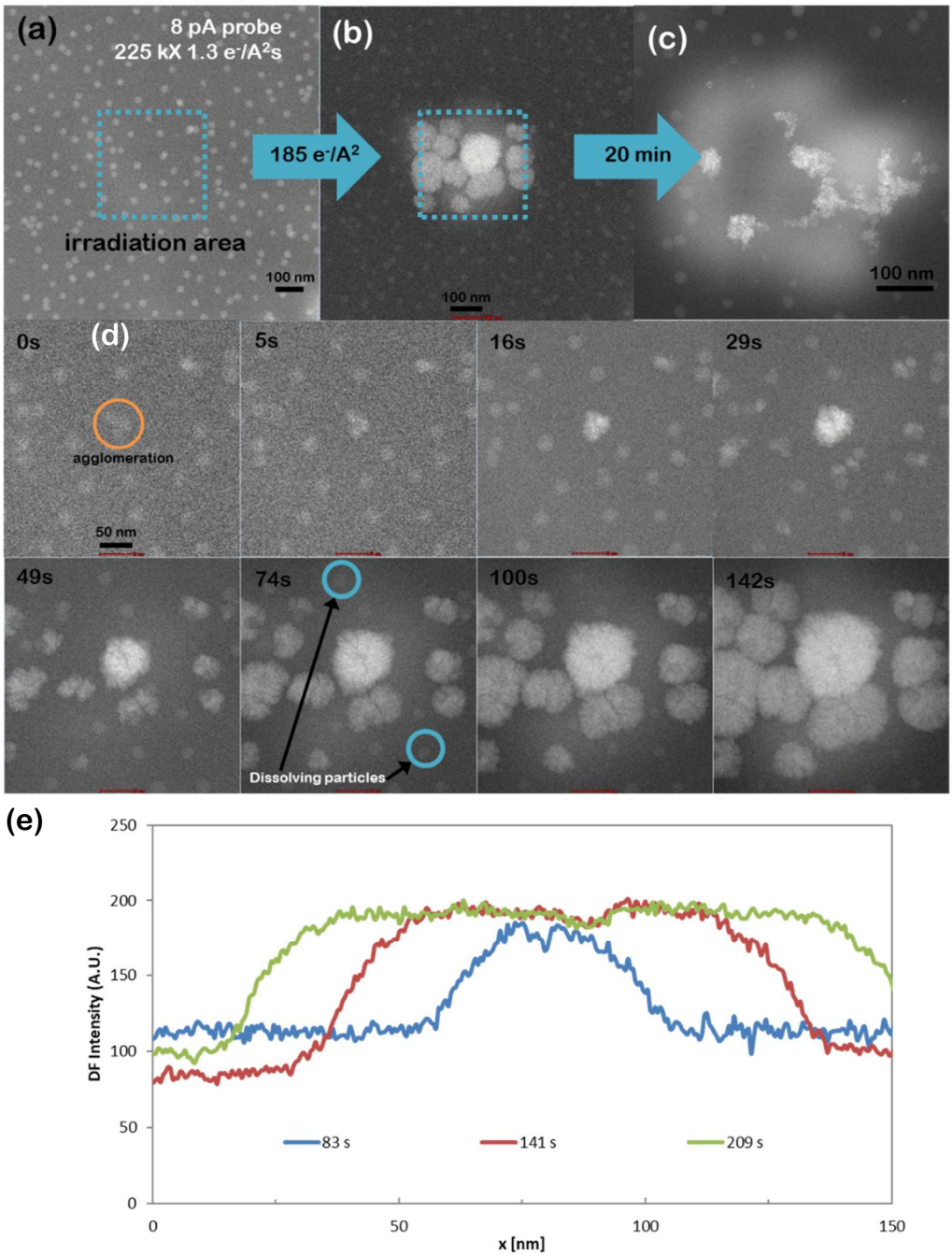

Figure 5.13. For this ensemble of CPP-PEG coated nanoparticles, iron growth at the particle surface follows dissolution of the primary Fe_3O_4 nanoparticles **(b**, and time series**)**. Some of the particles grow while others dissolve (circled in time series). When the beam is removed, densification and recrystallization as a disordered, hydrated iron phase occurs over approximately 20 minutes **(c)**. The growth of a three-particle aggregate, circled in **d**, is shown in the integrated HAADF intensity in plot **e**.

Post-mortem EDS and EELS analyses in Figure 5.14 and Figure 5.15 confirm the presence of iron in the secondary phases grown *in situ*.

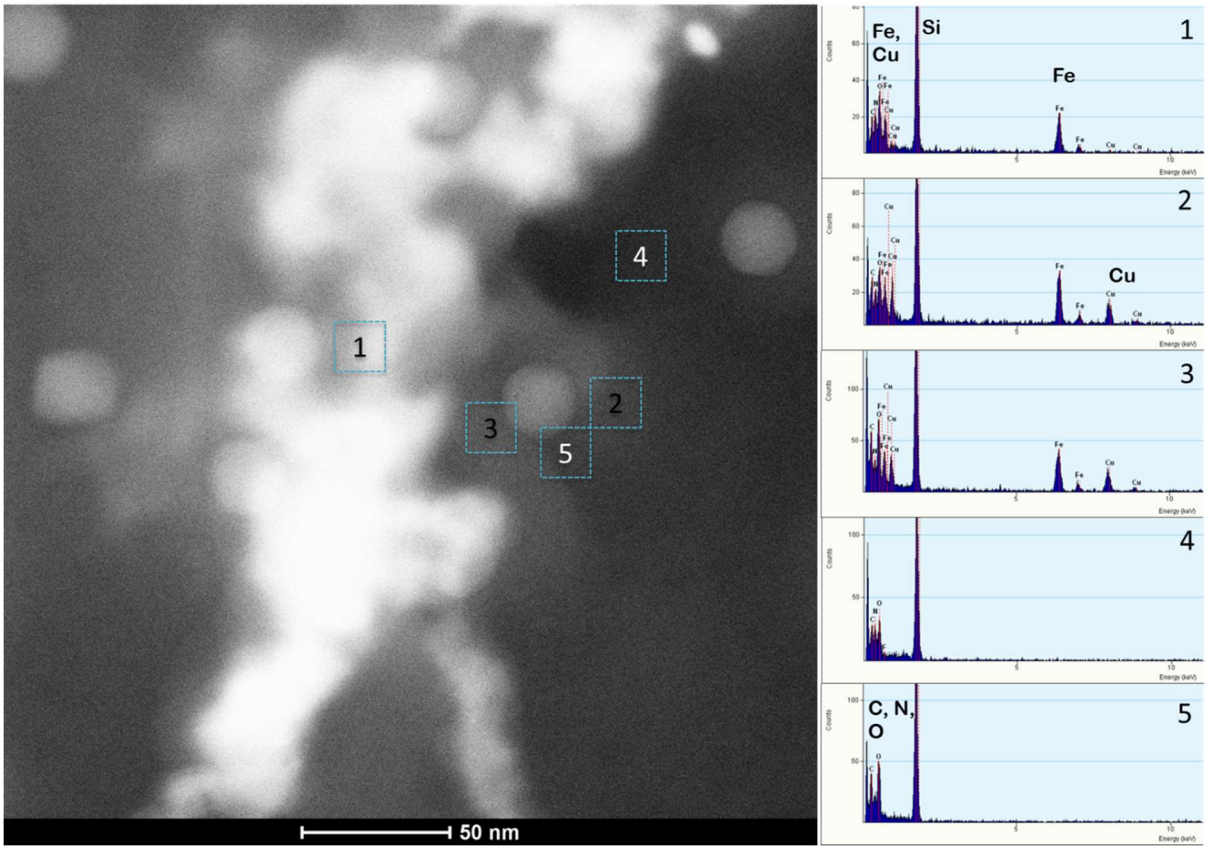

Figure 5.14. Post-mortem Energy-Dispersive Spectroscopy (EDS) confirms presence of iron in the nanoparticles (region 2) as well as the high contrast amorphous phase grown *in situ* (regions 1, 3). No iron was detected in the background (regions 4 and 5). Background copper peaks come from the holder and instrument, and silicon comes from the chip.

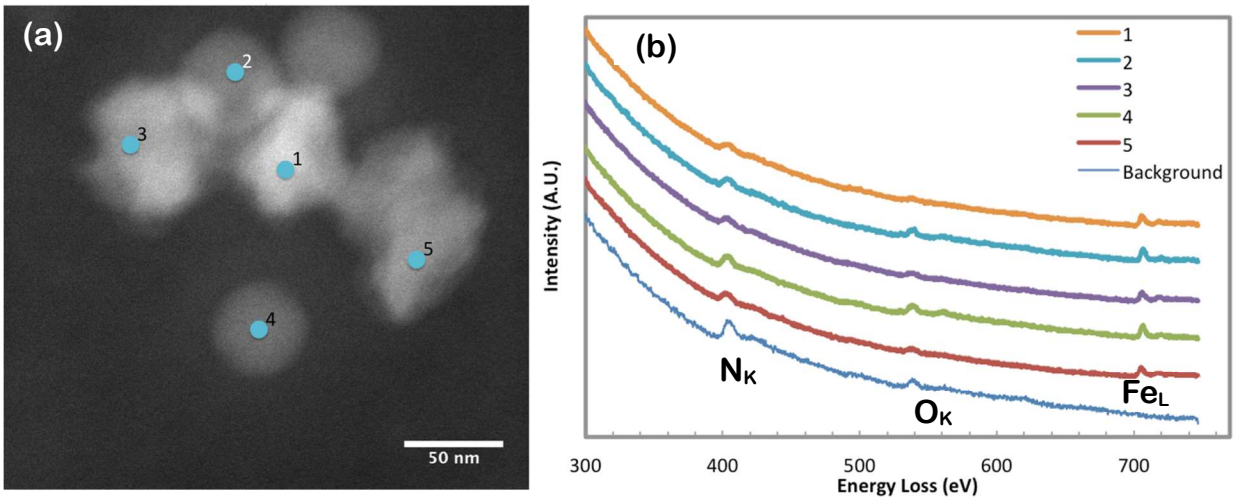

Figure 5.15. Post-mortem EELS spectra also confirm presence of iron in the particles. HAADF STEM image (**a**) indicating where spectra (**b)** where acquired. The iron L edge, onset 708 eV, is apparent both on the particles (2, 4) as well as the growths (1, 3, 5). No iron is detected in the background, captured near the cluster but not over any of the particles or growths. The nitrogen peak still present in the background is from the silicon nitride window.

5.4.6 Summary of *in situ* Nanoparticle Stability

The behavior of iron oxide nanoparticles in the TEM liquid cell depends on the surface coating. Iron ions in solution may then bind electrostatically or chemically with amino acid functional groups in the coating or recrystallize as solid hydrous iron oxide depending on local chemistry pH changes in solution. Functionalization of the Fe_3O_4 surface with L-cysteine gives reversible growth and dissolution reactions, which is specific to the local changes in pH and can be controlled with electron flux density. Metal cations, here iron, interact with amino acids altering their protonation state and in some cases forming complexes.[177], [213], [214] In particular, oxidation of cysteine by iron, and formation of iron-cysteine complexes has long been established in the case of free thiol cysteine.[215], [216] Reactivity of thioester cysteines in the coating is not necessarily the same, but we expect that iron-cysteine bonds will still form. The cysteine groups

on the functionalized nanoparticle surface serve as attachment sites for iron 2+ or 3+ ions in solution, potentially nucleating further growth. In the case of L-cys-PEG coated Fe_3O_4, *in-situ* formation of such organo-iron complexes is reversible, as shown in Figure 5.10. In contrast, the CPP-PEG coated sample contains several arginine sites where iron can bind electrostatically or chemically. With more active sites for iron to form complexes with the organic, the local iron concentration at these functional groups will be higher than the L-cysteine sample. Increasing the iron concentration stabilizes solid phases.

In all cases, the behavior of individual nanoparticles and assemblies diverge from that of bulk solution. The zeta potential, considered a primary indicator of colloidal stability, is not predictive of behavior observed in these irradiated systems. Some particles dissolve while others grow, even within the same sample. The nanoparticle stability and reversibility of growth and dissolution reactions depend on the surface functionalization and interactions with ions in solution—local phenomena that cannot be captured in the distribution of ζ in the sample. While the zeta potential of the functionalized nanoparticles is generally indicator of colloidal stability, it does not account for local variations in solution composition and pH as well as reactions between metal ions, peptides, or other species. With observable behaviors at the nanoscale differing significantly from the overall sample stability, it is clear that direct *in-situ* methods at relevant length scales must be an integral part of designing nanotechnologies that interface with biological and similarly complex systems.[160], [187]

The stability of nanoparticles in aqueous solutions is of natural significance in biomedical applications. Performance in MPI, for example, is determined by the size, size distribution, and phase of iron oxide nanoparticles.[1], [31], [37] *In vivo* behavior of nanoparticles is also highly dependent on surface chemistry.[30], [31], [165] Formulations that agglomerate in physiological

pH will lose their performance, while particles that dissolve too quickly are similarly unacceptable. Amino acid based surface modifications have enormous promise for targeting or other functionality, but may also have unexpected consequences for the behavior of the materials *in vivo*.[164]–[166] Nanoparticle surface chemistry and functionalization provide a platform to control nanoparticle interactions with solution, ions, and adjacent nanoparticles. For example, surface functionalization can be optimized for nanoparticle *in vivo* circulation time, or to tune dissolution kinetics in biological environments.[30], [178] Behavior of peptide functionalized iron oxide nanoparticles may model compounds in natural and biological systems including the interplay between proteins such as hemoglobin or ferritin and iron oxidation, metabolism, and clearance. [78], [205], [214], [215] *In situ* approaches enable direct nanoscale visualization at the solid-liquid interface to observe and quantify nanoscale kinetics. We expect the approaches we have described here will provide a starting point to evaluate a wide variety of functional materials at relevant length and time scales in hydrated environments.

Chapter 6. CONCLUDING REMARKS

In this work I have addressed several questions regarding the kinetics of nucleation, growth, synthesis, and colloidal stability of iron oxide nanoparticles. Using state-of-the-art TEM techniques, I have imaged and characterized the structure and chemistry of iron oxide nanoparticles with the highest level of detail available.

Beginning with the synthesis, the iron oleate precursor was characterized thermally to show its sequential breakdown. The ligands de-coordinate at well-defined temperatures, releasing free iron into solution in agreement with other works and DFT simulations. [107], [108] Iron oleate can be used as a precursor for synthesis of IONPs or as we suggest, forms as a reaction intermediate in other solvo-thermal syntheses. Next, as-synthesized particles were imaged and their Fe-valence was quantified by EELS and confirmed with Mossbauer spectroscopy. Prevalence of wüstite in the particles' cores suggests that they formed under-oxidized, then transformed to magnetite during aging, oxidizing from the surface in. At some point during synthesis, iron(III) was reduced to form mixed valence magnetite. Because wüstite (Fe[II]O) is often formed in the early stages of synthesis, reduction might be complete followed by oxidation at a later stage.

As these nanoparticles have non-equilibrium structures and phases, kinetics are inherent in their formation; we rely on *in situ* experiments to visualize their dynamics. By using specialized holders, we can introduce liquid samples into the TEM column. Using these techniques, a variety of colloidal phenomena are observed including nucleation, growth, aggregation, and dissolution. The energy deposited by the beam can be used as an electrochemical stimulus. TEM dose was used to electrolytically decompose iron(III) oleate, our SPION precursor, and bright field TEM movies were recorded of the precursor decomposition. The initially uniform liquid precursor separated into regions of dark and bright contrast—denser, iron-rich and iron deficient regions,

respectively. The kinetics of the separation were dose dependent, speeding up with larger dose rates. These particles were relatively large, up to 50 nm or more, and appeared amorphous. With extensive aging, as is performed *ex situ,* nanoparticles would likely crystalize.

In the thermolytic decomposition, magnetic size was initially very small (< 10 nm), growing over several hours following nucleation. Considering the TEM results it is possible that nanoparticles formed quickly via this phase separation into amorphous iron-rich particles, followed by a slow ageing and ordering into superparamagnetic particles. Although the electrochemical stimulus of the electron beam was not directly comparable to thermal energy, this remains a useful tool to enable direct visualization of nanoparticles kinetics.

In aqueous solutions, the electron beam produces reactive species in said solution, namely H+. I have shown how this can be used experimentally to study aqueous dissolution of iron oxide nanoparticles by measuring dissolution rates from the contrast in HAADF STEM. I further propose the reactive chemistry in the TEM liquid cell may be used to easily simulate acidic, reactive environments, specifically acidic biological environments. Particularly for this quantitative electrochemistry and in general for all TEM experiments, calibration and monitoring of dose rate, total dose, and relevant damage thresholds is critical. Furthermore, to minimize the effect of the electron beam, solution chemistry must be properly formulated to buffer at a particular pH, or alternately electron scavengers such as nitrates could be added to solution. Additional *in situ* stimuli remain to be investigated including the effect of an applied magnetic field or heating on the synthesis reaction and the stability of nanoparticles. As *in situ* experiments move away from electron beam induced reactions toward investigation of these other stimuli, reducing dose and minimizing damage will be especially important. Beyond the strategies previously discussed,

advances in compressive sensing and sparse sampling techniques have the potential to reproduce high-resolution images at a fraction of the dose. [217]

The techniques developed for these experiments have implications that go beyond the iron-containing systems we have studied. Materials processes in the liquid phase underlie industrial, biological, and geophysical systems, and influence energy production as well as global ecology and climate. In principle, combined with the structural and chemical sensitivity of TEM, we can use *in situ* methodologies to observe materials throughout chemical reactions, phase transformations, and many other materials processes. Much work remains to achieve this vision, and proper interpretation of these increasingly complex *in situ* systems will require development of kinetic models to predict electrochemistry in a wider variety of solutions. [218]

BIBLIOGRAPHY

[1] K. M. Krishnan, "Biomedical Nanomagnetics: A Spin Through Possibilities in Imaging, Diagnostics, and Therapy," *IEEE Trans. Magn.*, vol. 46, no. 7, pp. 2523–2558, Jul. 2010.

[2] H. Arami, R. M. Ferguson, A. P. Khandhar, and K. M. Krishnan, "Size-dependent ferrohydrodynamic relaxometry of magnetic particle imaging tracers in different environments," *Med. Phys.*, vol. 40, no. 7, p. 071904, 2013.

[3] R. M. Cornell and U. Schwertmann, *The iron oxides: structure, properties, reactions, occurrences, and uses*, 2nd, completely rev. and extended ed ed. Weinheim: Wiley-VCH, 2003.

[4] B. Gleich and J. Weizenecker, "Tomographic imaging using the nonlinear response of magnetic particles," *Nature*, vol. 435, no. 7046, pp. 1214–1217, Jun. 2005.

[5] O. N. Shebanova and P. Lazor, "Raman study of magnetite (Fe3O4): laser-induced thermal effects and oxidation," *J. Raman Spectrosc.*, vol. 34, no. 11, pp. 845–852, Nov. 2003.

[6] M. Hanesch, "Raman spectroscopy of iron oxides and (oxy)hydroxides at low laser power and possible applications in environmental magnetic studies," *Geophys. J. Int.*, vol. 177, no. 3, pp. 941–948, Jun. 2009.

[7] M. Pourbaix, *Atlas of electrochemical equilibria in aqueous solutions*, 2nd edition. Houston, TX: National Association of Corrosion Engineers (NACE), 1974.

[8] M. Faraday, "The Bakerian Lecture: Experimental Relations of Gold (and Other Metals) to Light," *Philos. Trans. R. Soc. Lond.*, vol. 147, no. 0, pp. 145–181, Jan. 1857.

[9] G. J. Higby, "Gold in medicine," *Gold Bull.*, vol. 15, no. 4, pp. 130–140, 1982.

[10] J. Turkevich, P. C. Stevenson, and J. Hillier, "A study of the nucleation and growth processes in the synthesis of colloidal gold," *Discuss. Faraday Soc.*, vol. 11, pp. 55–75, 1951.

[11] H. Perez, J.-P. Pradeau, P.-A. Albouy, and J. Perez-Omil, "Synthesis and Characterization of Functionalized Platinum Nanoparticles," *Chem. Mater.*, vol. 11, no. 12, pp. 3460–3463, Dec. 1999.

[12] V. F. Puntes, K. M. Krishnan, and A. P. Alivisatos, "Colloidal nanocrystal shape and size control: the case of cobalt," *Science*, vol. 291, no. 5511, pp. 2115–2117, 2001.

[13] D. Ma, J. Zhao, Y. Zhao, X. Hao, L. Li, L. Zhang, Y. Lu, and C. Yu, "Synthesis of bismuth nanoparticles and self-assembled nanobelts by a simple aqueous route in basic solution," *Colloids Surf. Physicochem. Eng. Asp.*, vol. 395, pp. 276–283, Feb. 2012.

[14] Z. G. Wu, M. Munoz, and O. Montero, "The synthesis of nickel nanoparticles by hydrazine reduction," *Adv. Powder Technol.*, vol. 21, no. 2, pp. 165–168, Mar. 2010.

[15] R. G. Patharkar, S. U. Nandanwar, and M. Chakraborty, "Synthesis of Colloidal Ruthenium Nanocatalyst by Chemical Reduction Method," *J. Chem.*, vol. 2013, pp. 1–5, 2013.

[16] J. Ge, Y. Hu, M. Biasini, W. P. Beyermann, and Y. Yin, "Superparamagnetic Magnetite Colloidal Nanocrystal Clusters," *Angew. Chem. Int. Ed.*, vol. 46, no. 23, pp. 4342–4345, Jun. 2007.

[17] J. Baumgartner, A. Dey, P. H. H. Bomans, C. Le Coadou, P. Fratzl, N. A. J. M. Sommerdijk, and D. Faivre, "Nucleation and growth of magnetite from solution," *Nat. Mater.*, vol. 12, no. 4, pp. 310–314, Feb. 2013.

[18] T. Hyeon, S. S. Lee, J. Park, Y. Chung, and H. B. Na, "Synthesis of Highly Crystalline and Monodisperse Maghemite Nanocrystallites without a Size-Selection Process," *J. Am. Chem. Soc.*, vol. 123, no. 51, pp. 12798–12801, Dec. 2001.
[19] J. Park, K. An, Y. Hwang, J.-G. Park, H.-J. Noh, J.-Y. Kim, J.-H. Park, N.-M. Hwang, and T. Hyeon, "Ultra-large-scale syntheses of monodisperse nanocrystals," *Nat. Mater.*, vol. 3, no. 12, pp. 891–895, Nov. 2004.
[20] S. Sun, H. Zeng, D. B. Robinson, S. Raoux, P. M. Rice, S. X. Wang, and G. Li, "Monodisperse MFe2O4 (M = Fe, Co, Mn) Nanoparticles," *J. Am. Chem. Soc.*, vol. 126, no. 1, pp. 273–279, Jan. 2004.
[21] S. Sun and H. Zeng, "Size-Controlled Synthesis of Magnetite Nanoparticles," *J. Am. Chem. Soc.*, vol. 124, no. 28, pp. 8204–8205, Jul. 2002.
[22] K. M. Krishnan, "Chapter 12: Magnetic Materials in Medicine and Biology," in *Fundamentals and Applications of Magnetic Materials*, Oxford University Press, Oxford, United Kingdom, 2016.
[23] M. Gonzales, "Synthesis, modeling and optimization of iron oxide nanoparticles for magnetic fluid hyperthermia," Ph.D. Thesis, University of Washington, 2007.
[24] M. Gonzales and K. M. Krishnan, "Synthesis of magnetoliposomes with monodisperse iron oxide nanocrystal cores for hyperthermia," *J. Magn. Magn. Mater.*, vol. 293, no. 1, pp. 265–270, May 2005.
[25] M. Gonzales and K. M. Krishnan, "Phase transfer of highly monodisperse iron oxide nanocrystals with Pluronic F127 for biomedical applications," *J. Magn. Magn. Mater.*, vol. 311, no. 1, pp. 59–62, Apr. 2007.
[26] R. M. Ferguson, K. R. Minard, and K. M. Krishnan, "Optimization of nanoparticle core size for magnetic particle imaging," *J. Magn. Magn. Mater.*, vol. 321, no. 10, pp. 1548–1551, May 2009.
[27] R. M. Ferguson, A. P. Khandhar, and K. M. Krishnan, "Tracer design for magnetic particle imaging," *J. Appl. Phys.*, vol. 111, no. 7, p. 07B318, 2012.
[28] R. M. Ferguson, "Tracer design for Magnetic Particle Imaging: modeling, synthesis, and experimental optimization of biocompatible iron oxide nanoparticles," University of Washington, 2011.
[29] A. P. Khandhar, "Biomedical imaging and therapy with physically and physiologically tailored magnetic nanoparticles," University of Washington, 2013.
[30] A. P. Khandhar, R. M. Ferguson, H. Arami, S. J. Kemp, and K. M. Krishnan, "Tuning surface coatings of optimized magnetite nanoparticle tracers for in vivo Magnetic Particle Imaging," *IEEE Trans. Magn.*, vol. 51, no. 5300304.
[31] H. Arami, A. P. Khandhar, A. Tomitaka, E. Yu, P. W. Goodwill, S. M. Conolly, and K. M. Krishnan, "In vivo multimodal magnetic particle imaging (MPI) with tailored magneto/optical contrast agents," *Biomaterials*, vol. 52, pp. 251–261, Jun. 2015.
[32] H. Arami, A. Khandhar, D. Liggitt, and K. M. Krishnan, "In vivo delivery, pharmacokinetics, biodistribution and toxicity of iron oxide nanoparticles," *Chem Soc Rev*, vol. 44, no. 23, pp. 8576–8607, 2015.
[33] H. Arami, "Magnetic Particle Imaging (MPI) Tracers for In Vivo Applications," Ph.D. Thesis, University of Washington, 2015.
[34] E. Teeman, C. Shasha, J. E. Evans, and K. M. Krishnan, "Intracellular dynamics of superparamagnetic iron oxide nanoparticles for magnetic particle imaging," *Nanoscale*, vol. 11, no. 16, pp. 7771–7780, 2019.

[35] E. Teeman, “Intracellular Dynamics of Superparamagnetic Iron Oxide Nanoparticles for Magnetic Particle Imaging,” Ph.D. Thesis, University of Washington, 2019.
[36] C. Shasha, “Nonequilibrium Nanoparticle Dyanamics for the Development of Magnetic Particle Imaging,” Ph.D. Thesis, University of Washington, 2019.
[37] R. Hufschmid, H. Arami, R. M. Ferguson, M. Gonzales, E. Teeman, L. N. Brush, N. D. Browning, and K. M. Krishnan, “Synthesis of phase-pure and monodisperse iron oxide nanoparticles by thermal decomposition,” *Nanoscale*, vol. 7, no. 25, pp. 11142–11154, 2015.
[38] R. Hufschmid, H. Arami, K. M. Krishnan, and N. D. Browning, “Ex Situ and In Situ (S)TEM of Iron Oxide Nanoparticles Synthesized by Decomposition of an Organometallic Precursor,” *Microsc. Microanal.*, vol. 21, no. Supplement S3, pp. 965–966, 2015.
[39] R. Hufschmid, E. Teeman, H. Arami, M. Gonzales, H. Bradshaw, A. Troksa, N. D. Browning, and K. M. Krishnan, “Phase-pure iron oxide nanoparticle MPI tracers: Comparison of alternative thermal decomposition synthesis strategies,” in *Magnetic Particle Imaging (IWMPI), 2015 5th International Workshop on*, 2015, pp. 1–1.
[40] R. Hufschmid, R. M. Ferguson, E. Teeman, K. M. Krishnan, and N. D. Browning, “Atomic Resolution and in situ STEM-EELS of Superparamagnetic Iron Oxide Nanoparticles,” *Microsc. Microanal.*, vol. 22, no. S3, pp. 1714–1715, 2016.
[41] O. Sadeghi, C. Falaise, P. I. Molina, R. Hufschmid, C. F. Campana, B. C. Noll, N. D. Browning, and M. Nyman, “Chemical Stabilization and Electrochemical Destabilization of the Iron Keggin Ion in Water,” *Inorg. Chem.*, Oct. 2016.
[42] R. Hufschmid, C. J. Newcomb, J. W. Grate, J. J. De Yoreo, N. D. Browning, and N. P. Qafoku, “Direct Visualization of Aggregate Morphology and Dynamics in a Model Soil Organic-Mineral System,” *Environ. Sci. Technol. Lett.*, vol. 4, no. 5, pp. 186–191, 2017.
[43] R. Hufschmid, K. Krishnan, and N. Browning, “Probing Dynamic Phase Transformations of Hydrated Iron Oxide Nanoparticles with in situ Scanning Transmission Electron Microscopy,” *Microsc. Microanal.*, vol. 23, Jul. 2017.
[44] R. Hufschmid, J. Landers, C. Shasha, S. Salamon, H. Wende, and K. M. Krishnan, “Nanoscale Physical and Chemical Structure of Iron Oxide Nanoparticles for Magnetic Particle Imaging,” *Phys. Status Solidi A*, vol. 216, no. 2, p. 1800544, Jan. 2019.
[45] R. J. Thibeau, C. W. Brown, and R. H. Heidersbach, “Raman spectra of possible corrosion products of iron,” *Appl. Spectrosc.*, vol. 32, no. 6, pp. 532–535, 1978.
[46] A. P. Khandhar, R. M. Ferguson, H. Arami, and K. M. Krishnan, “Monodisperse magnetite nanoparticle tracers for in vivo magnetic particle imaging,” *Biomaterials*, vol. 34, no. 15, pp. 3837–3845, May 2013.
[47] R. W. Chantrell, J. Popplewell, and S. W. Charles, “Measurements of Particle Size Distribution Parameters in Ferrofluids,” *IEEE Trans. Mag.*, vol. MAG-14, no. 5, pp. 975–977, Sep. 1978.
[48] R. M. Ferguson, A. P. Khandhar, H. Arami, L. Hua, O. Hovorka, and K. M. Krishnan, “Tailoring the magnetic and pharmacokinetic properties of iron oxide magnetic particle imaging tracers,” *Biomed. Tech. Eng.*, vol. 58, no. 6, Jan. 2013.
[49] J. Weizenecker, B. Gleich, J. Rahmer, and J. Borgert, “Micro-magnetic simulation study on the magnetic particle imaging performance of anisotropic mono-domain particles,” *Phys. Med. Biol.*, vol. 57, no. 22, pp. 7317–7327, Nov. 2012.

[50] M. Gonzales-Weimuller, M. Zeisberger, and K. M. Krishnan, “Size-dependant heating rates of iron oxide nanoparticles for magnetic fluid hyperthermia,” *J. Magn. Magn. Mater.*, vol. 321, no. 13, pp. 1947–1950, Jul. 2009.
[51] A. P. Khandhar, R. M. Ferguson, and K. M. Krishnan, “Monodispersed magnetite nanoparticles optimized for magnetic fluid hyperthermia: Implications in biological systems,” *J. Appl. Phys.*, vol. 109, no. 7, p. 07B310, 2011.
[52] F. Ludwig, C. Kuhlmann, T. Wawrzik, J. Dieckhoff, A. Lak, A. P. Kandhar, R. M. Ferguson, S. J. Kemp, and K. M. Krishnan, “Dynamic Magnetic Properties of Optimized Magnetic Nanoparticles for Magnetic Particle Imaging,” *IEEE Trans. Magn.*, vol. 50, no. 11, pp. 1–4, Nov. 2014.
[53] F. Ludwig, H. Remmer, C. Kuhlmann, T. Wawrzik, H. Arami, R. M. Ferguson, and K. M. Krishnan, “Self-consistent magnetic properties of magnetite tracers optimized for magnetic particle imaging measured by ac susceptometry, magnetorelaxometry and magnetic particle spectroscopy,” *J. Magn. Magn. Mater.*, vol. 360, pp. 169–173, Jun. 2014.
[54] L. R. Croft, P. W. Goodwill, J. J. Konkle, H. Arami, D. A. Price, A. X. Li, E. U. Saritas, and S. M. Conolly, “Low drive field amplitude for improved image resolution in magnetic particle imaging.,” *Med. Phys.*, vol. 43, no. 1, p. 424, Jan. 2016.
[55] von E. Ruska, “Beitrag zur übermikroskopischen Abbildung bei höheren Drucken,” *Kolloid-Z.*, vol. 100, no. 2, pp. 212–219, 1942.
[56] D. B. Williams and C. B. Carter, *Transmission Electron Microscopy*, Second Edition. Springer, 2009.
[57] C. A. Schneider, W. S. Rasband, and K. W. Eliceiri, “NIH Image to ImageJ: 25 years of image analysis,” *Nat. Methods*, vol. 9, p. 671, Jun. 2012.
[58] J. Schindelin, C. T. Rueden, M. C. Hiner, and K. W. Eliceiri, “The ImageJ ecosystem: An open platform for biomedical image analysis: T HE I MAGEJ E COSYSTEM,” *Mol. Reprod. Dev.*, vol. 82, no. 7–8, pp. 518–529, Jul. 2015.
[59] J. Schindelin, I. Arganda-Carreras, E. Frise, V. Kaynig, M. Longair, T. Pietzsch, S. Preibisch, C. Rueden, S. Saalfeld, B. Schmid, J.-Y. Tinevez, D. J. White, V. Hartenstein, K. Eliceiri, P. Tomancak, and A. Cardona, “Fiji: an open-source platform for biological-image analysis,” *Nat. Methods*, vol. 9, p. 676, Jun. 2012.
[60] N. D. Browning, M. F. Chisholm, and S. J. Pennycook, “Atomic-resolution chemical analysis using a scanning transmission electron microscope,” *Nature*, vol. 366, pp. 143–146, Nov. 1993.
[61] M. Haider, S. Uhlemann, and E. Schwan, “Electron microscopy image enhanced,” *Nature*, vol. 392, pp. 768–769, Apr. 1998.
[62] H. Dömer and O. Bostanjoglo, “High-speed transmission electron microscope,” *Rev. Sci. Instrum.*, vol. 74, no. 10, p. 4369, 2003.
[63] J. M. Grogan, L. Rotkina, and H. H. Bau, “In situ liquid-cell electron microscopy of colloid aggregation and growth dynamics,” *Phys. Rev. E*, vol. 83, no. 6, Jun. 2011.
[64] J. E. Evans, K. L. Jungjohann, N. D. Browning, and I. Arslan, “Controlled Growth of Nanoparticles from Solution with In Situ Liquid Transmission Electron Microscopy,” *Nano Lett.*, vol. 11, no. 7, pp. 2809–2813, Jul. 2011.
[65] L. R. Parent, D. B. Robinson, T. J. Woehl, W. D. Ristenpart, J. E. Evans, N. D. Browning, and I. Arslan, “Direct *in Situ* Observation of Nanoparticle Synthesis in a Liquid Crystal Surfactant Template,” *ACS Nano*, vol. 6, no. 4, pp. 3589–3596, Apr. 2012.

[66] J. M. Yuk, J. Park, P. Ercius, K. Kim, D. J. Hellebusch, M. F. Crommie, J. Y. Lee, A. Zettl, and A. P. Alivisatos, "High-Resolution EM of Colloidal Nanocrystal Growth Using Graphene Liquid Cells," *Science*, vol. 336, no. 6077, pp. 61–64, Apr. 2012.

[67] T. LaGrange, M. R. Armstrong, K. Boyden, C. G. Brown, G. H. Campbell, J. D. Colvin, W. J. DeHope, A. M. Frank, D. J. Gibson, F. V. Hartemann, J. S. Kim, W. E. King, B. J. Pyke, B. W. Reed, M. D. Shirk, R. M. Shuttlesworth, B. C. Stuart, B. R. Torralva, and N. D. Browning, "Single-shot dynamic transmission electron microscopy," *Appl. Phys. Lett.*, vol. 89, no. 4, p. 044105, 2006.

[68] C. C. Ahn, *Transmission electron energy loss spectrometry in materials science and the EELS atlas*. John Wiley & Sons, 2006.

[69] O. L. Krivanek, T. C. Lovejoy, N. Dellby, T. Aoki, R. W. Carpenter, P. Rez, E. Soignard, J. Zhu, P. E. Batson, M. J. Lagos, R. F. Egerton, and P. A. Crozier, "Vibrational spectroscopy in the electron microscope," *Nature*, vol. 514, no. 7521, pp. 209–212, Oct. 2014.

[70] O. L. Krivanek, N. Dellby, J. A. Hachtel, J.-C. Idrobo, M. T. Hotz, B. Plotkin-Swing, N. J. Bacon, A. L. Bleloch, G. J. Corbin, M. V. Hoffman, C. E. Meyer, and T. C. Lovejoy, "Progress in ultrahigh energy resolution EELS," *Ultramicroscopy*, vol. 203, pp. 60–67, Aug. 2019.

[71] T. Malis, S. C. Cheng, and R. F. Egerton, "EELS log-ratio technique for specimen-thickness measurement in the TEM," *J. Electron Microsc. Tech.*, vol. 8, no. 2, pp. 193–200, 1988.

[72] R. F. Klie and N. D. Browning, "Characterization of oxygen ordering in (La, Sr)FeO3 – δ by atomic resolution Z-contrast imaging and electron energy-loss spectroscopy," *J. Electron Microsc. (Tokyo)*, vol. 51, no. suppl 1, pp. S59–S66, Mar. 2002.

[73] R. F. Egerton, "Electron energy-loss spectroscopy in the TEM," *Rep. Prog. Phys.*, vol. 72, 2009.

[74] H. Shuman and P. Kruit, "Quantitative data processing of parallel recorded electron energy-loss spectra with low signal to background," *Rev. Sci. Instrum.*, vol. 56, no. 2, pp. 231–239, Feb. 1985.

[75] H. Shuman and A. P. Somlyo, "Electron energy loss analysis of near-trace-element concentrations of calcium," *Ultramicroscopy*, vol. 21, no. 1, pp. 23–32, 1987.

[76] N. J. Zaluzec, "Digital filters for application to data analysis in electron energy-loss spectrometry," *Ultramicroscopy*, vol. 18, no. 1–4, pp. 185–190, 1985.

[77] G. A. Botton, C. C. Appel, A. Horsewell, and W. M. Stobbs, "Quantification of the EELS near-edge structures to study Mn doping in oxides," *J. Microsc.*, vol. 180, no. 3, pp. 211–216, 1995.

[78] R. al Weissleder, D. D. Stark, B. L. Engelstad, B. R. Bacon, C. C. Compton, D. L. White, P. Jacobs, and J. Lewis, "Superparamagnetic iron oxide: pharmacokinetics and toxicity," *Am. J. Roentgenol.*, vol. 152, no. 1, pp. 167–173, 1989.

[79] Y.-X. J. Wang, S. M. Hussain, and G. P. Krestin, "Superparamagnetic iron oxide contrast agents: physicochemical characteristics and applications in MR imaging," *Eur. Radiol.*, vol. 11, no. 11, pp. 2319–2331, Nov. 2001.

[80] M. Lu, M. H. Cohen, D. Rieves, and R. Pazdur, "FDA report: Ferumoxytol for intravenous iron therapy in adult patients with chronic kidney disease," *Am. J. Hematol.*, p. NA-NA, 2010.

[81] P. Reimer and T. Balzer, “Ferucarbotran (Resovist): a new clinically approved RES-specific contrast agent for contrast-enhanced MRI of the liver: properties, clinical development, and applications,” *Eur. Radiol.*, vol. 13, no. 6, pp. 1266–1276, 2003.
[82] J. P. M. Almeida, A. L. Chen, A. Foster, and R. Drezek, “In vivo biodistribution of nanoparticles,” *Nanomed.*, vol. 6, no. 5, pp. 815–835, Jul. 2011.
[83] P. W. Goodwill, E. U. Saritas, L. R. Croft, T. N. Kim, K. M. Krishnan, D. V. Schaffer, and S. M. Conolly, “X-Space MPI: Magnetic Nanoparticles for Safe Medical Imaging,” *Adv. Mater.*, vol. 24, no. 28, pp. 3870–3877, Jul. 2012.
[84] R. W. Katzberg and C. Haller, “Contrast-induced nephrotoxicity: Clinical landscape,” *Kidney Int.*, vol. 69, pp. S3–S7, Apr. 2006.
[85] J. H. Ix, N. Mercado, M. G. Shlipak, P. A. Lemos, E. Boersma, W. Lindeboom, W. W. O’Neill, W. Wijns, and P. W. Serruys, “Association of chronic kidney disease with clinical outcomes after coronary revascularization: The arterial revascularization therapies study (ARTS),” *Am. Heart J.*, vol. 149, no. 3, pp. 512–519, Mar. 2005.
[86] M. A. Bettmann, “Frequently Asked Questions: Iodinated Contrast Agents1,” *RadioGraphics*, vol. 24, no. suppl_1, pp. S3–S10, Oct. 2004.
[87] Y.-X. J. Wang, “Superparamagnetic iron oxide based MRI contrast agents: Current status of clinical application,” *Quant. Imaging Med. Surg.*, vol. 1, no. 1, pp. 35–40, Dec. 2011.
[88] D. J. Grootendorst, J. Jose, R. M. Fratila, M. Visscher, A. H. Velders, B. Ten Haken, T. G. Van Leeuwen, W. Steenbergen, S. Manohar, and T. J. M. Ruers, “Evaluation of superparamagnetic iron oxide nanoparticles (Endorem®) as a photoacoustic contrast agent for intra-operative nodal staging,” *Contrast Media Mol. Imaging*, vol. 8, no. 1, pp. 83–91, Feb. 2013.
[89] R. Ferguson, A. Khandhar, E. Saritas, L. Croft, P. Goodwill, A. Halkola, J. Borgert, J. Rahmer, S. Conolly, and K. Krishnan, “Magnetic Particle Imaging with Tailored Iron Oxide Nanoparticle Tracers,” *IEEE Trans. Med. Imaging*, pp. 1–1, 2014.
[90] R. M. Ferguson, K. R. Minard, A. P. Khandhar, and K. M. Krishnan, “Optimizing magnetite nanoparticles for mass sensitivity in magnetic particle imaging,” *Med. Phys.*, vol. 38, no. 3, p. 1619, 2011.
[91] R. M. Ferguson, A. P. Khandhar, and K. M. Krishnan, “Tracer design for magnetic particle imaging (invited),” *J. Appl. Phys.*, vol. 111, no. 7, p. 07B318, 2012.
[92] A. P. Khandhar, R. M. Ferguson, J. A. Simon, and K. M. Krishnan, “Tailored magnetic nanoparticles for optimizing magnetic fluid hyperthermia,” *J. Biomed. Mater. Res. A*, vol. 100A, no. 3, pp. 728–737, Mar. 2012.
[93] B. H. Kim, N. Lee, H. Kim, K. An, Y. I. Park, Y. Choi, K. Shin, Y. Lee, S. G. Kwon, H. B. Na, J.-G. Park, T.-Y. Ahn, Y.-W. Kim, W. K. Moon, S. H. Choi, and T. Hyeon, “Large-Scale Synthesis of Uniform and Extremely Small-Sized Iron Oxide Nanoparticles for High-Resolution T_1 Magnetic Resonance Imaging Contrast Agents,” *J. Am. Chem. Soc.*, vol. 133, no. 32, pp. 12624–12631, Aug. 2011.
[94] S. Tong, S. Hou, Z. Zheng, J. Zhou, and G. Bao, “Coating Optimization of Superparamagnetic Iron Oxide Nanoparticles for High T_2 Relaxivity,” *Nano Lett.*, vol. 10, no. 11, pp. 4607–4613, Nov. 2010.
[95] V. K. LaMer and R. H. Dinegar, “Theory, production and mechanism of formation of monodispersed hydrosols,” *J. Am. Chem. Soc.*, vol. 72, no. 11, pp. 4847–4854, 1950.
[96] M. Kahlweit, “Ostwald ripening of precipitates,” *Adv. Colloid Interface Sci.*, vol. 5, no. 1, pp. 1–35, 1975.

[97] T. Wen, L. N. Brush, and K. M. Krishnan, “A generalized diffusion model for growth of nanoparticles synthesized by colloidal methods,” *J. Colloid Interface Sci.*, vol. 419, pp. 79–85, Apr. 2014.
[98] T. Sugimoto, “Peparation of monodispersed colloidal particles,” *Adv. Colloid Interface Sci.*, vol. 28, pp. 65–108, 1987.
[99] W. W. Yu, J. C. Falkner, C. T. Yavuz, and V. L. Colvin, “Synthesis of monodisperse iron oxide nanocrystals by thermal decomposition of iron carboxylate salts,” *Chem. Commun.*, no. 20, p. 2306, 2004.
[100] S. Zhao, C. Yang, J. Yan, and J. Wang, “A novel solvethermal method for the preparation of magnetic monodisperse Fe3O4 nanoparticles II: High-surface-activity ferrihydrite used as precursor,” *Mater. Res. Bull.*, vol. 48, no. 10, pp. 4385–4389, Oct. 2013.
[101] B. Vallina, J. D. Rodriguez-Blanco, A. P. Brown, L. G. Benning, and J. A. Blanco, “Enhanced magnetic coercivity of α-Fe2O3 obtained from carbonated 2-line ferrihydrite,” *J. Nanoparticle Res.*, vol. 16, no. 3, Mar. 2014.
[102] L. M. Bronstein, X. Huang, J. Retrum, A. Schmucker, M. Pink, B. D. Stein, and B. Dragnea, “Influence of Iron Oleate Complex Structure on Iron Oxide Nanoparticle Formation,” *Chem. Mater.*, vol. 19, no. 15, pp. 3624–3632, Jul. 2007.
[103] B. P. Pichon, O. Gerber, C. Lefevre, I. Florea, S. Fleutot, W. Baaziz, M. Pauly, M. Ohlmann, C. Ulhaq, O. Ersen, V. Pierron-Bohnes, P. Panissod, M. Drillon, and S. Begin-Colin, “Microstructural and Magnetic Investigations of Wüstite-Spinel Core-Shell Cubic-Shaped Nanoparticles,” *Chem. Mater.*, vol. 23, no. 11, pp. 2886–2900, Jun. 2011.
[104] H. Arami and K. M. Krishnan, “Highly Stable Amine Functionalized Iron Oxide Nanoparticles Designed for Magnetic Particle Imaging (MPI),” *IEEE Trans. Magn.*, vol. 49, no. 7, pp. 3500–3503, Jul. 2013.
[105] M. Gonzales and K. M. Krishnan, “Phase transfer of highly monodisperse iron oxide nanocrystals with Pluronic F127 for biomedical applications,” *J. Magn. Magn. Mater.*, vol. 311, no. 1, pp. 59–62, Apr. 2007.
[106] W. W. Yu, E. Chang, C. M. Sayes, R. Drezek, and V. L. Colvin, “Aqueous dispersion of monodisperse magnetic iron oxide nanocrystals through phase transfer,” *Nanotechnology*, vol. 17, no. 17, pp. 4483–4487, Sep. 2006.
[107] A. López-Cruz and G. E. López, “Formation of an iron oxide bond in iron carboxylate complexes: a density functional theory study,” *Mol. Phys.*, vol. 107, no. 17, pp. 1799–1804, Sep. 2009.
[108] S. Palchoudhury, W. An, Y. Xu, Y. Qin, Z. Zhang, N. Chopra, R. A. Holler, C. H. Turner, and Y. Bao, “Synthesis and Growth Mechanism of Iron Oxide Nanowhiskers,” *Nano Lett.*, vol. 11, no. 3, pp. 1141–1146, Mar. 2011.
[109] S. J. Kemp, R. M. Ferguson, A. P. Khandhar, and K. M. Krishnan, “Monodisperse magnetite nanoparticles with nearly ideal saturation magnetization,” *RSC Adv*, 2016.
[110] G. Wulff, *Z. Kryst. Mineral.*, vol. 34, no. 5/6, pp. 449–530, 1901.
[111] E. Ringe, R. P. Van Duyne, and L. D. Marks, “Wulff Construction for Alloy Nanoparticles,” *Nano Lett.*, vol. 11, no. 8, pp. 3399–3403, Aug. 2011.
[112] H. T. Hai, H. Kura, M. Takahashi, and T. Ogawa, “Facile synthesis of Fe3O4 nanoparticles by reduction phase transformation from gamma-Fe2O3 nanoparticles in organic solvent,” *J. Colloid Interface Sci.*, vol. 341, no. 1, pp. 194–199, Jan. 2010.
[113] H. T. Hai, H. T. Yang, H. Kura, D. Hasegawa, Y. Ogata, M. Takahashi, and T. Ogawa, “Size control and characterization of wustite (core)/spinel (shell) nanocubes obtained by

decomposition of iron oleate complex," *J. Colloid Interface Sci.*, vol. 346, no. 1, pp. 37–42, Jun. 2010.
[114] T. W. Smith and D. Wychick, "Colloidal iron dispersions prepared via the polymer-catalyzed decomposition of iron pentacarbonyl," *J. Phys. Chem.*, vol. 84, no. 12, pp. 1621–1629, 1980.
[115] D. L. A. de Faria, S. Venâncio Silva, and M. T. de Oliveira, "Raman microspectroscopy of some iron oxides and oxyhydroxides," *J. Raman Spectrosc.*, vol. 28, no. 11, pp. 873–878, Nov. 1997.
[116] L. Cavé, T. Al, D. Loomer, S. Cogswell, and L. Weaver, "A STEM/EELS method for mapping iron valence ratios in oxide minerals," *Micron*, vol. 37, no. 4, pp. 301–309, Jun. 2006.
[117] E. Y. Yu, M. Bishop, B. Zheng, R. M. Ferguson, A. P. Khandhar, S. J. Kemp, K. M. Krishnan, P. W. Goodwill, and S. M. Conolly, "Magnetic Particle Imaging: A Novel in Vivo Imaging Platform for Cancer Detection," *Nano Lett.*, vol. 17, no. 3, pp. 1648–1654, Mar. 2017.
[118] T. Knopp and T. M. Buzug, *Magnetic Particle Imaging*. Berlin, Heidelberg: Springer Berlin Heidelberg, 2012.
[119] T. Knopp, T. F. Sattel, S. Biederer, J. Rahmer, J. Weizenecker, B. Gleich, J. Borgert, and T. M. Buzug, "Model-Based Reconstruction for Magnetic Particle Imaging," *IEEE Trans. Med. Imaging*, vol. 29, no. 1, pp. 12–18, Jan. 2010.
[120] J. Borgert, J. D. Schmidt, I. Schmale, J. Rahmer, C. Bontus, B. Gleich, B. David, R. Eckart, O. Woywode, J. Weizenecker, J. Schnorr, M. Taupitz, J. Haegele, F. M. Vogt, and J. Barkhausen, "Fundamentals and applications of magnetic particle imaging," *J. Cardiovasc. Comput. Tomogr.*, vol. 6, no. 3, pp. 149–153, May 2012.
[121] J. Weizenecker, J. Borgert, and B. Gleich, "A simulation study on the resolution and sensitivity of magnetic particle imaging," *Phys. Med. Biol.*, vol. 52, no. 21, pp. 6363–6374, Nov. 2007.
[122] T. Knopp, S. Biederer, T. F. Sattel, M. Erbe, and T. M. Buzug, "Prediction of the Spatial Resolution of Magnetic Particle Imaging Using the Modulation Transfer Function of the Imaging Process," *IEEE Trans. Med. Imaging*, vol. 30, no. 6, pp. 1284–1292, Jun. 2011.
[123] S. Jiang, A. A. Eltoukhy, K. T. Love, R. Langer, and D. G. Anderson, "Lipidoid-Coated Iron Oxide Nanoparticles for Efficient DNA and siRNA delivery," *Nano Lett.*, vol. 13, no. 3, pp. 1059–1064, Mar. 2013.
[124] D. Chen, X. Xia, H. Gu, Q. Xu, J. Ge, Y. Li, N. Li, and J. Lu, "pH-responsive polymeric carrier encapsulated magnetic nanoparticles for cancer targeted imaging and delivery," *J. Mater. Chem.*, vol. 21, no. 34, p. 12682, 2011.
[125] J. R. McCarthy, K. A. Kelly, E. Y. Sun, and R. Weissleder, "Targeted delivery of multifunctional magnetic nanoparticles," *Nanomed.*, vol. 2, no. 2, pp. 153–167, Mar. 2007.
[126] E. Duguet, S. Vasseur, S. Mornet, and J.-M. Devoisselle, "Magnetic nanoparticles and their applications in medicine," *Nanomed.*, vol. 1, no. 2, pp. 157–168, Aug. 2006.
[127] R. Weissleder, A. Moore, U. Mahmood, R. Bhorade, H. Benveniste, E. A. Chiocca, and J. P. Basilion, "In vivo magnetic resonance imaging of transgene expression," *Nat. Med.*, vol. 6, no. 3, pp. 351–354, 2000.
[128] Q. A. Pankhurst, N. T. K. Thanh, S. K. Jones, and J. Dobson, "Progress in applications of magnetic nanoparticles in biomedicine," *J. Phys. Appl. Phys.*, vol. 42, no. 22, p. 224001, Nov. 2009.

[129] S. Trabulo, A. Aires, A. Aicher, C. Heeschen, and A. L. Cortajarena, “Multifunctionalized iron oxide nanoparticles for selective targeting of pancreatic cancer cells,” *Biochim. Biophys. Acta BBA - Gen. Subj.*, Feb. 2017.
[130] V. V. Mody, A. Cox, S. Shah, A. Singh, W. Bevins, and H. Parihar, “Magnetic nanoparticle drug delivery systems for targeting tumor,” *Appl. Nanosci.*, vol. 4, no. 4, pp. 385–392, Apr. 2014.
[131] B. Mehdaoui, A. Meffre, J. Carrey, S. Lachaize, L.-M. Lacroix, M. Gougeon, B. Chaudret, and M. Respaud, “Optimal Size of Nanoparticles for Magnetic Hyperthermia: A Combined Theoretical and Experimental Study,” *Adv. Funct. Mater.*, vol. 21, no. 23, pp. 4573–4581, Dec. 2011.
[132] A. Jordan, P. Wust, H. Fähling, W. John, A. Hinz, and R. Felix, “Inductive heating of ferrimagnetic particles and magnetic fluids: Physical evaluation of their potential for hyperthermia,” *Int. J. Hyperthermia*, vol. 25, no. 7, pp. 499–511, Jan. 2009.
[133] R. E. Rosensweig, “Heating magnetic fluid with alternating magnetic field,” *Proc. 9th Int. Conf. Magn. Fluids*, vol. 252, pp. 370–374, Nov. 2002.
[134] B. Thiesen and A. Jordan, “Clinical applications of magnetic nanoparticles for hyperthermia,” *Int. J. Hyperthermia*, vol. 24, no. 6, pp. 467–474, Jan. 2008.
[135] Z. Wang, R. Qiao, N. Tang, Z. Lu, H. Wang, Z. Zhang, X. Xue, Z. Huang, S. Zhang, G. Zhang, and Y. Li, “Active targeting theranostic iron oxide nanoparticles for MRI and magnetic resonance-guided focused ultrasound ablation of lung cancer,” *Biomaterials*, vol. 127, pp. 25–35, May 2017.
[136] S. Maruyama, “Development of Magnetic Nanocarriers based on Thermosensitive Liposomes and their Visualization using Magnetic Particle Imaging,” *Int. J. Nanomedicine Nanosurgery ISSN 2470-3206*, vol. 2, no. 2, 2016.
[137] L. M. Bauer, S. F. Situ, M. A. Griswold, and A. C. S. Samia, “High-performance iron oxide nanoparticles for magnetic particle imaging – guided hyperthermia (hMPI),” *Nanoscale*, vol. 8, no. 24, pp. 12162–12169, 2016.
[138] D. Ho, X. Sun, and S. Sun, “Monodisperse Magnetic Nanoparticles for Theranostic Applications,” *Acc. Chem. Res.*, vol. 44, no. 10, pp. 875–882, Oct. 2011.
[139] J. Xie, G. Liu, H. S. Eden, H. Ai, and X. Chen, “Surface-Engineered Magnetic Nanoparticle Platforms for Cancer Imaging and Therapy,” *Acc. Chem. Res.*, vol. 44, no. 10, pp. 883–892, Oct. 2011.
[140] P. Howes, M. Green, A. Bowers, D. Parker, G. Varma, M. Kallumadil, M. Hughes, A. Warley, A. Brain, and R. Botnar, “Magnetic Conjugated Polymer Nanoparticles as Bimodal Imaging Agents,” *J. Am. Chem. Soc.*, vol. 132, no. 28, pp. 9833–9842, Jul. 2010.
[141] P. Majewski and B. Thierry, “Functionalized Magnetite Nanoparticles - Synthesis, Properties, and Bio-Applications,” *Crit. Rev. Solid State Mater. Sci.*, vol. 32, no. 3, pp. 203–215, Jul. 2007.
[142] T. G. Sparrow, B. G. Williams, C. N. R. Rao, and J. M. Thomas, “L3/L2 white-line intensity ratios in the electron energy-loss spectra of 3d transition-metal oxides,” *Chem. Phys. Lett.*, vol. 108, no. 6, pp. 547–550, Jul. 1984.
[143] H. Tan, J. Verbeeck, A. Abakumov, and G. Van Tendeloo, “Oxidation state and chemical shift investigation in transition metal oxides by EELS,” *Ultramicroscopy*, vol. 116, pp. 24–33, May 2012.
[144] C. J. Rossouw, L. J. Allen, S. D. Findlay, and M. P. Oxley, “Channelling effects in atomic resolution STEM,” *Ultramicroscopy*, vol. 96, no. 3–4, pp. 299–312, Sep. 2003.

[145] E. M. James and N. D. Browning, “Practical aspects of atomic resolution imaging and analysis in STEM,” *Ultramicroscopy*, vol. 78, no. 1, pp. 125–139, 1999.
[146] S. J. Pennycook, “Z-contrast STEM for materials science,” *Ultramicroscopy*, vol. 30, no. 1–2, pp. 58–69, 1989.
[147] K. M. Krishnan, “Iron L3,2 near-edge fine structure studies,” *Ultramicroscopy*, vol. 32, no. 4, pp. 309–311, May 1990.
[148] C. Colliex, T. Manoubi, and C. Ortiz, “Electron-energy-loss-spectroscopy near-edge fine structures in the iron-oxygen system,” *Phys. Rev. B*, vol. 44, no. 20, p. 11402, 1991.
[149] K. M. Krishnan, *Fundamentals and Applications of Magnetic Materials*. Oxford University Press, Oxford, United Kingdom, 2016.
[150] G. F. Goya, T. S. Berquó, F. C. Fonseca, and M. P. Morales, “Static and dynamic magnetic properties of spherical magnetite nanoparticles,” *J. Appl. Phys.*, vol. 94, no. 5, pp. 3520–3528, Sep. 2003.
[151] J. Landers, F. Stromberg, M. Darbandi, C. Schöppner, W. Keune, and H. Wende, “Correlation of superparamagnetic relaxation with magnetic dipole interaction in capped iron-oxide nanoparticles,” *J. Phys. Condens. Matter*, vol. 27, no. 2, p. 026002, Jan. 2015.
[152] E. J. Verwey, “Electronic Conduction of Magnetite (Fe3O4) and its Transition Point at Low Temperatures,” *Nature*, vol. 144, p. 327, Aug. 1939.
[153] S. Mørup and H. Topsøe, “Magnetic and electronic properties of microcrystals of Fe3O4,” *J. Magn. Magn. Mater.*, vol. 31, pp. 953–954, 1983.
[154] I. S. Lyubutin, C. R. Lin, Yu. V. Korzhetskiy, T. V. Dmitrieva, and R. K. Chiang, “Mössbauer spectroscopy and magnetic properties of hematite/magnetite nanocomposites,” *J. Appl. Phys.*, vol. 106, no. 3, p. 034311, Aug. 2009.
[155] D. H. Jones and K. K. P. Srivastava, “Many-state relaxation model for the Mössbauer spectra of superparamagnets,” *Phys. Rev. B*, vol. 34, no. 11, p. 7542, 1986.
[156] C. A. McCammon and D. C. Price, “Mössbauer spectra of FexO (x>0.95),” *Phys. Chem. Miner.*, vol. 11, no. 6, pp. 250–254, Jan. 1985.
[157] S. Ammar, N. Jouini, F. Fiévet, Z. Beji, L. Smiri, P. Moliné, M. Danot, and J.-M. Grenèche, “Magnetic properties of zinc ferrite nanoparticles synthesized by hydrolysis in a polyol medium,” *J. Phys. Condens. Matter*, vol. 18, no. 39, pp. 9055–9069, Oct. 2006.
[158] M. Darbandi, F. Stromberg, J. Landers, N. Reckers, B. Sanyal, W. Keune, and H. Wende, “Nanoscale size effect on surface spin canting in iron oxide nanoparticles synthesized by the microemulsion method,” *J. Phys. Appl. Phys.*, vol. 45, no. 19, p. 195001, May 2012.
[159] I. A. Aksay, M. Trau, S. Manne, I. Honma, N. Yao, L. Zhou, P. Fenter, P. M. Eisenberger, and S. M. Gruner, “Biomimetic Pathways for Assembling Inorganic Thin Films,” *Science*, vol. 273, no. 5277, pp. 892–898, 1996.
[160] K. Voïtchovsky, J. J. Kuna, S. A. Contera, E. Tosatti, and F. Stellacci, “Direct mapping of the solid–liquid adhesion energy with subnanometre resolution,” *Nat. Nanotechnol.*, vol. 5, no. 6, pp. 401–405, Jun. 2010.
[161] B. Hulsken, R. Van Hameren, J. W. Gerritsen, T. Khoury, P. Thordarson, M. J. Crossley, A. E. Rowan, R. J. M. Nolte, J. A. A. W. Elemans, and S. Speller, “Real-time single-molecule imaging of oxidation catalysis at a liquid–solid interface,” *Nat. Nanotechnol.*, vol. 2, no. 5, pp. 285–289, May 2007.
[162] B. R. Shrestha, T. Baimpos, S. Raman, and M. Valtiner, “Angstrom-Resolved Real-Time Dissection of Electrochemically Active Noble Metal Interfaces,” *ACS Nano*, vol. 8, no. 6, pp. 5979–5987, Jun. 2014.

[163] V. Prabhakaran, B. L. Mehdi, J. J. Ditto, M. H. Engelhard, B. Wang, K. D. D. Gunaratne, D. C. Johnson, N. D. Browning, G. E. Johnson, and J. Laskin, "Rational design of efficient electrode–electrolyte interfaces for solid-state energy storage using ion soft landing," *Nat. Commun.*, vol. 7, p. 11399, Apr. 2016.
[164] A. E. Nel, L. Mädler, D. Velegol, T. Xia, E. M. V. Hoek, P. Somasundaran, F. Klaessig, V. Castranova, and M. Thompson, "Understanding biophysicochemical interactions at the nano–bio interface," *Nat. Mater.*, vol. 8, no. 7, pp. 543–557, Jul. 2009.
[165] B. Pelaz, G. Charron, C. Pfeiffer, Y. Zhao, J. M. De La Fuente, X.-J. Liang, W. J. Parak, and P. Del Pino, "Interfacing engineered nanoparticles with biological systems: anticipating adverse nano–bio interactions," *Small*, vol. 9, no. 9–10, pp. 1573–1584, 2013.
[166] P. Rivera-Gil, D. Jimenez De Aberasturi, V. Wulf, B. Pelaz, P. Del Pino, Y. Zhao, J. M. De La Fuente, I. Ruiz De Larramendi, T. Rojo, X.-J. Liang, and W. J. Parak, "The Challenge To Relate the Physicochemical Properties of Colloidal Nanoparticles to Their Cytotoxicity," *Acc. Chem. Res.*, vol. 46, no. 3, pp. 743–749, Mar. 2013.
[167] J. Kolosnjaj-Tabi, Y. Javed, L. Lartigue, J. Volatron, D. Elgrabli, I. Marangon, G. Pugliese, B. Caron, A. Figuerola, N. Luciani, T. Pellegrino, D. Alloyeau, and F. Gazeau, "The One Year Fate of Iron Oxide Coated Gold Nanoparticles in Mice," *ACS Nano*, vol. 9, no. 8, pp. 7925–7939, Aug. 2015.
[168] N. Feliu, D. Docter, M. Heine, P. del Pino, S. Ashraf, J. Kolosnjaj-Tabi, P. Macchiarini, P. Nielsen, D. Alloyeau, F. Gazeau, R. H. Stauber, and W. J. Parak, "In vivo degeneration and the fate of inorganic nanoparticles," *Chem Soc Rev*, vol. 45, no. 9, pp. 2440–2457, 2016.
[169] I. O. Perez De Berti, M. V. Cagnoli, G. Pecchi, J. L. Alessandrini, S. J. Stewart, J. F. Bengoa, and S. G. Marchetti, "Alternative low-cost approach to the synthesis of magnetic iron oxide nanoparticles by thermal decomposition of organic precursors," *Nanotechnology*, vol. 24, no. 17, p. 175601, May 2013.
[170] A. S. Arbab, L. B. Wilson, P. Ashari, E. K. Jordan, B. K. Lewis, and J. A. Frank, "A model of lysosomal metabolism of dextran coated superparamagnetic iron oxide (SPIO) nanoparticles: implications for cellular magnetic resonance imaging," *NMR Biomed.*, vol. 18, no. 6, pp. 383–389, Oct. 2005.
[171] M. Levy, N. Luciani, D. Alloyeau, D. Elgrabli, V. Deveaux, C. Pechoux, S. Chat, G. Wang, N. Vats, F. Gendron, C. Factor, S. Lotersztajn, A. Luciani, C. Wilhelm, and F. Gazeau, "Long term in vivo biotransformation of iron oxide nanoparticles," *Biomaterials*, vol. 32, no. 16, pp. 3988–3999, Jun. 2011.
[172] L. Lartigue, D. Alloyeau, J. Kolosnjaj-Tabi, Y. Javed, P. Guardia, A. Riedinger, C. Péchoux, T. Pellegrino, C. Wilhelm, and F. Gazeau, "Biodegradation of Iron Oxide Nanocubes: High-Resolution *In Situ* Monitoring," *ACS Nano*, vol. 7, no. 5, pp. 3939–3952, May 2013.
[173] A. López-Cruz, C. Barrera, V. L. Calero-DdelC, and C. Rinaldi, "Water dispersible iron oxide nanoparticles coated with covalently linked chitosan," *J. Mater. Chem.*, vol. 19, no. 37, p. 6870, 2009.
[174] R. Zhu, W. Jiang, Y. Pu, K. Luo, Y. Wu, B. He, and Z. Gu, "Functionalization of magnetic nanoparticles with peptide dendrimers," *J. Mater. Chem.*, vol. 21, no. 14, p. 5464, 2011.
[175] S. J. H. Soenen, U. Himmelreich, N. Nuytten, and M. De Cuyper, "Cytotoxic effects of iron oxide nanoparticles and implications for safety in cell labelling," *Biomaterials*, vol. 32, no. 1, pp. 195–205, Jan. 2011.

[176] N. Singh, G. J. S. Jenkins, B. C. Nelson, B. J. Marquis, T. G. G. Maffeis, A. P. Brown, P. M. Williams, C. J. Wright, and S. H. Doak, "The role of iron redox state in the genotoxicity of ultrafine superparamagnetic iron oxide nanoparticles," *Biomaterials*, vol. 33, no. 1, pp. 163–170, Jan. 2012.
[177] S. P. Schwaminger, P. F. García, G. K. Merck, F. A. Bodensteiner, S. Heissler, S. Günther, and S. Berensmeier, "Nature of Interactions of Amino Acids with Bare Magnetite Nanoparticles," *J. Phys. Chem. C*, vol. 119, no. 40, pp. 23032–23041, Oct. 2015.
[178] B. Mattix, T. R. Olsen, T. Moore, M. Casco, D. Simionescu, R. P. Visconti, and F. Alexis, "Accelerated Iron Oxide Nanoparticle Degradation Mediated by Polyester Encapsulation within Cellular Spheroids," *Adv. Funct. Mater.*, vol. 24, no. 6, pp. 800–807, Feb. 2014.
[179] G. Gouy, "Sur la constitution de la charge electrique a la surface d'un electrolyte," *J Phys*, vol. 9, no. 4, pp. 457–468, 1910.
[180] D. L. Chapman, "LI. A contribution to the theory of electrocapillarity," *Lond. Edinb. Dublin Philos. Mag. J. Sci.*, vol. 25, no. 148, pp. 475–481, 1913.
[181] O. Stern, "Zur theorie der elektrolytischen doppelschicht," *Z. Für Elektrochem. Angew. Phys. Chem.*, vol. 30, no. 21–22, pp. 508–516, 1924.
[182] A. Elbourne, S. McDonald, K. Voïchovsky, F. Endres, G. G. Warr, and R. Atkin, "Nanostructure of the Ionic Liquid–Graphite Stern Layer," *ACS Nano*, vol. 9, no. 7, pp. 7608–7620, Jul. 2015.
[183] M. Pounds, S. Tazi, M. Salanne, and P. A. Madden, "Ion adsorption at a metallic electrode: an *ab initio* based simulation study," *J. Phys. Condens. Matter*, vol. 21, no. 42, p. 424109, Oct. 2009.
[184] J. M. Black, D. Walters, A. Labuda, G. Feng, P. C. Hillesheim, S. Dai, P. T. Cummings, S. V. Kalinin, R. Proksch, and N. Balke, "Bias-Dependent Molecular-Level Structure of Electrical Double Layer in Ionic Liquid on Graphite," *Nano Lett.*, vol. 13, no. 12, pp. 5954–5960, Dec. 2013.
[185] D. A. Welch, T. J. Woehl, C. Park, R. Faller, J. E. Evans, and N. D. Browning, "Understanding the Role of Solvation Forces on the Preferential Attachment of Nanoparticles in Liquid," *ACS Nano*, vol. 10, no. 1, pp. 181–187, Jan. 2016.
[186] P. Tian, "Molecular dynamics simulations of nanoparticles," *Annu. Rep. Sect. C Phys. Chem.*, vol. 104, p. 142, 2008.
[187] I. Siretanu, D. Ebeling, M. P. Andersson, S. L. S. Stipp, A. Philipse, M. C. Stuart, D. van den Ende, and F. Mugele, "Direct observation of ionic structure at solid-liquid interfaces: a deep look into the Stern Layer," *Sci. Rep.*, vol. 4, May 2014.
[188] T. LaGrange, G. H. Campbell, B. W. Reed, M. Taheri, J. B. Pesavento, J. S. Kim, and N. D. Browning, "Nanosecond time-resolved investigations using the in situ of dynamic transmission electron microscope (DTEM)," *Ultramicroscopy*, vol. 108, no. 11, pp. 1441–1449, Oct. 2008.
[189] E. A. Stach, "Real-time observations with electron microscopy," *Mater. Today*, vol. 11, pp. 50–58, 2008.
[190] M. J. Williamson, R. M. Tromp, P. M. Vereecken, R. Hull, and F. M. Ross, "Dynamic microscopy of nanoscale cluster growth at the solid–liquid interface," *Nat. Mater.*, vol. 2, no. 8, pp. 532–536, Aug. 2003.
[191] N. de Jonge and F. M. Ross, "Electron microscopy of specimens in liquid," *Nat. Nanotechnol.*, vol. 6, no. 11, pp. 695–704, Oct. 2011.

[192] P. Abellan, T. J. Woehl, L. R. Parent, N. D. Browning, J. E. Evans, and I. Arslan, "Factors influencing quantitative liquid (scanning) transmission electron microscopy," *Chem. Commun.*, vol. 50, no. 38, p. 4873, 2014.
[193] E. D. Boyes and P. L. Gai, "Environmental high resolution electron microscopy and applications to chemical science," *Ultramicroscopy*, vol. 67, no. 1–4, pp. 219–232, 1997.
[194] J. F. Creemer, S. Helveg, G. H. Hoveling, S. Ullmann, A. M. Molenbroek, P. M. Sarro, and H. W. Zandbergen, "Atomic-scale electron microscopy at ambient pressure," *Ultramicroscopy*, vol. 108, no. 9, pp. 993–998, Aug. 2008.
[195] C. Q. Chen, Y. T. Pei, and J. T. M. De Hosson, "Effects of size on the mechanical response of metallic glasses investigated through in situ TEM bending and compression experiments," *Acta Mater.*, vol. 58, no. 1, pp. 189–200, Jan. 2010.
[196] J. M. Yuk, J. Park, P. Ercius, K. Kim, D. J. Hellebusch, M. F. Crommie, J. Y. Lee, A. Zettl, and A. P. Alivisatos, "High-Resolution EM of Colloidal Nanocrystal Growth Using Graphene Liquid Cells," *Science*, vol. 336, no. 6077, pp. 61–64, Apr. 2012.
[197] H. Zheng, R. K. Smith, Y. Jun, C. Kisielowski, U. Dahmen, and A. P. Alivisatos, "Observation of Single Colloidal Platinum Nanocrystal Growth Trajectories," *Science*, vol. 324, no. 5932, pp. 1309–13012, Jun. 2009.
[198] N. de Jonge, N. Poirier-Demers, H. Demers, D. B. Peckys, and D. Drouin, "Nanometer-resolution electron microscopy through micrometers-thick water layers," *Ultramicroscopy*, vol. 110, no. 9, pp. 1114–1119, Aug. 2010.
[199] T. J. Woehl, J. E. Evans, I. Arslan, W. D. Ristenpart, and N. D. Browning, "Direct *in Situ* Determination of the Mechanisms Controlling Nanoparticle Nucleation and Growth," *ACS Nano*, vol. 6, no. 10, pp. 8599–8610, Oct. 2012.
[200] J. Hermannsdörfer, N. de Jonge, and A. Verch, "Electron beam induced chemistry of gold nanoparticles in saline solution," *Chem Commun*, vol. 51, no. 91, pp. 16393–16396, 2015.
[201] J. Y. Huang, L. Zhong, C. M. Wang, J. P. Sullivan, W. Xu, L. Q. Zhang, S. X. Mao, N. S. Hudak, X. H. Liu, A. Subramanian, H. Fan, L. Qi, A. Kushima, and J. Li, "In Situ Observation of the Electrochemical Lithiation of a Single SnO2 Nanowire Electrode," *Science*, vol. 330, no. 6010, pp. 1515–1520, Dec. 2010.
[202] B. L. Mehdi, J. Qian, E. Nasybulin, C. Park, D. A. Welch, R. Faller, H. Mehta, W. A. Henderson, W. Xu, C. M. Wang, J. E. Evans, J. Liu, J.-G. Zhang, K. T. Mueller, and N. D. Browning, "Observation and Quantification of Nanoscale Processes in Lithium Batteries by Operando Electrochemical (S)TEM," *Nano Lett.*, vol. 15, no. 3, pp. 2168–2173, Mar. 2015.
[203] M. Gu, Y. Li, X. Li, S. Hu, X. Zhang, W. Xu, S. Thevuthasan, D. R. Baer, J.-G. Zhang, J. Liu, and C. Wang, "*In Situ* TEM Study of Lithiation Behavior of Silicon Nanoparticles Attached to and Embedded in a Carbon Matrix," *ACS Nano*, vol. 6, no. 9, pp. 8439–8447, Sep. 2012.
[204] N. M. Schneider, M. M. Norton, B. J. Mendel, J. M. Grogan, F. M. Ross, and H. H. Bau, "Electron–Water Interactions and Implications for Liquid Cell Electron Microscopy," *J. Phys. Chem. C*, vol. 118, no. 38, pp. 22373–22382, Sep. 2014.
[205] C. Wang, Q. Qiao, T. Shokuhfar, and R. F. Klie, "High-Resolution Electron Microscopy and Spectroscopy of Ferritin in Biocompatible Graphene Liquid Cells and Graphene Sandwiches," *Adv. Mater.*, vol. 26, no. 21, pp. 3410–3414, Jun. 2014.

[206] K. Iakoubovskii, K. Mitsuishi, Y. Nakayama, and K. Furuya, "Thickness measurements with electron energy loss spectroscopy," *Microsc. Res. Tech.*, vol. 71, no. 8, pp. 626–631, Aug. 2008.
[207] D. Bouscaud, R. Pesci, S. Berveiller, and E. Patoor, "Estimation of the electron beam-induced specimen heating and the emitted X-rays spatial resolution by Kossel microdiffraction in a scanning electron microscope," *Ultramicroscopy*, vol. 115, pp. 115–119, Apr. 2012.
[208] J. J. De Yoreo, P. U. P. A. Gilbert, N. A. J. M. Sommerdijk, R. L. Penn, S. Whitelam, D. Joester, H. Zhang, J. D. Rimer, A. Navrotsky, J. F. Banfield, A. F. Wallace, F. M. Michel, F. C. Meldrum, H. Colfen, and P. M. Dove, "Crystallization by particle attachment in synthetic, biogenic, and geologic environments," *Science*, vol. 349, no. 6247, pp. aaa6760–aaa6760, Jul. 2015.
[209] F. M. Michel, L. Ehm, S. M. Antao, P. L. Lee, P. J. Chupas, G. Liu, D. R. Strongin, M. A. A. Schoonen, B. L. Phillips, and J. B. Parise, "The Structure of Ferrihydrite, a Nanocrystalline Material," *Science*, vol. 316, no. 5832, p. 1726, Jun. 2007.
[210] O. Sadeghi, L. N. Zakharov, and M. Nyman, "Aqueous formation and manipulation of the iron-oxo Keggin ion," *Science*, vol. 347, no. 6228, p. 1359, Mar. 2015.
[211] L. D. Marks, "Wiener-filter enhancement of noisy HREM images," *Ultramicroscopy*, vol. 62, no. 1, pp. 43–52, 1996.
[212] M. J. Berger, J. S. Coursey, M. A. Zucker, and J. Chang, "Stopping-Power & Range Tables for Electrons, Protons, and Helium Ions," *NIST Stand. Ref. Database*, vol. 124, Jul. 2017.
[213] T. Dudev and C. Lim, "Factors Governing the Protonation State of Cysteines in Proteins: An Ab Initio/CDM Study," *J. Am. Chem. Soc.*, vol. 124, no. 23, pp. 6759–6766, Jun. 2002.
[214] E. Bottari, M. R. Festa, and L. Gentile, "An Investigation on the Equilibria between Arginine and Iron(II) and Iron(III)," *J. Chem. Eng. Data*, vol. 58, no. 3, pp. 718–723, Mar. 2013.
[215] R. G. Neville, "The oxidation of cysteine by iron and hydrogen peroxide," *J. Am. Chem. Soc.*, vol. 79, no. 10, pp. 2456–2457, 1957.
[216] L. Michaelis and E. G. Barron, "Oxidation-Reduction Systems of Biological Significance IV. Comparative Study of the Complexes of Cysteine with the Metals of the Iron Group," *J. Biol. Chem.*, vol. 83, no. 1, pp. 191–210, 1929.
[217] A. Stevens, H. Yang, L. Carin, I. Arslan, and N. D. Browning, "The potential for Bayesian compressive sensing to significantly reduce electron dose in high-resolution STEM images," *Microscopy*, vol. 63, no. 1, pp. 41–51, Feb. 2014.
[218] T. J. Woehl and P. Abellan, "Defining the radiation chemistry during liquid cell electron microscopy to enable visualization of nanomaterial growth and degradation dynamics: DEFINING THE RADIATION CHEMISTRY DURING LCEM," *J. Microsc.*, vol. 265, no. 2, pp. 135–147, Feb. 2017.
[219] I. M. Lifshitz and V. V. Slyozov, "The kinetics of precipitation from supersaturated solid solutions," *J. Phys. Chem. Solids*, vol. 19, no. 1, pp. 35–50, 1961.
[220] B. v Derjaguin and L. Landau, "Theory of the stability of strongly charged lyophobic sols and of the adhesion of strongly charged particles in solutions of electrolytes," *Acad. Sci. USSR*, 1941.
[221] E. J. Verwey and J. Th. G. Overbeek, "Theory of the stability of lyophobic colloids," *Elsevier*, 1948.

APPENDIX A: REVIEW OF NUCLEATION, GROWTH, AND COLLOIDAL STABILITY THEORY

A.1 Supersaturation Driven Nucleation

The assembly of nanoparticles can proceed down a variety of pathways: a classic example being, supersaturation driven nucleation of a solid phase in a liquid matrix. In this description, growth proceeds by monomer addition of nutrient from liquid to solid phase at the interface. Synthesis of monodisperse colloids was described in by LaMer and Dinegar in 1950.[95] The LaMer supersaturation plot is reproduced in Figure 6.1.

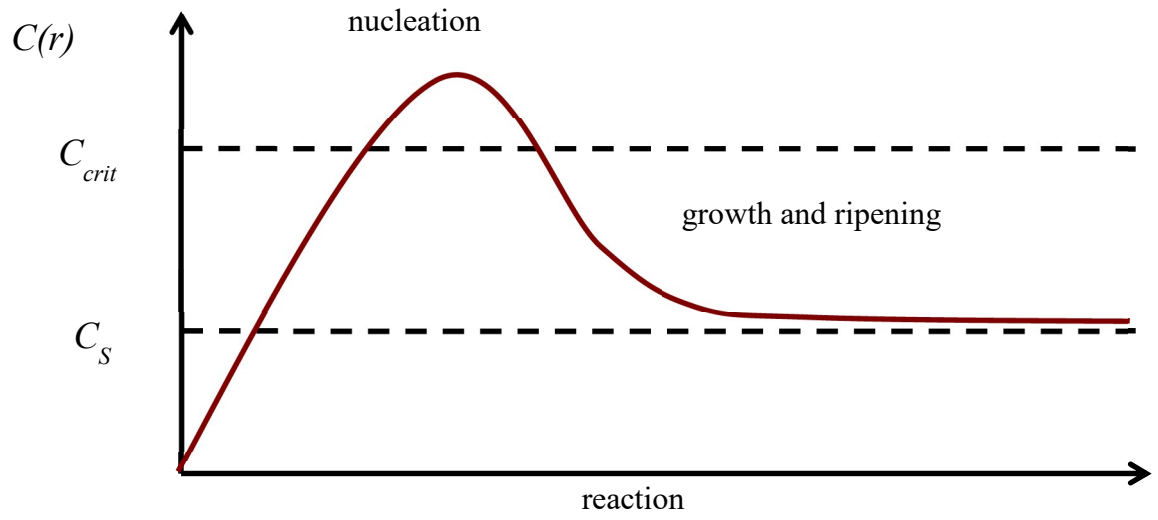

Figure 6.1. Schematic plot of monomer concentration versus time for the growth of nanoparticles, as described by LaMer. C_S indicates supersaturation, and C_{crit} indicates concentration for nucleation.

There are several synthetic methods used to reach supersaturation. A supply of nutrient can be added to solution at an elevated temperature or a chemical precursor can decompose to release nutrient into solution. The latter is typically achieved by heating the solution (thermolysis),

although other stimuli (electrolysis, pH, sonication) can be substituted. The most straightforward way to achieve uniform particles is to ensure that they all nucleate at the same time in a uniform environment and grow in similar conditions.

When the supersaturation exceeds some critical concentration, C_{crit}, there is enough driving force to nucleate new particles. If the solution remains supersaturated, existing particles can grow to alleviate said supersaturation. Between saturation, C_S, and C_{crit}, particles will grow but no new particles will nucleate. To produce monodisperse particles, nucleation must generally be separated from growth. If this is the case, all particles will start at the same size and at around the same time, and grow under similar conditions. To achieve this, an optimal synthesis will produce a rapid increase in precursor concentration above C_{crit}. To relieve this supersaturation, particles will nucleate, reducing the concentration to below critical. At this point particles will continue to grow as the concentration approaches C_S. In practice, the nucleation rate is finite and there will always be some size distribution. Depending on growth conditions, this distribution can either narrow or broaden with time.[97]

A.2 Critical Nucleus Size

The critical nucleus size, above which a precipitate is stable is often described as a trade-off between surface and volume free energy:

$$R_c = \frac{2\gamma}{\Delta G_v}$$

Where γ is the surface energy (per unit area), and ΔG_v is the free energy required to form a unit volume of solid phase. When the particle radius is greater than R_c, the particle will grow, when it is smaller than R_c, the particle will shrink. That is:

$$\frac{dR}{dt} > 0, \;\; R > R_c$$
$$\frac{dR}{dt} < 0, \;\; R < R_c$$

Furthermore, the nucleation rate can be described in terms of the activation energy to form a critical nucleus, ΔG^*, and the energy for an atom to cross the interface from solution to nucleus, ΔG_m.

$$\text{Nucleation rate} = K_v(T)\exp\left(-\frac{\Delta G^* + \Delta G_m}{k_B T}\right)$$

Where k_B is the Boltzmann constant, and $K_v(T)$ is a pre-exponent factor and function of temperature, T.

A.3 Growth Models

In some systems, growth may proceed by addition of monomers, as described by conventional growth models. Modeling this growth generally amounts to solving the concentration profile, $C(r)$. Mathematical models describe the nucleation rate, critical nucleus size, and growth rate of colloidal systems. Initial models focused on extreme cases of diffusion-limited and reaction-limited growth.[98] In diffusion limited growth, the supply of growth species to the particle surface is limited. In reaction limited growth, the rate-limiting step is the adsorption of growth species. More recently, the model has been generalized to account for intermediate cases.[97]

The most basic description of precipitate growth, often called the Lifshitz-Slyozov-Wagner (LSW) model,[219] simply applies conservation of mass to the diffusion equation:

$$J = 4\pi r^2 D \frac{dC}{dr}$$

Where J is the atomic flux, r is the radius (as a coordinate, not R of the particle), D is the diffusion constant, and C is the concentration of growth species in solution.

For isotropic growth in a spherical reference frame, the time evolution of the concentration profile $C(r)$ is described in terms of the diffusivity constant, D, by the equation:

$$\frac{\partial C}{\partial t} = D\left(\frac{\partial^2 C}{\partial r^2} + \frac{2}{r}\frac{\partial C}{\partial r}\right)$$

If we define a particle with diameter, R, the velocity of the particle surface is given by $v = \frac{dR}{dt}$

Under quasi-static conditions, that is if the velocity is less than the diffusion length: $v \ll D \cdot m$ then $\frac{\partial C}{\partial t} \approx 0$, and solutions to the diffusion equation takes the form:

$$C(r) = -\frac{A}{r} + C_b$$

Where C_b is the concentration of nutrient in bulk solution, and A is a constant

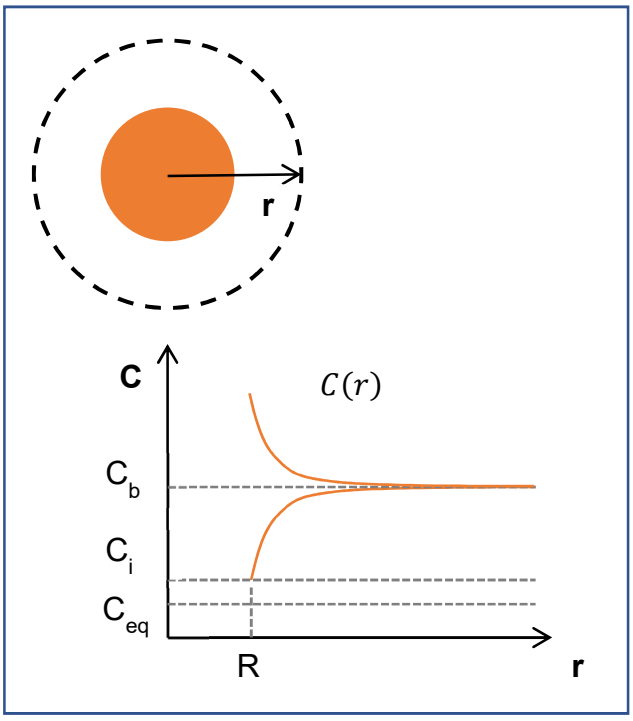

Figure 6.2. Solutions to the diffusion equation take the form $C(r) \sim 1/r$.

We can also relate the flux density of nutrient, *J*, to the mass accumulation at the growing (or dissolving) particle interface.

$$v(C_0 - C_i) = -J_I = D_I \frac{\partial C}{\partial r}\Big]_{r=R} = k\big(C_i - C_{eq}\big)$$

The velocity, here a function of the concentration difference at the interface, is simply equal to the flux density. Further, the precipitation/dissolution reaction at the interface is assumed to be first-order with respect to the difference between the interfacial concentration and equilibrium, given by the Gibbs Thompson equation:

$$C_{eq} = C_\infty \exp(\frac{2\gamma v}{RkT})$$

With some assumptions on boundary conditions, this defines the critical radius (R_C): for $r < R_C$ the precipitate will dissolve, and $r > R_C$ the precipitate will grow. When including a first-order precipitation reaction at the interface, with rate constant *k,* the kinetics can be regarded in two regimes: diffusion-controlled growth ($D << kr$), and reaction-controlled growth ($kr >> D$).[98] This has been recently generalized to consider the full range of *D* and *k* values.[97]

A.4 Colloidal Stability

The classical colloidal stability is often abbreviated DLVO Theory, for the scientists Derjaguin, Landau, Verwey, and Overbeek.[220], [221] In short, this model computes the energy to colloidal particles by considering as a combination of attractive, Van der Waals, and repulsive, electrostatic, forces, as depicted in Figure 6.3. This balance of attractive and repulsive forces defines an energy barrier. If this barrier is exceeded, attractive forces will dominate, and the colloids will aggregate.

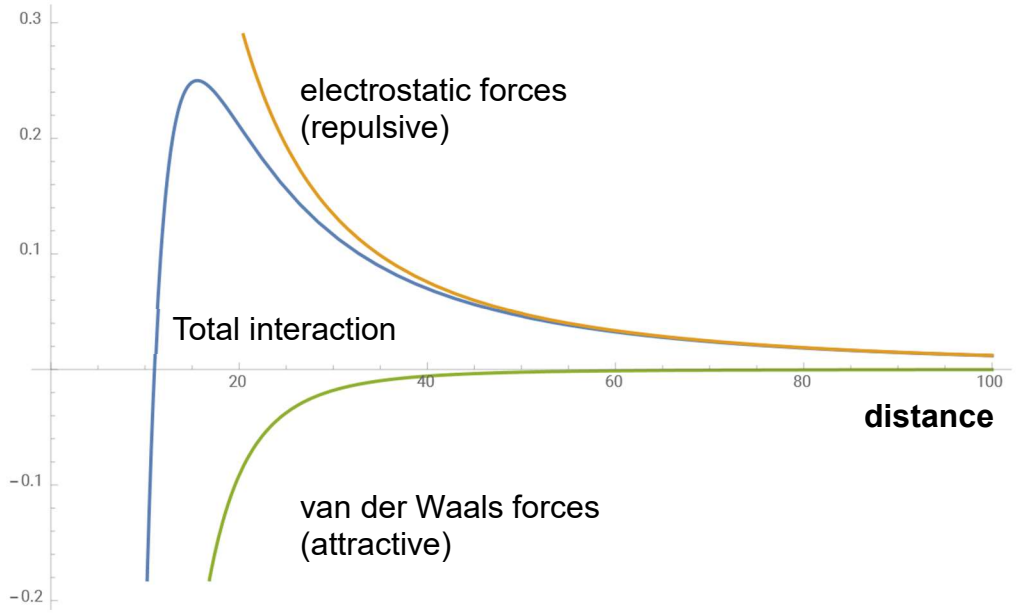

Figure 6.3. In DLVO theory, colloidal stability is considered as a combination of attractive and repulsive forces, with the total interaction energy acting as a barrier between dispersion and aggregation of colloids.